The multiconfiguration time-dependent Hartree (MCTDH) method: A highly efficient algorithm for propagating wavepackets

M. H. Beck, A. Jäckle, G. A. Worth, and H.-D. Meyer[1]

Theoretische Chemie, Physikalisch-Chemisches Institut, Universität Heidelberg,
Im Neuenheimer Feld 229, D-69120 Heidelberg, Germany

Abstract

A review is given on the multi-configuration time-dependent Hartree (MCTDH) method, which is an algorithm for propagating wavepackets. The formal derivation, numerical implementation, and performance of the method are detailed. As demonstrated by example applications, MCTDH may perform very efficiently, especially when there are many (typically four to twelve, say) degrees of freedom. The largest system treated with MCTDH to date is the pyrazine molecule, where all 24 (!) vibrational modes were accounted for.

The particular representation of the MCTDH wavefunction requires special techniques for generating an initial wavepacket and for analysing the propagated wavefunction. These techniques are discussed.

The full efficiency of the MCTDH method is only realised if the Hamiltonian can be written as a sum of products of one-dimensional operators. The kinetic energy operator and many model potential functions already have this required structure. For other potential functions, we describe an efficient algorithm for determining optimal fits of product form. An alternative to the product representation, the correlation discrete variable representation (CDVR) method, is also briefly discussed.

PACS: 31.15.Qg, 02.70.Ns

Keywords: MCTDH, multi-dimensional wavefunction propagation, quantum molecular dynamics

---

[1] to whom correspondence should be sent
(email: Hans-Dieter.Meyer@tc.pci.uni-heidelberg.de)

Contents

1 Introduction 6

2 Time-dependent methods 9

2.1 Time-dependent versus time-independent methods 9

2.2 The standard propagation method 10

2.3 Time-dependent Hartree 11

2.4 Multi-configurational approaches 14

3 MCTDH: Theory 15

3.1 The MCTDH equations of motion 15

3.2 Choice of constraints 18

3.3 Density matrices and natural orbitals 21

3.4 Interaction picture 23

3.5 Non-adiabatic systems 24

4 MCTDH: Implementation 26

4.1 Representation of the single-particle functions 26

4.2 Product representation of the Hamiltonian 26

4.3 Time-dependent and Correlation DVR 28

4.4 Numerical scaling in brief 29

4.5 Mode combination 31

4.6 Effort of the single- and multi-set formulation 32

4.7 Complex absorbing potentials 33

4.8 Projector and density matrix 34

5 MCTDH: Integration schemes 36

5.1 The variable mean-field (VMF) integration scheme 36

5.2 The constant mean-field (CMF) integration scheme 36

6 Product representation of potential energy surfaces 48

6.1 Expansion in natural potentials 48

6.2 Contraction over one mode 50

6.3 Iterative optimisation 51

6.4 Separable weights 53

6.5 Error measures 54

6.6 Emulating non-separable weights 56

6.7 Concluding remarks 58

6.8 Applications 58

7 Preparation of the initial wavepacket 62

7.1 Generation of eigenstates by energy relaxation 62

7.2 Initial wavepacket correction schemes for scattering problems 63

8 Analysis 70

8.1 Matrix elements of operators 70

8.2 Difference between MCTDH wavefunctions 70

8.3 Auto-correlation function and photo-absorption spectra 72

8.4 Filter-diagonalisation and ro-vibrational spectra 74

8.5 State populations 75

8.6 Excitation and reaction probabilities computed by flux analysis 75

8.7 Run-time analysis of the accuracy of the propagation 82

9 Selected applications 86

9.1 Photo-dissociation of NOCl 86

9.2 Reactive scattering of H+D_2 93

9.3 Surface scattering of N_2/LiF(001) 99

9.4 Photo-excitation of pyrazine 102

10 Conclusions and outlook 109

Acknowledgements 111

A Variational principles for the time-dependent Schrödinger equation 112

B Discrete variable representation (DVR) 115

B.1 VBR and FBR representation of the potential 115

B.2 Diagonalisation DVR 117

B.3 Quadrature DVR 119

B.4 Examples 120

C The Lanczos and the Lanczos-Arnoldi integrator 129

D $\mathcal{L}^2$-error of the product representation 132

E Overview of software packages 135

E.1 The MCTDH program 135

E.2 The POTFIT program 136

E.3 The ANALYSE programs 136

E.4 The FILTER program 137

E.5 The MCTDH library 137

E.6 System requirements 137

References 139

List of Figures

1 Diagrammatic description of the CMF scheme 39

2 The CMF error in dependence of the error tolerance 41

3 H+$D_2(\nu = 0, 1)$ reaction cross-sections 98

List of Tables

1 Errors of three product representations of collinear H+H_2 60

2 Calculations to date using the MCTDH method 87

3 Computational resources for the photo-dissociation of NOCl 90

4 Computational resources for the 4-mode pyrazine model 105

5 Computational resources for the 9-mode pyrazine model 107

E.1 Platforms on which the MCTDH software has been installed 138

1 Introduction

During the last two decades the interest in quantum molecular dynamics has continuously risen [1–3]. Many new experiments, in particular those in the field of femto-chemistry [4,5], require accompanying calculations for interpretation. A quantum mechanical study can be done in the time-independent picture by diagonalisation of the Hamiltonian, or in the time-dependent picture by propagation of a wavepacket. The standard method of solving the Schrödinger equation in either picture uses a representation of the wavepacket and Hamiltonian in an appropriate product basis. The method is thereby restricted by the computational resources required, which grow exponentially with the number of degrees of freedom.

As a result, for most of the above period numerically exact quantum mechanical methods were in general restricted to tri-atomic systems. Due to the increase in computer power and — equally important — the development of new efficient algorithms [6–10], the treatment of tetra-atomic systems is now becoming the state of the art, but studies of systems with more than six degrees of freedom are in general still impossible. This limit has been pushed to larger dimensions by introducing special — and often problem specific — techniques, such as pre-diagonalisation of low-dimensional Hamiltonians (see [11–13] and references in the latter citation), or configuration selection by Rayleigh-Schrödinger perturbation theory [14], or by wave operator methods [15].

The exponential scaling can be avoided by turning to more approximate, in particular to semiclassical, methods. There have been new developments in this field recently, showing impressive results [16]. We will discuss semiclassical methods no further and refer the reader to recent reviews [17,18].

In the time-dependent picture, on which we focus in the following, further approximations have been developed which keep a fully quantum mechanical picture while removing the scaling problem in a more general manner. These methods are exemplified by the TDH method (also known as time-dependent self-consistent field (TDSCF)) [19,20]. Here, the wavefunction is represented as a Hartree product of one-dimensional functions, resulting in a set of coupled one-dimensional equations of motion for the wavepacket (see Sec. 2.3). The effort required is thus significantly reduced, but at the cost that the correlation between degrees of freedom is no longer correctly treated. Various schemes have been developed to correct for this loss of correlation, e.g. by modifying the Hartree wavefunction by a time-dependent unitary operator [21–23], or by a multi-configurational (MC-TDSCF) approach, i.e. approximating the wavefunction by a number of Hartree products [24–26].

A particularly efficient variant of the MC-TDSCF approach is the multiconfiguration time-dependent Hartree (MCTDH) method [27–30]. The MCTDH method, to which this review is devoted, combines the efficiency of a mean-field method, such as TDH, with the accuracy of a numerically exact solution. Using a multi-configurational wavefunction ansatz, and solving the time-dependent Schrödinger equation by a variational method, leads to a set of coupled equations of motion for the expansion coefficients and for the set of functions used to build the Hartree product configurations. The latter are known as single-particle functions. As all possible configurations from the set of single-particle functions are build, the method is unfortunately also plagued by exponential scaling. However, the base to be exponentiated is substantially smaller compared with the standard methods. This enables the treatment of larger systems by the MCTDH scheme.

In the limit of convergence with respect to the number of configurations, the results of an MCTDH propagation are numerically exact. Even in this limit the equations of motion, while seemingly complex, require less effort than the standard method for large systems. An important feature of the method is that, due to its variational character, a small set of single-particle functions can be used to produce qualitatively good results with a minimum of effort. Internal checks using the population of the single-particle functions can then be used as a guide to the quality of the results.

The method has been applied successfully to a number of phenomena, such as photodissociation [28,31–34] and photoabsorption spectra [35–38], predissociation [39], and reactive [40–46] and molecule-surface scattering [47–53]. To demonstrate the applicability of the method to large systems, it should be mentioned that converged calculations on a system with two coupled electronic states and 24 nuclear degrees of freedom have been performed [36–38].

The purpose of this review is to provide an overview of the MCTDH theory and the application of the method, with an emphasis on the description of the algorithm (see Secs. 3 and 4). In App. E, a brief description of our MCTDH computer package is given.

A wavepacket propagation calculation can be divided into three parts:

(1) Generation of the initial wavepacket.
(2) Propagation of the wavepacket.
(3) Analysis of the propagated wavepacket.

These stages are described in detail.

The core of the MCTDH method is the wavepacket propagation. Here, one important factor for the solution of the equations of motion is the choice of the primitive basis used to represent the single-particle functions. In general a discrete variable representation (DVR) is used, and here various standard DVRs are described (see Appendix B): harmonic oscillator, Legendre, spherical harmonics, sine, and exponential, as well as the related fast Fourier transform

(FFT) basis. Various integration schemes are then possible. In particular, a very efficient integrator has been developed [54] which exploits the fact that the mean-field matrices, which correlate the motion of the single-particle functions, change slower in time than the single-particle functions themselves. This integrator is described in Sec. 5.

The MCTDH propagation will in general be efficient only if the Hamiltonian is given in product form. The kinetic energy operator is usually in this form, as are many model potential operators, and profit has been made of this feature when investigating surface scattering [47–52] and vibronic coupling [35–37]. When the potential does not have a product structure, one may either use the recently developed correlation DVR [55] (see Sec. 4.3), or fit the potential to the desired form [56,57]. An algorithm accomplishing such a fit is discussed in Sec. 6.

The initial form of the wavepacket must be chosen to fit the product form of the MCTDH wavefunction. A simple wavepacket may be chosen, and then modified before propagation (see Sec. 7). For example, in many applications the initial state is an eigenstate of a potential energy surface. These can be generated by the method of energy relaxation (propagation in imaginary time). For scattering problems, a Wentzel-Kramers-Brillouin (WKB) correction scheme has been developed that allows the initial wavepacket to be placed close to the interaction region.

After the propagation has been completed, it is necessary to extract the quantities of interest. In this analysis step, which is addressed in Sec. 8, one again has to take into account the particular form of the MCTDH wavefunction. Examples are given for various evaluations: how to obtain a spectrum from the Fourier transform of the autocorrelation function or by employing the filter-diagonalisation method, calculate the flux into a reaction channel, or monitor the probability density along a coordinate.

Finally, in Sec. 9 examples of calculations are given to highlight the various points of the algorithm, and to show how the possible choices affect the computational effort and accuracy of the calculation.

2 Time-dependent methods

In the earlier days of quantum molecular dynamics time-dependent methods were largely ignored. Solving the time-independent Schrödinger equation was considered as being significantly more efficient. This view began to change when Heller's first paper on Gaussian wavepacket propagation [58] appeared in 1975. In the following years new numerical techniques were developed for solving the time-dependent Schrödinger equation numerically exactly [7]. In particular, powerful integrators were invented [9], such as the split-operator [59–61], the Chebyshev [62], and the short iterative Lanczos [63] scheme. Since then the time-dependent approach has become popular.

2.1 Time-dependent versus time-independent methods

The quantal motion of the nuclei of a molecule or collision complex is most naturally described by solving the time-dependent Schrödinger equation. If the Hamiltonian H is time-independent, however, the propagated wavepacket may conveniently be expanded in the set of eigenstates of H (we use a unit system throughout where $\hbar = 1$),

$$\psi(t) = \sum_j a_j \, e^{-iE_j t} \varphi_j \,, \tag{1}$$

where

$$H \, \varphi_j = E_j \, \varphi_j \qquad \text{and} \qquad a_j = \langle \varphi_j \, | \, \psi(0) \rangle \,. \tag{2}$$

This well-known expansion shows that the knowledge of a wavepacket $\psi(t)$ for all times and the knowledge of all eigenstates φ_j and energies E_j are equivalent. The decision to follow the time-dependent or the time-independent approach is thus a matter of taste, and a question of numerical efficiency.

Although being formally equivalent, the time-independent approach seems to be easier because one variable — the time — has disappeared from the equations to be solved. However, in the time-independent picture one has to solve an eigenvalue problem, whereas using the time-dependent approach one is faced with an initial value problem, which is mathematically simpler. This point is of particular importance when treating scattering or half-collision (e.g. photo-dissociation) processes. In these cases the eigenstates become continuum functions with complicated scattering boundary conditions. The sum in Eq. (1) has to be replaced by an integral over the continuum states. In the time-dependent framework, on the other hand, the wavepacket remains square integrable, and there is essentially no difference in propagating a wavepacket that is a superposition of bound or continuum states.

The time-dependent picture becomes even more attractive when turning to approximate methods. One may distinguish two classes of approximations. Methods from the first class simplify the Hamiltonian. The coupled states approximation [64,65] (also known as j_z-conserving approximation) is a typical example out of this category. Approximations of this type can be employed in both the time-independent and time-dependent framework. In both pictures they introduce the same errors and lead to a similar reduction of the numerical effort.

The other class is based on approximating the wavefunction. Here a typical example is the Hartree approximation, which writes the multi-dimensional wavefunction as a simple product of one-dimensional functions. This approach works in general much better in the time-dependent picture, because a time-dependent wavepacket is usually more or less localised (in phase space), while an eigenstate is typically rather delocalised. Hence the time-dependent approach enables the use of approximations which are more efficient and more accurate than their time-independent counterparts.

Besides these technical advantages, a time-dependent description often leads to a better understanding of the physical process under discussion. Finally, if the Hamiltonian is itself time-dependent, one must of course adopt the time-dependent picture.

2.2 The standard propagation method

The standard approach for solving the time-dependent Schrödinger equation is the numerically exact propagation of a wavepacket represented in a time-independent product basis set, i.e. the wavefunction is written as

$$\Psi(Q_1,\ldots,Q_f,t) = \sum_{j_1=1}^{N_1} \cdots \sum_{j_f=1}^{N_f} C_{j_1\ldots j_f}(t) \prod_{\kappa=1}^{f} \chi_{j_\kappa}^{(\kappa)}(Q_\kappa)\,, \tag{3}$$

where f specifies the number of degrees of freedom, $Q_1,\ldots,Q_f$ are the nuclear coordinates, the $C_{j_1\ldots j_f}$ denote the time-dependent expansion coefficients, and the $\chi_{j_\kappa}^{(\kappa)}$ are the time-independent basis functions for degree of freedom κ. To allow an efficient and accurate evaluation of the action of the Hamiltonian H on the wavefunction Ψ, one usually chooses the N_κ basis functions $\chi_{j_\kappa}^{(\kappa)}$ to be the DVR/FBR functions of a collocation method, typified by those discussed in App. B.

The equations of motion for $C_{j_1 \dots j_f}(t)$ can be derived from the Dirac-Frenkel variational principle [19,66]

$$\langle \delta\Psi \,|\, H - i\partial_t \,|\, \Psi \rangle = 0 \,, \tag{4}$$

where ∂_t denotes the partial derivative with respect to time, leading to

$$i\dot{C}_J = \sum_L H_{JL} C_L \,, \tag{5}$$

where we have established the multi-index $J = j_1 \dots j_f$ (and analogously for L). $H_{JL} = \langle \chi^{(1)}_{j_1} \dots \chi^{(f)}_{j_f} \mid H \mid \chi^{(1)}_{l_1} \dots \chi^{(f)}_{l_f} \rangle$ is the matrix representation of the Hamiltonian given in the product basis set $\{\chi^{(\kappa)}_{j_\kappa}\}$. Equation (5) forms a system of coupled linear first-order ordinary differential equations, which can be solved by integrators explicitly designed for equations of that kind [9], such as the split-operator [59–61], Chebyshev [62] or Lanczos [63] methods.

The computational effort of this numerically exact treatment grows exponentially with the number of degrees of freedom f. To see this we define the effort as the number of floating point operations to be carried out, and assume for simplicity that the same number $N = N_1 = \dots = N_f$ of basis functions is employed for each degree of freedom. If one utilises the fact that the kinetic energy part of H can be written in tensor form and that the potential energy is diagonal on a DVR grid, the computational effort necessary to evaluate the right hand side of Eq. (5) is then proportional to fN^{f+1}. Here we have neglected the effort for computing the matrix representation of H since this has to be done only once at the beginning of the propagation. This scaling behaviour generally restricts the standard method to systems with not more than five or six degrees of freedom.

2.3 Time-dependent Hartree

In order to circumvent the disadvantageous scaling behaviour of a numerically exact propagation, approximate methods for solving the time-dependent Schrödinger equation have been developed. The most widely used approximate scheme is the time-dependent Hartree (TDH) method [19,20] (also known as the time-dependent self-consistent field (TDSCF) method), which we will briefly discuss in the following. Understanding this approach will pave the way to understanding the MCTDH method. To keep the discussion as simple as possible we restrict ourselves to the treatment of two degrees of freedom only. The extension to larger systems is straightforward.

In the TDH approximation the wavefunction is written as

$$\Psi(x,y,t) = a(t)\,\varphi_1(x,t)\,\varphi_2(y,t)\ , \tag{6}$$

where a is a time-dependent complex number and φ_1 and φ_2 are known as *single-particle functions* or *orbitals*. The product $\varphi_1\varphi_2$ is called a *Hartree product*.

Equation (6) does not determine the single-particle functions uniquely, since phase and normalisation factors may be shifted from φ_1 to φ_2 or even to a. The introduction of the (redundant) term $a(t)$ allows us to freely choose the phases of both φ_1 and φ_2. We write the constraints that fix the phases in differential form:

$$\langle\varphi_1\,|\,\dot\varphi_1\rangle = \langle\varphi_2\,|\,\dot\varphi_2\rangle = 0\,. \tag{7}$$

These constraints also guarantee that the norm of φ_1 and φ_2 does not change. Hence φ_1 and φ_2 will stay normalised throughout the propagation,

$$\|\,\varphi_1(t)\,\| = \|\,\varphi_2(t)\,\| = 1\,, \tag{8}$$

if they are normalised initially.

The equations of motion for $a(t)$, $\varphi_1(t)$, and $\varphi_2(t)$ are derived from the Dirac-Frenkel variational principle (4). Variation with respect to a yields

$$\langle\varphi_1\varphi_2\,|\,i\dot a\varphi_1\varphi_2 + ia\dot\varphi_1\varphi_2 + ia\varphi_1\dot\varphi_2 - Ha\varphi_1\varphi_2\rangle = 0 \tag{9}$$

or, with the aid of the constraints (7) and (8),

$$i\dot a = \langle H\rangle a\,, \tag{10}$$

where $\langle H\rangle = \langle\varphi_1\varphi_2\,|\,H\ |\ \varphi_1\varphi_2\rangle$. Similarly, by varying φ_1 and φ_2 we obtain

$$i\dot\varphi_1 = \Big(H^{(1)} - \langle H\rangle\Big)\,\varphi_1 \quad\text{and}\quad i\dot\varphi_2 = \Big(H^{(2)} - \langle H\rangle\Big)\,\varphi_2\,, \tag{11}$$

with the *mean-field operators*

$$H^{(1)} = \langle\varphi_2\,|\,H\ |\ \varphi_2\rangle \quad\text{and}\quad H^{(2)} = \langle\varphi_1\,|\,H\,|\,\varphi_1\rangle\,. \tag{12}$$

Equation (11) can be alternatively written as

$$i\dot\varphi_1 = \Big(1-\,|\,\varphi_1\rangle\langle\varphi_1\,|\,\Big)H^{(1)}\varphi_1 \quad\text{and}\quad i\dot\varphi_2 = \Big(1-\,|\,\varphi_2\rangle\langle\varphi_2\,|\,\Big)H^{(2)}\varphi_2\,, \tag{13}$$

where $\mid \varphi_1\rangle\langle\varphi_1 \mid$ and $\mid \varphi_2\rangle\langle\varphi_2 \mid$ denote the projectors onto the state φ_1 or φ_2, respectively. It is now obvious that the equations of motion satisfy the constraints (7) and (8).

The TDH wavefunction can be considered as being propagated by an effective Hamiltonian H_{eff},

$$i\dot{\Psi} = H_{\mathrm{eff}}\,\Psi\,, \tag{14}$$

with

$$H_{\mathrm{eff}} = H^{(1)} + H^{(2)} - \langle H \rangle\,. \tag{15}$$

To investigate the errors introduced by the TDH approximation let us assume that the Hamiltonian has the form

$$H = -\frac{1}{2m_1}\frac{\partial^2}{\partial x^2} - \frac{1}{2m_2}\frac{\partial^2}{\partial y^2} + V_1(x) + V_2(y) + W_1(x)\,W_2(y)\,. \tag{16}$$

In this case one finds that

$$H_{\mathrm{eff}} = H - \Big(W_1 - \langle W_1 \rangle\Big)\Big(W_2 - \langle W_2 \rangle\Big)\,, \tag{17}$$

or

$$i\dot{\Psi} - H\Psi = -\Big(W_1 - \langle W_1 \rangle\Big)\Big(W_2 - \langle W_2 \rangle\Big)\Psi\,. \tag{18}$$

The right hand side of the above equation describes the error introduced by the Hartree approximation. The error vanishes if the Hamiltonian is separable, and it becomes small if the functions W_1 and W_2 are almost constant over the width of the single-particle functions φ_1 and φ_2, respectively. This is why the time-dependent Hartree method is usually more accurate than the time-independent Hartree method; the time-dependent wavepacket is likely to be localised, whereas the eigenstates are usually very delocalised.

The TDH approximation has been intensively used by Gerber and coworkers [67–70] who have applied it to systems with very many (≈ 100) modes. The treatment of such large systems became possible through the development of the classical based separable potential (CSP) method [67], which is a very efficient way to approximately evaluate the mean-fields. Although the use of the CSP method destroys the variational basis of the TDH approach, it seems to introduce only small errors.

As the performance of the TDH method is often rather poor, an obvious suggestion is to improve the method by taking several configurations into account. The first investigations on multi-configurational time-dependent SCF (MC-TDSCF) — as the method was called — were made by Makri and Miller [24] and by Kosloff *et al.* [25], both in 1987. These important early investigations were formulated for two degrees of freedom and two configurations only. As the two-dimensional case is a special case, generalisation of these approaches is not obvious. The latter approach has been developed further [26], but not pursued later.

In this review we will discuss the multiconfiguration time-dependent Hartree (MCTDH) method. This algorithm, which was published in 1990 [27], is fully general from its outset. The number of degrees of freedom and the number of single-particle functions per degree of freedom is arbitrary. The latter feature allows MCTDH to cover the full range of quality of approximation, from TDH to numerically exact. The particular choice of constraints used in the derivation of MCTDH (see Eq. (22) below) makes the working equations — albeit seemingly complex — simpler than those of their predecessors.

It should be noted that the acronym MC-TDSCF is used for the whole family of multi-configurational approaches, while MCTDH, being uniquely defined in Sec. 3.1, is a special variant of the MC-TDSCF family.

Because of the complexity of MCTDH, simplified methods have been tried. One may for instance perform a TDH calculation, diagonalise the mean-fields to obtain a full set of single-particle functions, and generate a correlated wavepacket via a time-dependent CI in a space of single-particle functions. This approach — called TDH-CI [71–75], or TDSCF with CI corrections [76,77] — may be regarded as an approximation to MCTDH. The single-particle functions are obtained here in a simplified way. However, it is not important to simplify the equations of motion of the single-particle functions, because their solution requires only a small fraction of the total effort when larger systems are considered. But it is of crucial importance to have optimal single-particle functions in order to keep the number of configurations as small as possible. Being fully based on an variational principle, as is detailed in the following section, the MCTDH working equations generate optimal single-particle functions.

3 MCTDH: Theory

In this section the working equations of the MCTDH scheme [27–30] are derived. The MCTDH scheme is motivated by the discussion of the preceding sections 2.2 and 2.3, since MCTDH combines the benefits of the standard, numerically exact, wavefunction propagation and the time-dependent Hartree approaches. We also describe several modifications of the original MCTDH algorithm that serve to further improve the efficiency and extend the applicability of the method.

3.1 The MCTDH equations of motion

In the MCTDH scheme the TDH approach is generalised by writing the wavefunction Ψ, which describes the molecular dynamics of a system with f degrees of freedom, as a linear combination of Hartree products, i.e. the *ansatz* for the wavefunction becomes

$$\Psi(Q_1,\dots,Q_f,t) = \sum_{j_1=1}^{n_1} \dots \sum_{j_f=1}^{n_f} A_{j_1\dots j_f}(t) \prod_{\kappa=1}^{f} \varphi_{j_\kappa}^{(\kappa)}(Q_\kappa,t)\,, \tag{19}$$

where $Q_1,\dots,Q_f$ are the nuclear coordinates, the $A_{j_1\dots j_f}$ denote the MCTDH expansion coefficients, and the $\varphi_{j_\kappa}^{(\kappa)}$ are the n_κ expansion functions for each degree of freedom κ, known as *single-particle functions*. Setting $n_1 = \dots = n_f = 1$ one arrives at the TDH wavefunction. TDH is thus contained in MCTDH as a limiting case. As the numbers n_κ are increased, the more accurate the propagation of the wavefunction becomes, and the MCTDH wavefunction monotonically converges towards the numerically exact one, Eq. (3), as n_κ approaches N_κ. The computational labour, however, increases strongly with increasing values of n_κ. We will later provide some guidelines as to how to choose the numerical values of the n_κ consistently, in order to achieve some desired level of accuracy (see Sec. 8.7). Here we note that the n_κ should obey [27]

$$n_\kappa^2 \leq \prod_{\kappa'=1}^{f} n_{\kappa'}\,, \tag{20}$$

otherwise there will be redundant configurations. For two dimensions the condition $n_1 = n_2$ follows, but for higher dimensions Eq. (20) usually does not pose a constraint.

As in the case of the TDH approximation, the MCTDH wavefunction representation (19) is not unique, one may linearly transform the single-particle functions and the expansion coefficients while still representing the same wavefunction. These redundancies prohibit singularity-free well-defined equations of motion. Uniquely defined propagation is obtained by imposing the constraints

$$\langle\varphi_j^{(\kappa)}(0)\,|\,\varphi_l^{(\kappa)}(0)\rangle = \delta_{jl} \tag{21}$$

and

$$\langle\varphi_j^{(\kappa)}(t)\,|\,\dot{\varphi}_l^{(\kappa)}(t)\rangle = -i\,\langle\varphi_j^{(\kappa)}(t)\,|\,g^{(\kappa)}\,|\,\varphi_l^{(\kappa)}(t)\rangle \tag{22}$$

on the single-particle functions. Here the *constraint operator* $g^{(\kappa)}$ is a Hermitian, but otherwise arbitrary, operator acting exclusively on the κth degree of freedom. The constraints (21) and (22) imply that the initially orthonormal single-particle functions remain orthonormal for all times.

Before presenting the MCTDH working equations we simplify the notation by establishing the composite index J and the configurations Φ_J:

$$A_J = A_{j_1\ldots j_f} \qquad \text{and} \qquad \Phi_J = \prod_{\kappa=1}^{f} \varphi_{j_\kappa}^{(\kappa)}\,. \tag{23}$$

We also introduce the projector on the space spanned by the single-particle functions for the κth degree of freedom:

$$P^{(\kappa)} = \sum_{j=1}^{n_\kappa} |\,\varphi_j^{(\kappa)}\rangle\langle\varphi_j^{(\kappa)}\,|\ . \tag{24}$$

The *single-hole functions* $\Psi_l^{(\kappa)}$ are defined as the linear combination of Hartree products of $(f-1)$ single-particle functions that do not contain the single-particle functions for the coordinate Q_κ,

$$\begin{aligned}\Psi_l^{(\kappa)} &= \sum_{j_1}\cdots\sum_{j_{\kappa-1}}\sum_{j_{\kappa+1}}\cdots\sum_{j_f} A_{j_1\ldots j_{\kappa-1} l j_{\kappa+1}\ldots j_f}\,\varphi_{j_1}^{(1)}\cdots\varphi_{j_{\kappa-1}}^{(\kappa-1)}\varphi_{j_{\kappa+1}}^{(\kappa+1)}\cdots\varphi_{j_f}^{(f)}\\ &= \sum_J^{\kappa} A_{J_l^\kappa}\,\varphi_{j_1}^{(1)}\cdots\varphi_{j_{\kappa-1}}^{(\kappa-1)}\varphi_{j_{\kappa+1}}^{(\kappa+1)}\cdots\varphi_{j_f}^{(f)}\,,\end{aligned} \tag{25}$$

where in the last line J_l^κ denotes a composite index J with the κth entry set at l, and $\sum_J^\kappa$ is the sum over the indices for all degrees of freedom excluding the κth.

The single-hole functions enable us to define the *mean-fields*

$$\langle H\rangle_{jl}^{(\kappa)} = \langle\Psi_j^{(\kappa)}\,|\,H\,|\,\Psi_l^{(\kappa)}\rangle \tag{26}$$

and *density matrices*

$$\begin{aligned}\rho_{jl}^{(\kappa)} &= \langle \Psi_j^{(\kappa)} \,|\, \Psi_l^{(\kappa)} \rangle \\ &= \sum_{j_1} \cdots \sum_{j_{\kappa-1}} \sum_{j_{\kappa+1}} \cdots \sum_{j_f} A^*_{j_1 \ldots j_{\kappa-1} j j_{\kappa+1} \ldots j_f} A_{j_1 \ldots j_{\kappa-1} l j_{\kappa+1} \ldots j_f} \\ &= \sum_J^{\kappa} A^*_{J_j^\kappa} A_{J_l^\kappa} \,.\end{aligned} \tag{27}$$

In Sec. 3.3 a discussion on the density matrix is given. Note that $\langle H \rangle_{jl}^{(\kappa)}$ is an operator acting on the κth degree of freedom, and that the trace of $\boldsymbol{\rho}^{(\kappa)}$ equals $\parallel \Psi \parallel^2$ due to the orthonormality of the single-particle functions.

Using the notation introduced above, we may express Ψ, $\dot{\Psi}$, and the variation $\delta\Psi$ as

$$\Psi = \sum_J A_J \Phi_J = \sum_{j=1}^{n_\kappa} \varphi_j^{(\kappa)} \Psi_j^{(\kappa)} \,, \tag{28}$$

$$\dot{\Psi} = \sum_{\kappa=1}^{f} \sum_{j=1}^{n_\kappa} \dot{\varphi}_j^{(\kappa)} \Psi_j^{(\kappa)} + \sum_J \dot{A}_J \Phi_J \,, \tag{29}$$

$$\frac{\delta\Psi}{\delta A_J} = \Phi_J \qquad \text{and} \qquad \frac{\delta\Psi}{\delta\varphi_j^{(\kappa)}} = \Psi_j^{(\kappa)} \,. \tag{30}$$

With the aid of the variational principle (4) (see also App. A) and the constraints (21) and (22) one finds when varying the coefficients:

$$\langle \Phi_J \,|\, H \,|\, \Psi \rangle - i \langle \Phi_J \,|\, \dot{\Psi} \rangle = 0 \tag{31}$$

and hence

$$i\dot{A}_J = \langle \Phi_J \,|\, H \,|\, \Psi \rangle - \sum_{\kappa=1}^{f} \sum_{l=1}^{n_\kappa} g_{j_\kappa l}^{(\kappa)} A_{J_l^\kappa} \,, \tag{32}$$

where $g_{jl}^{(\kappa)} = \langle \varphi_j^{(\kappa)} \,|\, g^{(\kappa)} \,|\, \varphi_l^{(\kappa)} \rangle$.

Varying with respect to the single-particle functions yields

$$\langle \Psi_j^{(\kappa)} \,|\, H \,|\, \Psi \rangle = i \langle \Psi_j^{(\kappa)} \,|\, \sum_{\kappa'=1}^{f} \sum_{l=1}^{n_{\kappa'}} \dot{\varphi}_l^{(\kappa')} \Psi_l^{(\kappa')} \rangle + i \sum_J \langle \Psi_j^{(\kappa)} \,|\, \Phi_J \rangle \dot{A}_J \,. \tag{33}$$

From this one obtains

$$i\sum_{l=1}^{n_\kappa}\rho_{jl}^{(\kappa)}\dot{\varphi}_l^{(\kappa)} = \langle\Psi_j^{(\kappa)}\,|\,H\,|\,\Psi\rangle - \sum_J \langle\Psi_j^{(\kappa)}\,|\,\Phi_J\rangle\,\langle\Phi_J\,|\,H\,|\,\Psi\rangle + \sum_{k,l=1}^{n_\kappa}\rho_{jk}^{(\kappa)}g_{lk}^{(\kappa)}\varphi_l^{(\kappa)}\,. \tag{34}$$

Noticing that

$$\sum_J \langle\Psi_j^{(\kappa)}\,|\,\Phi_J\rangle\,\langle\Phi_J\,| = P^{(\kappa)}\langle\Psi_j^{(\kappa)}\,| \tag{35}$$

and

$$\langle\Psi_j^{(\kappa)}\,|\,H\,|\,\Psi\rangle = \sum_{l=1}^{n_\kappa}\langle H\rangle_{jl}^{(\kappa)}\varphi_l^{(\kappa)}\,, \tag{36}$$

and after some rearrangement, one finally arrives at the MCTDH working equations

$$i\dot{A}_J = \sum_L \langle\Phi_J\,|\,H\,|\,\Phi_L\rangle A_L - \sum_{\kappa=1}^{f}\sum_{l=1}^{n_\kappa} g_{j_\kappa l}^{(\kappa)} A_{J_l^\kappa}\,, \tag{37}$$

$$i\dot{\boldsymbol{\varphi}}^{(\kappa)} = g^{(\kappa)}\mathbf{1}_{n_\kappa}\boldsymbol{\varphi}^{(\kappa)} + \left(1 - P^{(\kappa)}\right)\left[\left(\boldsymbol{\rho}^{(\kappa)}\right)^{-1}\langle\boldsymbol{H}\rangle^{(\kappa)} - g^{(\kappa)}\mathbf{1}_{n_\kappa}\right]\boldsymbol{\varphi}^{(\kappa)}\,, \tag{38}$$

where a vector notation has been adopted for the single-particle functions with

$$\boldsymbol{\varphi}^{(\kappa)} = \left(\varphi_1^{(\kappa)},\ldots,\varphi_{n_\kappa}^{(\kappa)}\right)^T\,, \tag{39}$$

$\boldsymbol{\rho}^{(\kappa)}$ the density matrix, $\langle\boldsymbol{H}\rangle^{(\kappa)}$ the matrix of mean field operators, and $\mathbf{1}_{n_\kappa}$ the $n_\kappa \times n_\kappa$ unit matrix. The choice of the constraint operator, $g^{(\kappa)}$, can then be used to change the final form of the equations of motion, either to simplify them, or to highlight different aspects of the dynamics. This problem will be addressed in detail in Sec. 3.2.

We close this section by emphasising that the MCTDH equations conserve the norm and, for time-independent Hamiltonians, the total energy. This follows directly from the variational principle (cf. App. A).

3.2 Choice of constraints

In the previous section 3.1, the MCTDH equations of motion were derived without explicitly defining the constraint single-particle operator, $g^{(\kappa)}$. The choice of this operator is arbitrary, and it does not affect the quality of the

MCTDH wavefunction. It does however affect the numerical performance of the integration of the equations of motion, as it is possible to transfer the work from the integration of the equations of motion for the coefficients to those for the single-particle functions. Here we describe some of the possible choices for this constraint operator.

The simplest choice is to set $g^{(\kappa)} = 0$ for all degrees of freedom. When this is done, the MCTDH equations of motion read

$$i\dot{A}_J = \sum_L \langle \Phi_J \,|\, H \,|\, \Phi_L \rangle A_L \,, \tag{40}$$

$$i\dot{\boldsymbol{\varphi}}^{(\kappa)} = \left(1 - P^{(\kappa)}\right) \left(\boldsymbol{\rho}^{(\kappa)}\right)^{-1} \langle \boldsymbol{H} \rangle^{(\kappa)} \boldsymbol{\varphi}^{(\kappa)} \,. \tag{41}$$

The relationship to the standard method equations of motion, Eq. (5), is here clear. When $n_\kappa = N_\kappa$ the single-particle function basis is complete, and so the right-hand side of Eq. (41) is zero, resulting in a time-independent basis.

A second possibility is to use the fact that the Hamiltonian may contain certain terms that operate only on one degree of freedom. Denoting these separable terms by $h^{(\kappa)}$ the Hamiltonian can then be written

$$H = \sum_{\kappa=1}^{f} h^{(\kappa)} + H_{\mathrm{R}} \,, \tag{42}$$

where the residual part, H_{R}, includes all the correlations between the degrees of freedom. If the constraints $g^{(\kappa)} = h^{(\kappa)}$ are now taken, the MCTDH equations of motion change to

$$i\dot{A}_J = \sum_L \langle \Phi_J \,|\, H_{\mathrm{R}} \,|\, \Phi_L \rangle A_L \,, \tag{43}$$

$$i\dot{\boldsymbol{\varphi}}^{(\kappa)} = \left[h^{(\kappa)} \mathbf{1}_{n_\kappa} + \left(1 - P^{(\kappa)}\right) \left(\boldsymbol{\rho}^{(\kappa)}\right)^{-1} \langle \boldsymbol{H}_{\mathrm{R}} \rangle^{(\kappa)} \right] \boldsymbol{\varphi}^{(\kappa)} \,, \tag{44}$$

where the matrix elements $\langle \Phi_J \mid H_{\mathrm{R}} \mid \Phi_L \rangle$ and mean-fields $\langle H_{\mathrm{R}} \rangle_{jl}^{(\kappa)}$ are now evaluated using only the residual part of the Hamiltonian.

Compared to Eq. (43), the working equation (40) has the disadvantage that the full Hamiltonian H instead of the residual Hamiltonian H_{R} is employed in the propagation of the MCTDH coefficients, which is computationally more expensive. While it seems that Eq. (44) also gains over the working equation (41) by using only the residual Hamiltonian to build the mean fields, in practice this is not the case, as Eq. (41) can be rewritten to also take advantage of the separable parts of the Hamiltonian:

$$i\dot{\boldsymbol{\varphi}}^{(\kappa)} = \left(1 - P^{(\kappa)}\right) \left[h^{(\kappa)} \mathbf{1}_{n_\kappa} + \left(\boldsymbol{\rho}^{(\kappa)}\right)^{-1} \langle \boldsymbol{H}_{\mathrm{R}} \rangle^{(\kappa)} \right] \boldsymbol{\varphi}^{(\kappa)} \,. \tag{45}$$

In many cases the different amount of work required to propagate the MCTDH coefficients can make a noticeable difference to the required computer time. For example, in the case of the 4-mode model for the photo-excitation of the pyrazine molecule [35], a calculation employing Eqs. (40) and (45) is 8% slower compared with one using Eqs. (43) and (44).

The use of Eq. (41) or (45) however implies that the motion of the single-particle functions is minimised, because the projector exclusively allows motions in directions perpendicular to the space spanned by the single-particle functions. Reducing the motion of the single-particle functions to a minimum may be favourable for some integrators. This is for example the case when using the constant-mean-field integrator described below in Sec. 5.2, which has been developed to optimally integrate the MCTDH equations of motion.

It is important to note that these two sets of equations are connected by a similarity transformation:

$$\tilde{\varphi}_j^{(\kappa)} = \sum_l \varphi_l^{(\kappa)} U_{lj}^{(\kappa)} \,, \tag{46}$$

$$\tilde{A}_{j_1 \dots j_f} = \sum_{l_1} \dots \sum_{l_f} \left(\boldsymbol{U}^{(1)^\dagger} \right)_{j_1 l_1} \dots \left(\boldsymbol{U}^{(f)^\dagger} \right)_{j_f l_f} A_{l_1 \dots l_f} \,, \tag{47}$$

where, if $\tilde{A}$ and $\tilde{\varphi}$ are the coefficients and single-particle functions from Eqs. (40) and (41), and A and φ are those from Eqs. (43) and (44), then $\boldsymbol{U}^{(\kappa)} = \exp(i\boldsymbol{h}^{(\kappa)}t)$, with $h_{jl}^{(\kappa)} = \langle \varphi_j^{(\kappa)} \,|\, h^{(\kappa)} \,|\, \varphi_l^{(\kappa)} \rangle$. Similar transformations connect the basis functions propagated using any two constraint operators, replacing $\boldsymbol{h}^{(\kappa)}$ in the unitary transformation operator with the difference between the constraint operators. This underlines the fact the constraints make no difference to the accuracy of the representation of the wavefunction.

One last possibility for the choice of constraints will be mentioned here. A Hermitian operator can be chosen that is completely described within the single-particle basis, i.e.

$$g^{(\kappa)} = \sum_{l,j=1}^{n_\kappa} |\, \varphi_l^{(\kappa)} \rangle \, g_{lj}^{(\kappa)} \langle \varphi_j^{(\kappa)} \,| \ . \tag{48}$$

The constraint operator to the right of the projector in Eq. (38) then disappears, and the equations of motion read

$$i\dot{A}_J = \sum_L \langle \Phi_J \,|\, H \,|\, \Phi_L \rangle A_L - \sum_{\kappa=1}^{f} \sum_{l=1}^{n_\kappa} g_{j_\kappa l}^{(\kappa)} A_{J_l^\kappa} \,, \tag{49}$$

$$i\dot{\boldsymbol{\varphi}}^{(\kappa)} = \left(\boldsymbol{g}^{(\kappa)} \right)^T \boldsymbol{\varphi}^{(\kappa)} + \left(1 - P^{(\kappa)} \right) \left(\boldsymbol{\rho}^{(\kappa)} \right)^{-1} \langle \boldsymbol{H} \rangle^{(\kappa)} \boldsymbol{\varphi}^{(\kappa)} \,, \tag{50}$$

where $\boldsymbol{g}^{(\kappa)}$ is the constraint operator matrix with elements $g_{lj}^{(\kappa)}$ (see Eq. (48)). (Eq. (50) holds generally, as it may be derived directly from Eq. (34)). It is of course also possible to add the separable Hamiltonian terms to these constraints, replacing H by H_R, and replacing $\boldsymbol{g}^{(\kappa)^T}$ by $h^{(\kappa)}\mathbf{1}_{n_\kappa} + \boldsymbol{g}^{(\kappa)^T}$.

Constraint operators of this type are time-dependent, and the matrix representation must be recalculated at each step. They may be used to enforce the single-particle functions to retain a particular property. An example is given below in Sec. 3.3, where constraints of this form are developed so that the single-particle functions are the natural orbitals of the system, i.e. the density matrices remain diagonal.

3.3 Density matrices and natural orbitals

So far we have said nothing about the physical meaning of the density matrix $\boldsymbol{\rho}^{(\kappa)}$ defined in Eq. (27). For an interpretation of $\boldsymbol{\rho}^{(\kappa)}$ we turn to the related density operator. Using the definitions (25) and (27) we express the density operator as

$$\begin{aligned}\hat{\rho}^{(\kappa)}(Q_\kappa, Q'_\kappa) &= \sum_{j,l=1}^{n_\kappa} \varphi_j^{(\kappa)}(Q_\kappa)\, \rho_{lj}^{(\kappa)}\, \varphi_l^{(\kappa)^*}(Q'_\kappa) \\ &= \int \Psi^*(Q_1, \ldots, Q'_\kappa, \ldots, Q_f)\, \Psi(Q_1, \ldots, Q_\kappa, \ldots, Q_f) \\ &\quad \times dQ_1 \ldots dQ_{\kappa-1}\, dQ_{\kappa+1} \ldots dQ_f\,. \end{aligned} \tag{51}$$

This shows that $\boldsymbol{\rho}^{(\kappa)}$ is similar to the well-known one-particle density of electronic structure theory [78], and related to a reduced density matrix [79]. (Note that our density matrix is the transposed of the matrix representation of the density operator in the set of the single-particle functions.) Diagonalising the operator $\hat{\rho}^{(\kappa)}$ yields the *natural populations* and *natural orbitals* [27,28,47,80], defined as the eigenvalues and eigenvectors of $\hat{\rho}^{(\kappa)}$. Since we are dealing with distinguishable particles we have a separate density matrix for each degree of freedom.

In contrast to the single-particle functions, the natural orbitals are uniquely defined. The former depend on the choice of the single-particle constraint operators $g^{(\kappa)}$ (see Sec. 3.2), as well as on the chosen set of initial single-particle functions. Replacing the single-particle functions of *ansatz* (19) by the natural orbitals we arrive at a unique MCTDH representation of the wavefunction. Furthermore, the natural populations characterise the contribution of the related natural orbitals to the representation of the wavefunction. Small natural populations indicate that the MCTDH expansion converges, and this provides an important internal check on the quality of the computed solution. (See for instance Refs. [28,31,34,39,40,47,50–52] for examples.) For very small or even vanishing eigenvalues, the Hermitian and positive semi-definite density matrix will become singular. This numerical problem is addressed in Sec. 4.8.

As mentioned above in Sec. 3.2, it is possible to define a set of constraint operators, $g^{(\kappa)}$, using Eq. (48) such that the single-particle functions retain the "natural" form, i.e. the density matrices remain diagonal during the propagation [80]. Using Eqs. (25), (27), (28), and (37) one may write the time-derivative of the density matrix as

$$\begin{aligned} i\dot{\rho}^{(\kappa)}_{jl} = {} & \langle \Psi^{(\kappa)}_j \varphi^{(\kappa)}_l \,|\, H \,|\, \Psi \rangle - \langle \Psi \,|\, H \,|\, \Psi^{(\kappa)}_l \varphi^{(\kappa)}_j \rangle \\ & - \sum_{k=1}^{n_\kappa} \left(\rho^{(\kappa)}_{jk} g^{(\kappa)}_{lk} - \rho^{(\kappa)}_{kl} g^{(\kappa)}_{kj} \right) \\ & + \sum_{\kappa' \neq \kappa}^{f} \left(\langle \Psi \,|\, g^{(\kappa')} \,|\, \Psi^{(\kappa)}_l \varphi^{(\kappa)}_j \rangle - \langle \Psi^{(\kappa)}_j \varphi^{(\kappa)}_l \,|\, g^{(\kappa')} \,|\, \Psi \rangle \right) , \end{aligned} \tag{52}$$

where $g^{(\kappa)}_{lk}$ is as before the matrix representation of the constraint operator in the single-particle function basis. Since

$$\langle \Psi \,|\, g^{(\kappa')} \,|\, \Psi^{(\kappa)}_l \varphi^{(\kappa)}_j \rangle = \langle \Psi^{(\kappa)}_j \varphi^{(\kappa)}_l \,|\, g^{(\kappa')} \,|\, \Psi \rangle \, , \tag{53}$$

the last sum in Eq. (52) vanishes.

We now require that

$$\rho^{(\kappa)}_{jl} = \delta_{jl}\, \rho^{(\kappa)}_{ll} \tag{54}$$

and thus in particular that

$$\dot{\rho}^{(\kappa)}_{jl} = 0 \quad \text{for} \quad j \neq l \, . \tag{55}$$

According to Eq. (52) this condition holds if one chooses

$$g^{(\kappa)}_{jl} = \frac{\langle \Psi \,|\, H \,|\, \Psi^{(\kappa)}_j \varphi^{(\kappa)}_l \rangle - \langle \Psi^{(\kappa)}_l \varphi^{(\kappa)}_j \,|\, H \,|\, \Psi \rangle}{\rho^{(\kappa)}_{jj} - \rho^{(\kappa)}_{ll}} \, , \quad j \neq l \, . \tag{56}$$

The diagonal elements $g^{(\kappa)}_{jj}$ are not determined by the requirement (55) and may be chosen arbitrarily. Usually they are set to zero. Note that if the populations of different natural orbital are similar Eq. (56) becomes singular. This introduces the need to regularise the operator matrix (see Sec. 4.8).

Using these constraint operator matrices, Eqs. (49) and (50) become the *natural orbital equations of motion* [80]. Note that the single-particle operators are now time-dependent, and must be recalculated at every time step of the propagation. If the Hamiltonian is in the form of products of one-dimensional operators (see Sec. 4.2), as is required for the efficient use of the MCTDH algorithm, the work to build these operator matrices is minimal: the matrix is formed from products of the mean-field matrices with the one-dimensional operator matrices, both of which are required anyway.

We emphasise again that all three sets of equations of motion derived above using different constraint operators, Eqs. (40,41), (43,44), and (49,50), generate the same propagated wavefunction $\Psi(t)$. Its representation, and the numerical performance of the algorithm however differ. The attraction of using natural orbitals comes from the idea that a wavefunction represented in this basis set optimally converges with respect to the number of configurations required. In the MCTDH theory however, this quicker convergence is not achieved, as the propagated natural orbitals and other single-particle functions span the same space. We have performed some test calculations with natural orbital propagation and found no advantage (see e.g. Sec. 9.4). However, propagation in natural orbitals has been reported in Refs. [47,50,51,53].

3.4 Interaction picture

In some cases a significant increase in efficiency can be found by moving from the normal, Schrödinger, picture to an interaction picture for the propagation of the single-particle functions. For this, the single-particle function $\varphi_j^{(\kappa)}(t)$ is back-transformed in time to $\zeta_j^{(\kappa)}(t)$ by the unitary transformation

$$\zeta_j^{(\kappa)}(t) = \exp\left(ih^{(\kappa)}t\right)\varphi_j^{(\kappa)}(t)\,, \tag{57}$$

where $h^{(\kappa)}$ is the single-particle operator introduced in Eq. (42). The exponentiation of these operators is accomplished by diagonalising their DVR matrix representation. When these new orbitals are substituted into Eq. (44), a new set of equations of motion for the interaction picture orbitals,

$$i\dot{\boldsymbol{\zeta}}^{(\kappa)} = \exp\left(ih^{(\kappa)}t\right)\left(1-P^{(\kappa)}\right)\left(\boldsymbol{\rho}^{(\kappa)}\right)^{-1}\langle\boldsymbol{H}_{\mathrm{R}}\rangle^{(\kappa)}\exp\left(-ih^{(\kappa)}t\right)\boldsymbol{\zeta}^{(\kappa)}\,, \tag{58}$$

is obtained.

At each time t, a transformation is therefore required between the interaction picture and the Schrödinger picture orbitals. The propagation of the interaction picture orbitals however only includes the residual Hamiltonian H_{R}. When the residual terms are small, the equations of motion are smoother in the interaction than in the Schrödinger picture, so that larger integration steps are possible. For example, in a calculation of the absorption spectrum of pyrazine, the step size in the interaction picture was typically two to three times larger than in the Schrödinger picture [35]. A less dramatic increase was observed in a study on the collinear reactive scattering $H+H_2 \rightarrow H_2+H$. When this system was represented in Jacobian coordinates, the use of the interaction picture led to an increase of step size by 30%. In binding coordinates, however, the step size was only 6% larger than in the Schrödinger picture, and the reduction of the numerical effort incident to it was completely compensated by the effort for the transformation between the two pictures [81].

The increase of step size due to the use of the interaction picture implies that the single-particle functions have limited the integration steps in all these examples. This indicates that the single-particle functions often change more rapidly than the MCTDH expansion coefficients.

3.5 Non-adiabatic systems

The motion of the molecular nuclei is often determined by a single Born-Oppenheimer potential energy surface. This situation was implicitly assumed in the discussion so far. However, applications like photo-absorption or photo-dissociation involve electronically excited states, and there one must frequently account for the non-adiabatic coupling to another, or even several other, electronic states.

The MCTDH algorithm can also be applied to systems where more than one electronic state is included. One possibility to accomplish this is to choose one extra degree of freedom, the κ_eth say, to represent the electronic manifold [32,33]. The coordinate Q_{κ_e} then labels the electronic states, taking only discrete values $Q_{\kappa_e} = 1, 2, \ldots, \sigma$, where σ is the number of electronic states under consideration. The number of single-particle functions for such an electronic mode is set to the number of states, i.e. $n_{\kappa_e} = \sigma$. The equations of motion (37) and (38) remain unchanged, treating nuclear and electronic modes on the same footing. This is called the *single-set formulation*, since only one set of single-particle functions is used for all the electronic states.

Contrary to this, the *multi-set formulation* employs different sets of single-particle functions for each electronic state [48,35]. In this formulation the wavefunction Ψ and the Hamiltonian H are expanded in the set $\{| \, \alpha\rangle\}$ of electronic states:

$$|\,\Psi\rangle = \sum_{\alpha=1}^{\sigma} \Psi^{(\alpha)} \, |\,\alpha\rangle \tag{59}$$

and

$$H = \sum_{\alpha,\beta=1}^{\sigma} |\,\alpha\rangle H^{(\alpha\beta)} \langle\beta\,| \, , \tag{60}$$

where each state function $\Psi^{(\alpha)}$ is expanded in MCTDH form (19). The derivation of the equations of motion corresponds to the single-set formalism detailed in Sec. 3.1, except that extra state labels have to be introduced on the various quantities such as constraint operators, mean fields and density matrices. Selecting the constraint operators $g^{(\alpha,\kappa)} = 0$ for simplicity, the equations of motion read

$$i\dot{A}_J^{(\alpha)} = \sum_{\beta=1}^{\sigma} \sum_L \langle \Phi_J^{(\alpha)} \,|\, H^{(\alpha\beta)} \,|\, \Phi_L^{(\beta)} \rangle A_L^{(\beta)} \,, \tag{61}$$

$$i\dot{\boldsymbol{\varphi}}^{(\alpha,\kappa)} = \left(1 - P^{(\alpha,\kappa)}\right) \left(\boldsymbol{\rho}^{(\alpha,\kappa)}\right)^{-1} \sum_{\beta=1}^{\sigma} \langle \boldsymbol{H} \rangle^{(\alpha\beta,\kappa)} \boldsymbol{\varphi}^{(\beta,\kappa)} \,, \tag{62}$$

with mean-fields

$$\langle H \rangle_{jl}^{(\alpha\beta,\kappa)} = \langle \Psi_j^{(\alpha,\kappa)} \,|\, H^{(\alpha\beta)} \,|\, \Psi_l^{(\beta,\kappa)} \rangle \,. \tag{63}$$

The superscripts α and β denote to which electronic state the functions and operators belong. Other constraints such as $g^{(\alpha,\kappa)} = h^{(\alpha,\kappa)}$, where $h^{(\alpha,\kappa)}$ is the separable part of the Hamiltonian for the αth electronic state, can be chosen analogously to the single-set formalism, discussed in Sec. 3.2.

A fuller derivation of these equations is given in Ref. [35]. In Sec. 4.6 the computational effort of the single- and multi-set approach is compared (see also Ref. [54]).

4 MCTDH: Implementation

While in the preceding Sec. 3 we concentrated on the theory underlying the MCTDH approach, this part now focuses on the concrete implementation of the MCTDH algorithm. The computational effort of the MCTDH scheme is also discussed and compared with the standard method.

4.1 Representation of the single-particle functions

In order to implement the MCTDH working equations, the single-particle functions have to be represented by a finite set of numbers. Expanding the single-particle functions in a set of primitive (i.e. time-independent) basis functions is a straightforward way to generate such a representation. For treating polar angles (θ, ϕ) such an approach has in fact been used [52]. In that work two-dimensional single-particle functions were expanded in a set of spherical harmonics $Y_{lm}(\theta, \phi)$.

In other cases the single-particle functions are represented pointwise by employing a collocation scheme of the fast Fourier transform (FFT) [7,82] or the discrete variable representation (DVR) [83–86] type. The basic idea of a DVR is to use a primitive basis which is based on a set of orthogonal polynomials. By diagonalising the position operator, $\hat{Q}$, in this basis, a set of DVR basis functions, $\{|\chi_\alpha\rangle\}$, and grid points, $\{Q_\alpha\}$, are obtained, where the αth function is an approximation to a delta function on the αth point. Operators local in coordinate space, e.g. the potential energy operator, are now taken as diagonal on the DVR points. Non-local operators, such as kinetic energy operators, are expressed as a matrix, evaluating the matrix elements analytically in the polynomial basis before transforming to the DVR basis. Examples for DVR representations are harmonic oscillator (or Hermite), Legendre, sine and exponential DVR. For more details on FFT and DVR representations we refer the reader to App. B.

4.2 Product representation of the Hamiltonian

For the MCTDH algorithm to be efficient, one has to avoid the direct evaluation of the Hamiltonian matrix elements $\langle \Phi_J \mid H \mid \Phi_L \rangle$ and mean-fields $\langle H_{\mathrm{R}} \rangle_{jl}^{(\kappa)} = \langle \Psi_j^{(\kappa)} \mid H_{\mathrm{R}} \mid \Psi_l^{(\kappa)} \rangle$ occurring in the equations of motion, since this would require f-fold and $(f-1)$-fold integrations, respectively. These multi-dimensional integrations can be circumvented if the residual Hamiltonian H_{R} is written as a sum of products of single-particle operators,

$$H_{\mathrm{R}} = \sum_{r=1}^{s} c_r \prod_{\kappa=1}^{f} h_r^{(\kappa)} , \tag{64}$$

with expansion coefficients c_r.

The kinetic energy operator normally has the required form (64). Often, however, the potential energy operator does not have the necessary structure, and it must be fitted to the product form. A convenient, systematic, and efficient approach to obtain an optimal product representation is described in Sec. 6.

Using Eq. (64) the matrix elements can be expanded as

$$\langle \Phi_J \,|\, H \,|\, \Phi_L \rangle = \sum_{\kappa=1}^{f} \langle \varphi^{(\kappa)}_{j_\kappa} \,|\, h^{(\kappa)} \,|\, \varphi^{(\kappa)}_{l_\kappa} \rangle + \sum_{r=1}^{s} c_r \prod_{\kappa=1}^{f} \langle \varphi^{(\kappa)}_{j_\kappa} \,|\, h^{(\kappa)}_r \,|\, \varphi^{(\kappa)}_{l_\kappa} \rangle \,. \tag{65}$$

Again the $h^{(\kappa)}$ and $h^{(\kappa)}_r$ denote the single-particle operators building up the separable and the residual part of the Hamiltonian, respectively. The mean-field operators now read

$$\langle H_{\mathrm{R}} \rangle^{(\kappa)}_{jl} = \sum_{r=1}^{s} \mathcal{H}^{(\kappa)}_{rjl} h^{(\kappa)}_r \,, \tag{66}$$

where the *mean-field matrix* $\boldsymbol{\mathcal{H}}^{(\kappa)}_r$ has elements

$$\mathcal{H}^{(\kappa)}_{rjl} = c_r {\sum_J}^{\kappa} A^*_{J^\kappa_j} \sum_{l_1} \langle \varphi^{(1)}_{j_1} \,|\, h^{(1)}_r \,|\, \varphi^{(1)}_{l_1} \rangle \ldots \sum_{l_f} \langle \varphi^{(f)}_{j_f} \,|\, h^{(f)}_r \,|\, \varphi^{(f)}_{l_f} \rangle A_{L^\kappa_l} \,. \tag{67}$$

Note that "…" does not contain a sum over l_κ.

The time-derivative of the MCTDH coefficients, Eq. (37), can now be written as

$$\begin{aligned} i\dot{A}_J =& \sum_{\kappa=1}^{f} \sum_{l=1}^{n_\kappa} \langle \varphi^{(\kappa)}_{j_\kappa} \,|\, h^{(\kappa)} - g^{(\kappa)} \,|\, \varphi^{(\kappa)}_{l} \rangle A_{J^\kappa_l} \\ &+ \sum_{r=1}^{s} c_r \sum_{l_1} \langle \varphi^{(1)}_{j_1} \,|\, h^{(1)}_r \,|\, \varphi^{(1)}_{l_1} \rangle \ldots \sum_{l_f} \langle \varphi^{(f)}_{j_f} \,|\, h^{(f)}_r \,|\, \varphi^{(f)}_{l_f} \rangle A_L \\ =& \sum_L \mathcal{K}_{JL} A_L \,, \end{aligned} \tag{68}$$

where we have implicitly defined the *Hamiltonian matrix* $\boldsymbol{\mathcal{K}}$. (Contrary to Eq. (67), here "…" does contain l_κ.) Note that due to the product form of the Hamiltonian, the action of $\boldsymbol{\mathcal{K}}$ on $\boldsymbol{A}$ requires only sfn^{f+1} operations rather than n^{2f}. Moreover, the evaluation of all the matrix elements of the single-particle operators $h^{(\kappa)}_r$ takes only sfn^2N operations, whereas a direct multi-dimensional integration would require N^f operations (see Sec. 4.3). These numbers emphasise the importance of the product representation.

Also recognise that $\boldsymbol{\mathcal{K}}$ depends on the single-particle functions, which in turn depend on the MCTDH coefficients, making Eq. (68) non-linear. The working equations for the single-particle functions, Eq. (38), are also non-linear, among other reasons because of the projection operator $P^{(\kappa)}$.

4.3 Time-dependent and Correlation DVR

Rather than expanding the Hamiltonian into a sum of products of single-particle operators, as described in Sec. 4.2, it is of course also possible to directly evaluate the matrix elements $\langle\Phi_J\,|\,V\,|\,\Phi_L\rangle$, using the fact that the potential energy operator $V(Q^{(1)},\dots,Q^{(f)})$ is taken as diagonal in the primitive DVR basis $\{\,\chi^{(\kappa)}_{\alpha}(Q^{(\kappa)})\,\}$,

$$\langle\chi^{(1)}_{\alpha_1}\dots\chi^{(f)}_{\alpha_f}\,|\,V\,|\,\chi^{(1)}_{\beta_1}\dots\chi^{(f)}_{\beta_f}\rangle = V\left(Q^{(1)}_{\alpha_1},\dots,Q^{(f)}_{\alpha_f}\right)\delta_{\alpha_1\beta_1}\dots\delta_{\alpha_f\beta_f}\,. \tag{69}$$

(See App. B for the definition of $\chi^{(\kappa)}_{\alpha_\kappa}$.) Thus the potential energy matrix can be generated by transforming from the single-particle function basis to the DVR basis, multiplying by the potential energy function at the grid points, and transforming back. This transformation however means that N^f evaluations need to be made to evaluate the integrals required for the mean-fields and A-coefficient equations of motion.

A method has therefore been introduced where the basic idea of a DVR basis is used, but instead of using the N^f points of the primitive DVR grid, a smaller set of *time-dependent DVR* (TDDVR) points is used. These points are obtained from the eigenvalues $x^{(\kappa)}_j$ and eigenfunctions $X^{(\kappa)}_j(Q^{(\kappa)})$ of the position operator $\hat{Q}^{(\kappa)}$ in the time-dependent basis of the single-particle functions [28,87],

$$\langle\varphi^{(\kappa)}_j\,|\,\hat{Q}^{(\kappa)}\,|\,\varphi^{(\kappa)}_l\rangle = \sum_{k=1}^{n_\kappa}\langle\varphi^{(\kappa)}_j\,|\,X^{(\kappa)}_k\rangle\,x_k\,\langle X^{(\kappa)}_k\,|\,\varphi^{(\kappa)}_l\rangle\,. \tag{70}$$

Assuming that the potential operator is also diagonal on the product grid $x^{(1)}_{j_1},\dots,x^{(f)}_{j_f}$, these points can be used in place of the primitive DVR grid points $Q^{(1)}_{\alpha_1},\dots,Q^{(f)}_{\alpha_f}$. Matrix elements of the potential are then computed as

$$\langle X^{(1)}_{j_1}\dots X^{(f)}_{j_f}\,|\,V\,|\,X^{(1)}_{l_1}\dots X^{(f)}_{l_f}\rangle = V\left(x^{(1)}_{j_1},\dots,x^{(f)}_{j_f}\right)\delta_{j_1l_1}\dots\delta_{j_f\,l_f}\,. \tag{71}$$

As a result, after transformation from the single-particle basis to the TDDVR basis $\{\,|X_j\rangle\,\}$, only n^f evaluations are required.

Unfortunately, this method can result in inaccurate evaluation of the integral (69) due to the small number of points used. In particular, analysis by

Manthe has shown that separable parts of the potential energy function are poorly represented by this scheme. This analysis lead to the introduction of the *correlated DVR* (CDVR) scheme [55]. Here, an additional correction term

$$\sum_{\kappa=1}^{f} \Delta V_\kappa \, \delta_{j_1 l_1} \ldots \delta_{j_{\kappa-1} l_{\kappa-1}} \delta_{j_{\kappa+1} l_{\kappa+1}} \ldots \delta_{j_f \, l_f} \tag{72}$$

is added to the right hand side of Eq. (71), where

$$\begin{aligned} \Delta V_\kappa = & \langle X^{(\kappa)}_{j_\kappa} \,|\, V\left(x^{(1)}_{j_1}, \ldots, x^{(\kappa-1)}_{j_\kappa -1}, Q^{(\kappa)}, x^{(\kappa+1)}_{j_\kappa+1}, \ldots, x^{(f)}_{j_f}\right) |\, X^{(\kappa)}_{l_\kappa} \rangle \\ & - V\left(x^{(1)}_{j_1}, \ldots, x^{(f)}_{j_f}\right) \delta_{j_\kappa l_\kappa} \, . \end{aligned} \tag{73}$$

This term in effect corrects for the finite width of the TDDVR basis functions, and separable parts of the potential energy operator are treated accurately. Even so, the method suffers from the disadvantage that it is not possible to know the error that is being made in the integration.

Our experience with the CDVR method is rather mixed. For some systems it performed excellently (see Sec. 9.1), for others it did not work at all well. We hence ceased using it. However, when the propagation time is comparatively small and high accuracy is not required CDVR has found to work satisfactorily [43]. We consider the development of CDVR as a very important contribution since it removes the requirement that the Hamiltonian is given in product form. We hope that CDVR can be further developed to become more accurate and in particular to contain an error estimating control. As a final note, CDVR unfortunately cannot be used when there are multi-mode single-particle functions (see Sec. 4.5), because there is in general no multi-dimensional DVR. This excludes the use of CDVR when treating larger systems ($f > 10$, say).

4.4 Numerical scaling in brief

Although the MCTDH working equations are rather complicated, their use is in general advantageous because there are fewer differential equations to be solved compared with the standard method described in Sec. 2.2. To see this let us investigate the computational effort required to evaluate the right hand side of the working equations (37) and (38). We define the effort as the number of floating point operations to be carried out and consider only the most important terms. In the following we will assume for simplicity that the single-particle functions are represented on a DVR grid. We also assume that the number of grid points or primitive basis functions, N, as well as the number of single-particle functions, n, does not depend on the particular degree of freedom κ. Alternatively, one may consider N and n as the geometric means of the N_κ and n_κ, respectively. Notice that in the MCTDH applications N is typically much larger than n.

The effort of the MCTDH algorithm can be split up into two parts with different scaling behaviour. For small values of n and f, that is for systems with comparatively little correlation and few degrees of freedom, the dominant contribution to the computational effort stems from the calculation of the action of the single-particle operators $h_r^{(\kappa)}$ on the single-particle functions $\varphi_j^{(\kappa)}$. This effort grows linearly with the number of degrees of freedom and is proportional to $sfnN^2$, where s is the number of terms in the Hamiltonian expansion (64).

For systems where n and f are large, the calculation of the derivative of the MCTDH coefficients and in particular the mean-field matrices determines the numerical cost, which scales exponentially with the number of modes f. The effort for computing the mean-field matrices is proportional to sf^2n^{f+1}. The cost to determine the time-derivative (68) of the MCTDH coefficients scales with sfn^{f+1}. Note, however, that the right hand side of Eq. (68) is evaluated in almost the same way as the mean-field matrix elements $\mathcal{H}_{rjl}^{(\kappa)}$, Eq. (67), which allows the computation of $i\dot{\boldsymbol{A}}$ as a by-product of the calculation of the mean-field matrices with only little additional cost. Combining the two terms, the total numerical effort is therefore

$$\text{effort} \approx c_1 sfnN^2 + c_2 sf^2n^{f+1}\,, \tag{74}$$

using coefficients of proportionality, c_1 and c_2.

For comparison, in the standard method discussed in Sec. 2.2 the effort is proportional to fN^{f+1}. For systems with large values of n and f, the gain factor of the MCTDH scheme with respect to the standard method is hence proportional to $s^{-1}f^{-1}(N/n)^{f+1}$. Consequently, the MCTDH scheme is superior to the standard method if the number of degrees of freedom as well as the *contraction efficiencies* N_κ/n_κ, and in particular the mean contraction efficiency N/n, are sufficiently large.

For calculations of large systems, a more important factor than numerical efficiency is the computer memory required. This is dominated by the number of values needed to describe the wavefunction. Hence the memory required by the standard method is proportional to N^f. In contrast, memory needed by the MCTDH method scales as

$$\text{memory} \sim fnN + n^f\,, \tag{75}$$

where the first term is due to the (single-mode) single-particle function representation, and the second term the wavefunction coefficient vector $\boldsymbol{A}$. As $n < N$, often by a factor of five or more, the MCTDH method needs much less memory than the standard method, so allowing larger systems to be treated.

The importance of the memory requirements for large systems can be easily seen by looking at what would be needed for studying the dynamics of the pyrazine molecule ($C_4H_4N_2$). This system has 25 degrees of freedom (24 vibrational modes and a set of electronic states). Although in a study we have performed [36] the mean grid length for the degrees of freedom was only $N \approx 7.4$, the corresponding direct product grid consists of about 10^{21} points making the use of the standard method totally infeasible. Unfortunately, the MCTDH method as presented above, using a set of single-particle functions per degree of freedom, is also unable to treat this system: the program requires memory equivalent to approximately 12 vectors of the length specified in Eq. (75), double precision complex, and so with only 2 single-particle functions per mode the calculation would need $2^{25} \times 12 \times 16$ Bytes ≈ 6.1 GB.

The memory requirements can however be reduced if single-particle functions are used that describe a set of degrees of freedom, rather than just one. The wavefunction ansatz, Eq. (19), is then rewritten as a multi-configuration over p generalised "particles",

$$\Psi(q_1, \ldots, q_p, t) = \sum_{j_1=1}^{\tilde{n}_1} \cdots \sum_{j_p=1}^{\tilde{n}_p} A_{j_1 \ldots j_p}(t) \prod_{\kappa=1}^{p} \varphi_{j_\kappa}^{(\kappa)}(q_\kappa, t) \,, \tag{76}$$

where $q_\kappa = (Q_i, Q_j, \ldots)$ is the set of coordinates combined together in a single particle, described by $\tilde{n}_\kappa$ functions, termed *multi-mode* single-particle functions to distinguish them from the usual *single-mode* single-particle functions.

By combining d degrees of freedom together to form a set of $p = f/d$ particles, the memory requirement changes to

$$\text{memory} \sim p\tilde{n}N^d + \tilde{n}^p \,, \tag{77}$$

where $\tilde{n}$ is the number of multi-mode functions needed for the new particles. For large systems, the second term dominates this equation. Thus if

$$\tilde{n} < n^d, \tag{78}$$

i.e. the number of multi-mode functions is less for a multi-dimensional particle than the product of single-mode functions needed for the separate degrees of freedom, there can be a large saving in memory required.

The inequality (78) will in general be true. This comes from the fact that the number of single-particle functions required is related to the strength of coupling between the particle and the rest of the system. By combining modes, this coupling is reduced as the coupling between the combined degrees of freedom is now treated within the single-particle functions for the combined mode. Consider a system with a set of coupled modes. The coupling will lead to a wavefunction which is poorly described by a Hartree product, and many single-mode functions would be needed. In contrast, combining all the degrees of freedom together into one particle, only one single-particle function will be required: the standard numerically exact wavefunction.

To summarise, if only single-mode functions are used, i.e. $d = 1$, the memory requirement, Eq. (77), is dominated by the number of A-coefficients, n^f. By combining degrees of freedom together this number can be reduced, but at the expense of longer product grids required to describe the now multi-mode single-particle functions. At the extreme of all degrees of freedom combined together, the first term in Eq. (77) then dominates as N^f. Between these two extremes however, there is an optimally small amount of memory required.

At the same time, by combining modes, the effort equation is changed from Eq. (74) to

$$\text{effort} \approx c_1 spd\tilde{n}N^{d+1} + c_2 sp^2\tilde{n}^{p+1} \,, \tag{79}$$

where the first term is larger than before, while the second term is smaller. Again one sees the penalty of combining modes: the extra effort needed due to the longer single-particle function grids. For this reason combining modes is not recommended for small systems, unless two degrees of freedom are very strongly coupled [52]. For large systems however, the effect is significant, and enables the 25 degree of freedom pyrazine system to be studied [36–38].

4.6 Effort of the single- and multi-set formulation

In our discussion in Sec. 4.4 on the numerical scaling of the MCTDH scheme we have implicitly assumed a system which involves only a single potential energy surface. Now we shall compare the effort of the single- and multi-set approaches introduced in Sec. 3.5. In order to understand which of the two formalisms is computationally more efficient, it is necessary to know how the expansion (64) of the residual Hamiltonian looks like in each formulation. In the multi-set formalism the single-particle operator $h_r^{(\alpha\beta,\kappa)}$ depends explicitly on the initial electronic state β the operator acts on, as well as on the final state α the result belongs to. Therefore, if two products $h_r^{(\alpha\beta,1)} \cdot \ldots \cdot h_r^{(\alpha\beta,f)}$ and $h_r^{(\alpha'\beta',1)} \cdot \ldots \cdot h_r^{(\alpha'\beta',f)}$ of single-particle operators are equal but couple different initial or final states, i.e. $\alpha \neq \alpha'$ or $\beta \neq \beta'$, as is for example typically the case for a kinetic energy term, both must be listed in the expansion of the residual Hamiltonian. This is different for the single-set formalism, where the κ_eth mode labels the σ electronic states. The corresponding single-particle operator $h_r^{(\kappa_e)}$ is then a $\sigma \times \sigma$ matrix the diagonal elements of which specify on which states the rth expansion term acts, while the off-diagonal elements define which states are being coupled. By setting more than one matrix element unequal to zero it is possible to combine into one single-set expansion term those multi-set terms that refer to different initial or final electronic states but are otherwise equal.

Comparing both formalisms, one finds that the multi-set formulation has the disadvantages that σ sets of single-particle functions (rather than just one) must be propagated, that — as we have just seen — the number of Hamiltonian expansion terms is generally larger, and that more mean-field matrices have to be determined for each term r and mode κ, namely σ^2 instead of only one. The multi-set formulation has, on the other hand, two important advantages. First, since a separate set of functions is used for each electronic state, the number of single-particle functions per state that is required for convergence is typically smaller than in the single-set formulation. This is because each set of single-particle functions individually adapts itself to the wavepacket of the corresponding state. Note that the number of single-particle functions per state contributes to the exponentially growing effort of the MCTDH algorithm, while the number of sets only affects the linearly scaling parts (see Sec. 4.4). The second advantage results from the computation of the mean-field matrices and the time-derivative of the MCTDH coefficients, Eqs. (67) and (68). In the single-set formulation the $\langle \varphi^{(\kappa)} \mid h_r^{(\kappa)} \mid \varphi^{(\kappa)} \rangle$ matrices have to be multiplied for each expansion term with the full A-vector, i.e. the vector that contains the MCTDH coefficients of all electronic states, whereas in the multi-set formulation only the shorter $A^{(\alpha)}$-vector (see Eqs. (61) and (63)) of the αth state is involved in this multiplication. These advantages favour the multi-set approach in many cases [35–37,54], which is thus the preferable method when non-adiabatic systems are investigated within the MCTDH scheme.

4.7 Complex absorbing potentials

To motivate the use of complex absorbing potentials, let us consider a scattering event in one dimension. One part of the wavepacket has already left the interaction region and is in free motion. The other part is still in the strong interaction region. When the first part of the wavepacket reaches the end of the grid it will be reflected (or it enters the other side of the grid when periodic boundary conditions are assumed, e.g. if an FFT primitive basis is used), and hence the description of the relevant part of the wavefunction will be deteriorated. To avoid the use of extremely long grids one may annihilate the free part of the wavepacket just before it reaches the end of the grid. For this purpose Leforestier and Wyatt [88], and later Kosloff and Kosloff [89], established *complex absorbing potentials* (CAPs). In the following decade the use of CAPs became more and more widespread. CAPs have been used to compute the complex Siegert eigenenergies of resonance states by diagonalising the CAP augmented Hamiltonian [90–92]. Neuhauser and Baer [93–95] introduced CAPs into the field of reactive scattering. Here CAPs are particularly useful because they enable the use of the reactant coordinate set alone throughout the calculation. Seideman and Miller [96,97] have used CAPs to compute Green's functions. Note that CAPs are also known under the names *negative imaginary potential* (NIP), *absorbing boundary condition* (ABC) or (somewhat misleadingly) *optical potential.*

The introduction of a CAP is an artificial change of the Hamiltonian and one must be careful to ensure that this modification does not change the relevant physics. In fact, a CAP does not only annihilate the wavefunction but also produces (unwanted) reflections. These reflections can be kept negligibly small by making the CAP sufficiently weak and long. The performance of CAPs has been carefully analysed in Refs. [92,98–100], and here we merely note that within MCTDH monomial CAPs have been used exclusively, i.e. CAPs of the form

$$-iW(Q) = -i\,\eta\,(Q - Q_c)^b\,\theta(Q - Q_c)\,, \tag{80}$$

where the exponent is usually set to $b = 2$ or $b = 3$. The symbol $\theta(x)$ denotes Heaviside's step function and Q_c is the point where the CAP is switched on, i.e. Q_c and the end of the grid determine the length of the CAP. The CAP strength η and the CAP length are chosen according to the rules given in Ref. [99]. The CAP $-iW(Q_\kappa)$ is then added to the Hamiltonian, typically to the separable part $h^{(\kappa)}$ (see Eq. (42)). If however the constraint $g^{(\kappa)} = h^{(\kappa)}$ is used (cf. Sec. 3.2), the CAP has to be included in the residual part H_R. This is because the $g^{(\kappa)}$ must be Hermitian operators.

CAPs have been found to be very useful in MCTDH calculations despite the fact that the computational labour of an MCTDH calculation is relatively insensitive to the grid lengths. They have been used in MCTDH calculations not only to keep the grid lengths small, but also to analyse the wavepacket and to determine cross-sections. This is discussed in Sec. 8.6.

4.8 Projector and density matrix

The MCTDH equations of motion as derived in Sec. 3.1 have to be slightly modified for numerical reasons. The first change concerns the projection operator $P^{(\kappa)}$. This projector ensures the constraints (21) and (22) and preserves the orthonormality of the single-particle functions during the propagation. If the single-particle functions however become non-orthonormal due to inaccuracies of the integration, $P^{(\kappa)}$, as defined by Eq. (24), ceases to be a projector, and even an exact solution of Eq. (38) will then further destroy the orthonormality. A cure to this numerical problem is to define the projector as

$$P^{(\kappa)} = \sum_{j,l=1}^{n_\kappa} |\varphi_j^{(\kappa)}\rangle \left(\left(\boldsymbol{\mathcal{O}}^{(\kappa)}\right)^{-1}\right)_{jl} \langle\varphi_l^{(\kappa)}|\,, \tag{81}$$

where $\mathcal{O}_{jl}^{(\kappa)} = \langle\varphi_j^{(\kappa)}|\varphi_l^{(\kappa)}\rangle$ is the overlap matrix of the single-particle functions. Equation (81) defines an orthonormal projector as long as the single-particle functions are linearly independent; their orthonormality is not required.

The second modification refers to the density matrix $\boldsymbol{\rho}^{(\kappa)}$, Eq. (27). The eigenvalues or natural populations (see Sec. 3.3) of $\boldsymbol{\rho}^{(\kappa)}$ characterise the importance of the corresponding eigenfunctions or natural orbitals. If there is a natural orbital (i.e. a linear combination of the single-particle functions) that does not contribute to the MCTDH wavefunction, the density matrix will become singular and may be replaced by a regularised one, such as

$$\boldsymbol{\rho}_{\text{reg}}^{(\kappa)} = \boldsymbol{\rho}^{(\kappa)} + \varepsilon \exp\left(-\boldsymbol{\rho}^{(\kappa)}/\varepsilon\right)\,, \tag{82}$$

with ε being a small number. (The setting of ε is not very critical. Reasonable values range from $\varepsilon = 10^{-8}$ to $\varepsilon = 10^{-14}$, depending on the chosen accuracy of the integrator.) When complex absorbing potentials (see Sec. 4.7) are employed, the wavefunction vanishes for large times. To compensate for this, ε is weighted with the squared norm of the wavefunction, i.e. ε is replaced by $\varepsilon\,\mathrm{tr}(\boldsymbol{\rho}^{(\kappa)})$. Note that the regularisation changes only the time evolution of those natural orbitals that are very weakly populated; the time evolution of the natural orbitals important for the description of the wavefunction remains unchanged. A regularisation similar to the one discussed has to be applied to Eq. (52) when propagating in natural orbitals.

5 MCTDH: Integration schemes

The efficiency and accuracy of the MCTDH method strongly depends on the algorithm used for solving the equations of motion (37) and (38) introduced in Sec. 3.1. This section therefore addresses the integration of the MCTDH working equations.[2]

5.1 The variable mean-field (VMF) integration scheme

As noted in Sec. 4.2, the MCTDH equations of motion (37) and (38) form a system of coupled non-linear ordinary differential equations of first order. The non-linearity of the equations inhibits their integration by such powerful integrators as the Chebyshev [62] or short iterative Lanczos [63] scheme. A straightforward and easy to implement way to solve this problem is to employ an all-purpose integration method [101,102] instead. To distinguish this approach from that described below, it is called the *variable mean-field* (VMF) scheme. In the VMF scheme, of all the integrators that have been tested an Adams-Bashforth-Moulton (ABM) predictor-corrector turned out to perform most efficiently in integrating the complete set (37) and (38) of differential equations. The VMF approach has been applied in the majority of calculations to date.

The VMF scheme is not the optimal method for solving the MCTDH equations, because the wavefunction — i.e. the A-vector and the single-particle functions — contains components that are highly oscillatory in time. This eventually enforces small integration steps, at each of which the density and mean-field matrices have to be computed. For larger systems the frequent calculation of these quantities contributes to the dominant part to the computational effort, since the effort for these calculations grows exponentially with the number of degrees of freedom (see Sec. 4.4). One therefore expects a significant speed-up of the MCTDH algorithm by employing an integration scheme that is specifically tailored to the solution of the MCTDH equations of motion. Such a method is discussed in the subsequent Sec. 5.2.

5.2 The constant mean-field (CMF) integration scheme

An integration scheme which has proved to be both efficient and robust in solving the MCTDH working equations is known as the *constant mean-field* (CMF) integrator [54].

---

[2] Parts of the text and all figures of this chapter have been reprinted from Ref. [54] with kind permission of Springer-Verlag, Heidelberg, who holds the copyright of that reference.

5.2.1 The concept behind CMF

The motivation behind the CMF integration scheme is that the matrix elements $\mathcal{K}_{JL} = \langle \Phi_J \mid H \mid \Phi_L \rangle$, and the product of the inverse density and the mean-field matrices, $\left(\boldsymbol{\rho}^{(\kappa)}\right)^{-1} \boldsymbol{\mathcal{H}}_r^{(\kappa)}$, generally change much slower in time than the MCTDH coefficients and the single-particle functions. For that reason it is possible to use a wider meshed time discretisation for the propagation of the former quantities than for the latter ones with only a minor loss of accuracy. In other words, during the integration of the equations of motion (37) and (38) one may hold the Hamiltonian matrix elements, the density matrices, and the mean-field matrices constant for some time τ (hence the name).

This concept shall now be discussed in more detail. For the sake of simplicity we first consider a simplified variant that already demonstrates most of the properties and advantages of the integrator. The actual integration scheme is somewhat more subtle and is described in the subsequent Sec. 5.2.2. An integration step in this simplified variant begins with the initial values $\boldsymbol{A}(t_0)$ and $\boldsymbol{\varphi}^{(\kappa)}(t_0)$ being employed to determine the Hamiltonian matrix $\boldsymbol{\mathcal{K}}(t_0)$ (Eq. (68)), the regularised density matrices $\boldsymbol{\rho}^{(\kappa)}(t_0)$ (Eqs. (27) and (82)), and the mean-field matrices $\boldsymbol{\mathcal{H}}_r^{(\kappa)}(t_0)$ (Eq. (67)). With these matrices kept constant, the wavefunction is then propagated from t_0 to $t_1 = t_0 + \tau$. The propagated values $\boldsymbol{A}(t_1)$ and $\boldsymbol{\varphi}^{(\kappa)}(t_1)$ are used to compute $\boldsymbol{\mathcal{K}}(t_1)$, $\boldsymbol{\rho}^{(\kappa)}(t_1)$, and $\boldsymbol{\mathcal{H}}_r^{(\kappa)}(t_1)$. This procedure is re-iterated until the desired final point of time is reached.

Using for simplicity the constraint operators $g^{(\kappa)} = 0$ (see Sec. 3.2) and the single-set formulation (see Sec. 3.5) the *CMF equations of motion* then read

$$i\dot{A}_J(t) = \sum_L \bar{\mathcal{K}}_{JL} A_L(t) \tag{83}$$

$$\begin{aligned}
i\dot{\varphi}_j^{(1)}(t) &= \left(1 - P^{(1)}\right) \left(h^{(1)} \varphi_j^{(1)}(t) + \sum_{k,l=1}^{n_1} \left(\bar{\rho}^{(1)\,-1}\right)_{jk} \sum_{r=1}^{s} \bar{\mathcal{H}}_{rkl}^{(1)} h_r^{(1)} \varphi_l^{(1)}(t) \right) \\
\vdots \qquad & \qquad\qquad\qquad\qquad \vdots \\
i\dot{\varphi}_j^{(f)}(t) &= \left(1 - P^{(f)}\right) \left(h^{(f)} \varphi_j^{(f)}(t) + \sum_{k,l=1}^{n_f} \left(\bar{\rho}^{(f)\,-1}\right)_{jk} \sum_{r=1}^{s} \bar{\mathcal{H}}_{rkl}^{(f)} h_r^{(f)} \varphi_l^{(f)}(t) \right) .
\end{aligned} \tag{84}$$

The bar indicates that the corresponding term is evaluated at the time $t_m = t_0 + m\tau$, with m being the number of steps made so far, and is then held constant over the CMF integration step $t_m \leq t \leq t_{m+1}$. Analogous equations hold for the multi-set formulation and other constraint operators.

Supposing that a comparatively large step size τ can be chosen, the CMF integration scheme has several advantages. First of all, the density and mean-field matrices have to be set up less frequently. Since for systems with many configurations (23) and a long expansion of the Hamiltonian (64) the calculation of the mean-field matrices dominates the numerical effort, the CMF integrator can significantly reduce the computation time. The overhead created by the product form (64) of the Hamiltonian is also diminished.

Another important characteristic of the CMF scheme lies in the simplified structure of the system of differential equations. While the MCTDH equations (37) and (38) are coupled, the CMF equations (83) and (84) separate into $f+1$ disjoined subsystems. One of these subsystems is for the MCTDH coefficients, the others are for each of the f single-particle vectors $\boldsymbol{\varphi}^{(\kappa)}$, Eq. (39). Splitting a large system of differential equations into smaller ones generally lessens the computational effort because the step size can then be adapted independently for each subsystem; if one subsystem requires small integration steps, the others remain unaffected. Furthermore, the decoupling of the working equations allows the integration of each subsystem with a different accuracy. For example, since for molecules with many degrees of freedom the effort for the propagation of the single-particle functions can often be neglected, one might integrate the set of equations (84) with high precision, while demanding only a moderate accuracy for the expensive integration of the MCTDH expansion coefficients, Eq. (83).

Finally, we point out that the working equation (83) for the A-vector is linear with constant coefficients, which permits its solution by integrators explicitly designed for equations of that kind [9], such as the Chebyshev [62] or Lanczos [63] method. This further enlarges the efficiency of the CMF approach. The set of equations (84) for the single-particle functions is, however, still non-linear due to the projection operator $P^{(\kappa)}$.

5.2.2 The second-order CMF scheme

Despite all its advantages, the simplified variant of the CMF integration scheme depicted in the previous Sec. 5.2.1 has to be improved further in order to be competitive. One reason is that in its current form the method defines — analogous to Euler's rule — a first-order integrator, which is known to perform quite poorly. Another reason is that the above scheme lacks a means of estimating the discretisation error and adjusting the step size τ. The following modifications of the method eliminate these shortcomings.

The actual CMF integration scheme is depicted in Fig. 1. This diagram displays a step of size τ from time $t = 0$ to $t = \tau$. $\bar{\boldsymbol{\mathcal{K}}}(t)$, $\bar{\boldsymbol{\rho}}^{-1}(t)$, and $\bar{\boldsymbol{\mathcal{H}}}(t)$ denote the Hamiltonian matrix, the inverse density and the mean-field matrices, respectively, evaluated at the time t and held constant during the integration step (we have dropped the superscript κ for simplicity). First, the wavefunction at time $t = 0$ is used to determine $\bar{\boldsymbol{\mathcal{K}}}(0)$, $\bar{\boldsymbol{\rho}}^{-1}(0)$, and $\bar{\boldsymbol{\mathcal{H}}}(0)$. Then both the MCTDH coefficients (step 1 in the figure) and the single-particle functions (step 2) are propagated from $t = 0$ to $t = \tau/2$ according to Eqs. (83)

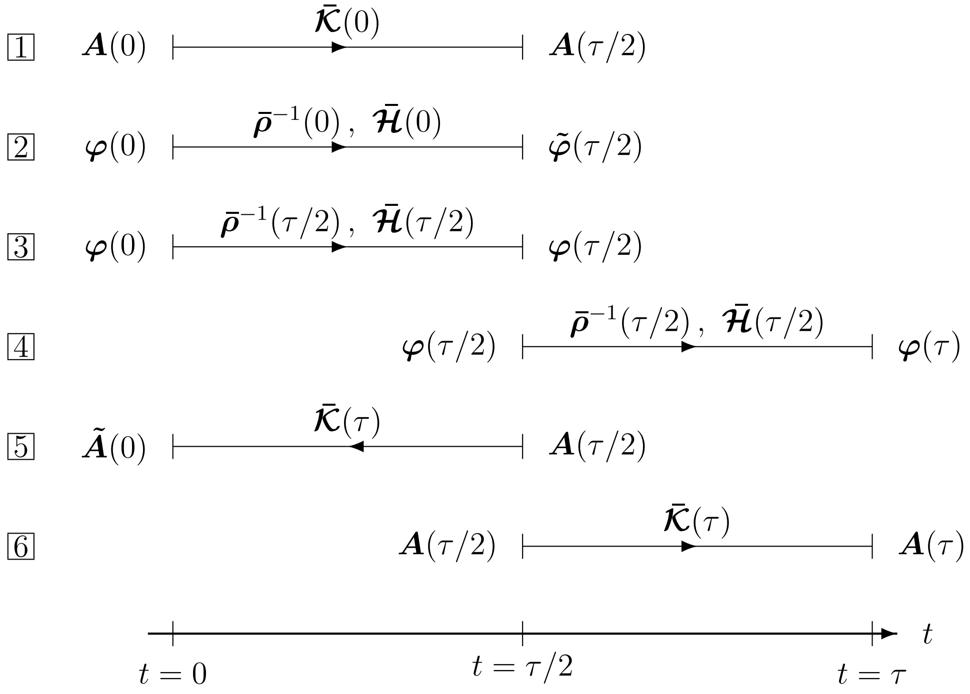

Fig. 1. Diagrammatic description of the second-order CMF scheme. See Sec. 5.2.2 for details.

and (84), yielding $\boldsymbol{A}(\tau/2)$ and $\tilde{\boldsymbol{\varphi}}(\tau/2)$. With this propagated wavefunction the advanced $\bar{\boldsymbol{\rho}}^{-1}(\tau/2)$ and $\bar{\boldsymbol{\mathcal{H}}}(\tau/2)$ are computed and employed in a second propagation of the single-particle functions from $t = 0$ to $t = \tau/2$ (step 3), resulting in $\boldsymbol{\varphi}(\tau/2)$. The difference between $\boldsymbol{\varphi}(\tau/2)$ and $\tilde{\boldsymbol{\varphi}}(\tau/2)$ measures the error of the single-particle functions caused by the discretisation. We will soon address this error in detail, but for the moment it is sufficient to know that if this error is too large, the integration step made so far is rejected and repeated with a smaller step size τ, otherwise the step is accepted and $\boldsymbol{\varphi}$ is propagated to the end of the interval, $t = \tau$, (step 4). The knowledge of $\boldsymbol{\varphi}(\tau)$ allows the calculation of the Hamiltonian matrix $\bar{\boldsymbol{\mathcal{K}}}(\tau)$. To obtain an error estimate for the MCTDH coefficients, $\boldsymbol{A}(\tau/2)$ is then propagated backwards in time from $t = \tau/2$ to $t = 0$ employing $\bar{\boldsymbol{\mathcal{K}}}(\tau)$ (step 5), leading to $\tilde{\boldsymbol{A}}(0)$. Again, the difference between the initial $\boldsymbol{A}(0)$ and $\tilde{\boldsymbol{A}}(0)$ is linked to the error of the coefficients and is used to decide whether to reject or accept the integration step. In the latter case, $\boldsymbol{A}(\tau/2)$ is propagated over the second half of the interval (step 6), yielding $\boldsymbol{A}(\tau)$. The step is completed by the calculation of $\bar{\boldsymbol{\rho}}^{-1}(\tau)$ and $\bar{\boldsymbol{\mathcal{H}}}(\tau)$.

The CMF equations of motion (83,84) were derived using the constraint operators $g^{(\kappa)} = 0$. As has been outlined in Sec. 3.2, this implies that the motion of the single-particle functions is minimised. Alternatively, one may employ the constraints $g^{(\kappa)} = h^{(\kappa)}$, where $h^{(\kappa)}$ is the separable part of the Hamiltonian, Eq. (42). However, the resulting set of equations of motion, i.e. the CMF formulation of Eqs. (43) and (44), has been found empirically to be often less efficient than the one presented here [54]. It has, on the other hand, the advantage that the separable part of the Hamiltonian, $h^{(\kappa)}$, is treated exactly, in contrast to Eqs. (83) and (84). This may favour the use of these constraints in some cases.

5.2.3 Error estimate and step size control

In this section we will outline how the error estimate and the step size control are implemented in the CMF scheme. For a comprehensive discussion of this subject we refer the reader to Ref. [54].

Controlling the CMF step size requires the knowledge of how the differences $\Delta\boldsymbol{A} = \boldsymbol{A} - \tilde{\boldsymbol{A}}$ and $\Delta\boldsymbol{\varphi}^{(\kappa)} = \boldsymbol{\varphi}^{(\kappa)} - \tilde{\boldsymbol{\varphi}}^{(\kappa)}$ are connected to the error of the wavefunction. Let Ψ and $\tilde{\Psi}$ denote two MCTDH wavefunctions, Eq. (19). Expanding the difference between Ψ and $\tilde{\Psi}$, one obtains (after some algebra) in lowest order

$$\| \Psi - \tilde{\Psi} \|^2 = \| \Delta\boldsymbol{A} \|^2 + \sum_{\kappa=1}^{f} \mathrm{tr}\left(\Delta\boldsymbol{\mathcal{O}}^{(\kappa)} \boldsymbol{\rho}^{(\kappa)\,T} \right) , \tag{85}$$

with $\Delta\mathcal{O}_{jl}^{(\kappa)} = \langle \Delta\varphi_j^{(\kappa)} \mid \Delta\varphi_l^{(\kappa)} \rangle$. Setting $\Delta\boldsymbol{\varphi} = \boldsymbol{\varphi}(\tau/2) - \tilde{\boldsymbol{\varphi}}(\tau/2)$ and $\Delta\boldsymbol{A} = \boldsymbol{A}(0) - \tilde{\boldsymbol{A}}(0)$ one can thus define the CMF discretisation error δ, which is essentially given by Eq. (85), of the MCTDH wavefunction. To devise an automatic step size control one computes this error estimate δ after each CMF step and sets the new CMF step size τ_{new} to

$$\tau_{\mathrm{new}} = \tau \sqrt[4]{\epsilon/\delta} \, , \tag{86}$$

where τ is the current step size and ϵ is a suitable error tolerance. The fourth root is due to the fact that the CMF scheme defines a second-order integration method, i.e. $\| \Psi - \tilde{\Psi} \| \sim \tau^2$.

A detailed study of the CMF step size control has been performed in Ref. [54]. In that work both the VMF and the CMF integrator were applied to the photodissociation process of methyl iodide, modeled by a system with five degrees of freedom evolving on three vibronically coupled diabatic potential energy surfaces. The error of the CMF scheme was determined by comparing the wavefunction obtained at the end of the propagation with that obtained using the VMF scheme. The result for five different error tolerances ϵ is displayed in Fig. 2. One finds that the error introduced by the CMF method is almost proportional to ϵ over a wide range of error tolerances . A similar correlation has also been observed for other systems. The automatic step size control

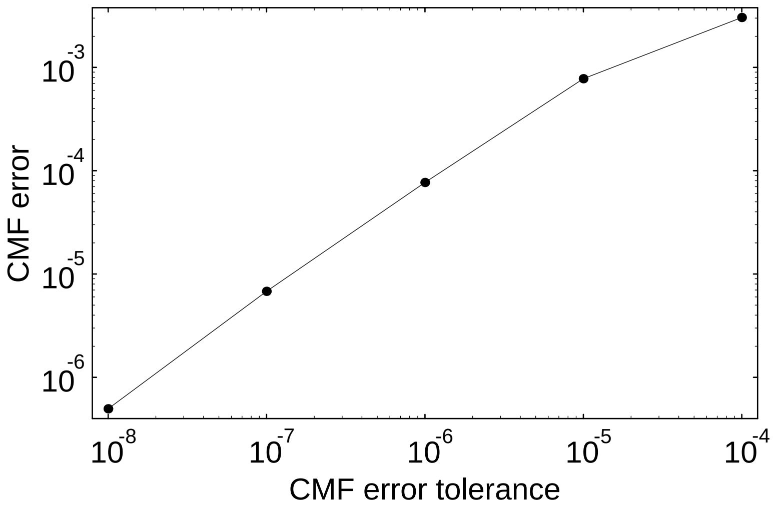

Fig. 2. The CMF error, defined as $\| \Psi_{\mathrm{VMF}} - \Psi_{\mathrm{CMF}} \|^2 \, / \, (\| \Psi_{\mathrm{VMF}} \|^2 + \| \Psi_{\mathrm{CMF}} \|^2)$, for the example system CH_3I propagated with five different error tolerances ϵ (the line only serves to guide the eyes). Ψ_{VMF} and Ψ_{CMF} stand for the wavefunction at the final time $t = 30$ fs, determined using the VMF and the CMF scheme, respectively.

hence allows one to directly influence the accuracy of the CMF integrator by varying the error tolerance. In particular, the integration error can easily be reduced below a desired limit by choosing ϵ appropriately. This strongly simplifies the handling of the CMF scheme.

5.2.4 Solving the CMF equations

We still need to comment on how the CMF equations of motion (83) and (84) are being integrated. For the propagation of the MCTDH coefficients one may take advantage of the linearity of Eq. (83) and employ a short iterative Lanczos (SIL) integrator with variable order. (If complex absorbing potentials are included in the Hamiltonian, then $\bar{\boldsymbol{\mathcal{K}}}$ is no longer Hermitian. In such a case the SIL–integrator is replaced by a Lanczos-Arnoldi integrator [103–105]. See App. C for more details on the SIL algorithm.)

The Lanczos scheme possesses several properties that make the CMF integrator not only efficient but also robust and easy to handle. For instance, in the SIL method no knowledge of the energy range and no energy shift of the Hamiltonian is required, and it is also less sensitive to large eigenvalues of the Hamiltonian than other polynomial methods. (For optimal numerical performance however it is still necessary to cut off large potential energy values.) Moreover, the Lanczos algorithm conserves the norm exactly, whereas in a VMF calculation the norm is generally not strictly conserved due to numerical inaccuracies. Finally, in order to estimate the integration error of the MCTDH coefficients, the CMF method needs a backward propagation of the

A-vector (step 5 in Fig. 1). The SIL–integrator permits the estimation of this error almost for free, as the Krylov space that has to be built for this back-propagation can also be used in the subsequent forward propagation (step 6).

Since Eq. (84) is non-linear, the Lanczos method cannot be applied to the single-particle functions. The predictor-corrector method used in the VMF scheme (see Sec. 5.1) is not very appropriate to the CMF scheme, because as a multistep method it must be restarted twice within each CMF step. To integrate Eq. (84) a Bulirsch-Stoer extrapolation method with variable order and step size, and polynomial extrapolation [102], has been recommended [54].

In addition to the various benefits of the simplified version of the CMF scheme underlined in Sec. 5.2.1, the second-order CMF method offers two further advantages. First, the CMF integrator enables one to control the discretisation error and adjust the step size. Without such an internal error control it would hardly be possible to apply the integrator to realistic problems where nothing is known about the exact solution. The second important improvement lies in increasing the order of the error term and thus allowing larger CMF steps.

The major disadvantage of the CMF strategy compared with the simplified scheme discussed in Sec. 5.2.1 is the one and a half fold increase in the effort of propagating the single-particle functions. For large systems however (i.e. for $n^f \gg N^2$) most of the computation time is typically spent on the propagation of the MCTDH coefficients, so that this additional cost is negligible.

We close this section in emphasising that the CMF integration scheme converges for $n \to N$ towards the standard method (see Sec. 2.2), since for $n = N$ both the single-particle functions and the mean-fields are constant. Moreover, the CMF integrator conserves the norm exactly.

5.2.5 Computational details

Attention to two numerical details significantly enhances the efficient implementation of the CMF integrator.

The first one concerns the propagation of the single-particle functions according to Eq. (84). As pointed out in Sec. 4.4 this dominates the numerical cost for small systems. Although the matrices $\bar{\boldsymbol{\mathcal{H}}}_r^{(\kappa)}$ are constant, the sum

$$\sum_{r=1}^{s} \bar{\mathcal{H}}_{rkl}^{(\kappa)} h_r^{(\kappa)} \varphi_l^{(\kappa)} \tag{87}$$

still has to be computed at each evaluation of the right hand side of Eq. (84). To see how one can avoid this summation we examine the value of the vector

(87) at the αth ($\alpha = 1, \ldots, N_\kappa$) grid point. Let $|\chi_\alpha^{(\kappa)}\rangle$ denote the corresponding DVR function (see App. B). Projecting (87) onto $|\chi_\alpha^{(\kappa)}\rangle$ and using the (numerical) completeness of the set of DVR functions, we obtain

$$\langle\chi_\alpha^{(\kappa)}|\sum_{r=1}^{s}\bar{\mathcal{H}}_{rkl}^{(\kappa)}h_r^{(\kappa)}|\varphi_l^{(\kappa)}\rangle = \sum_{\beta=1}^{N_\kappa}\left(\sum_{r=1}^{s}\bar{\mathcal{H}}_{rkl}^{(\kappa)}\langle\chi_\alpha^{(\kappa)}|h_r^{(\kappa)}|\chi_\beta^{(\kappa)}\rangle\right)\langle\chi_\beta^{(\kappa)}|\varphi_l^{(\kappa)}\rangle\,. \tag{88}$$

The number in brackets could in principal be determined for all κ, α, β, k and l only once at the beginning of each CMF step and then taken from memory. However, this would require the storage of fn^2N^2 complex numbers. Since most of the single-particle operators are potential terms and hence diagonal, it seems reasonable to save only these terms and continue treating the non-diagonal ones as before. For simplicity, let us assume that the Hamiltonian expansion terms are arranged such that the first s_κ are diagonal, i.e. $\langle\chi_\alpha^{(\kappa)}|h_r^{(\kappa)}|\chi_\beta^{(\kappa)}\rangle = \langle\chi_\alpha^{(\kappa)}|h_r^{(\kappa)}|\chi_\alpha^{(\kappa)}\rangle\delta_{\alpha\beta}$, whereas the other $s - s_\kappa$ are represented by full matrices. Expression (88) then reads

$$\begin{aligned}\langle\chi_\alpha^{(\kappa)}|\sum_{r=1}^{s}\bar{\mathcal{H}}_{rkl}^{(\kappa)}h_r^{(\kappa)}|\varphi_l^{(\kappa)}\rangle = {} & \mathcal{M}_{kl\alpha}^{(\kappa)}\langle\chi_\alpha^{(\kappa)}|\varphi_l^{(\kappa)}\rangle \\ & + \sum_{r=s_\kappa+1}^{s}\bar{\mathcal{H}}_{rkl}^{(\kappa)}\langle\chi_\alpha^{(\kappa)}|h_r^{(\kappa)}|\varphi_l^{(\kappa)}\rangle\,,\end{aligned} \tag{89}$$

with

$$\mathcal{M}_{kl\alpha}^{(\kappa)} = \sum_{r=1}^{s_\kappa}\bar{\mathcal{H}}_{rkl}^{(\kappa)}\langle\chi_\alpha^{(\kappa)}|h_r^{(\kappa)}|\chi_\alpha^{(\kappa)}\rangle\,. \tag{90}$$

Since $\bar{\boldsymbol{\mathcal{H}}}$ is constant, $\boldsymbol{\mathcal{M}}$ needs to be computed only initially at each CMF (half-) step. The numerical effort of calculating the diagonal part of sum (88) is then reduced by a factor of s_κ for each degree of freedom κ, diminishing the overhead due to the product form (64) of the residual Hamiltonian.

The second item refers to the adaptation of the step size. When the CMF integrator is applied to realistic problems, where the interest lies in calculating observable quantities, one usually needs the wavefunction Ψ at certain (typically equidistant) times t_m. According to the uncertainty principle, the distance $\Delta t = t_{m+1} - t_m$ between two neighbouring points must be chosen sufficiently small to resolve the full energy range. Since the step size τ is limited by $\tau \leq \Delta t$, this might affect the length of the CMF steps and hence reduce the integrator's efficiency. In those cases where the observables are determined using the auto-correlation function, a simple trick exists that enables one to double the output interval Δt. The preferable way to compute the auto-correlation function is given by Eq. (167). However, the auto-correlation function is then known solely at the times $2m\Delta t$ instead of $m\Delta t$ ($m = 0, 1, \ldots$). At the intermediate points $(2m-1)\Delta t$ the auto-correlation function can be obtained from $c((2m-1)\Delta t) = \langle \Psi^*((m-1)\Delta t) \,|\, \Psi(m\Delta t)\rangle$, if $\Psi((m-1)\Delta t)$ has been stored in memory. This permits the choice of a Δt which is twice as large as before.

5.2.6 Numerical effort

Having described the CMF integration scheme in detail, we shall estimate the expected speed-up of a CMF calculation compared with a VMF calculation. We restrict our discussion to large systems (i.e. $n^f \gg N^2$), where the dominant contribution to the numerical effort is caused by the computation of the mean-field matrices and the time-derivative of the MCTDH coefficients. We assume that in the VMF scheme the equations of motion are solved using a predictor-corrector routine that evaluates the differential equation twice in each step. As outlined in Sec. 4.4, this requires $2c_1 s f^2 n^{f+1}$ floating point operations per step, where c_1 is a proportionality constant. In a CMF calculation with a Lanczos integrator of mean order $\bar{l}$ used for the propagation of the MCTDH coefficients, $2c_1 s f^2 n^{f+1} + 2c_2 \bar{l} s f n^{f+1}$ floating point operations are needed for the two CMF half-steps. In our implementation of the code the constants c_1 and c_2 fulfil the relation $c_2 \approx 2c_1$. The gain of a CMF calculation with respect to a VMF calculation can hence be approximated by

$$\text{gain(CMF/VMF)} \approx \frac{f}{f + 2\bar{l}} \frac{\bar{\tau}_{\text{CMF}}}{\bar{\tau}_{\text{VMF}}} \,, \tag{91}$$

with $\bar{\tau}_{\text{CMF}}$ and $\bar{\tau}_{\text{VMF}}$ being the mean CMF and VMF (i.e. predictor-corrector) step sizes, respectively. In the limit $f \to \infty$ the gain is exclusively given by the ratio of the CMF and the VMF step size.

We also want to estimate the gain of the CMF scheme with respect to the standard method discussed in Sec. 2.2. To this end we assume that the equations of motion of the standard method are solved employing a Lanczos integrator. The SIL step size in the standard method will then be comparable to the size of a CMF half-step, and the mean SIL order $\bar{l}$ will also be similar in both schemes. (This is a rather conservative assumption since the matrix $\bar{\boldsymbol{\mathcal{K}}}$ used in the CMF scheme generally has a smaller spectral range than the Hamiltonian matrix employed in the standard method. This is because $\bar{\boldsymbol{\mathcal{K}}}$ is set up in the single-particle basis, which is better adapted to the potential than the primitive basis used in the standard method to represent the Hamiltonian matrix.) In the standard method the effort for each SIL step is given by $c_3 \bar{l} f N^{f+1}$, with $c_3 \approx c_2$. Thus one approximately obtains for the gain of a CMF calculation with respect to the standard method:

$$\text{gain(CMF/standard)} \approx \frac{2\bar{l}}{f + 2\bar{l}} \frac{1}{s} \left(\frac{N}{n}\right)^{f+1} \,. \tag{92}$$

A more careful analysis shows that the expression n^{f+1} should be interpreted as $f^{-1}(\sum_\kappa n_\kappa)(\prod_\kappa n_\kappa)$ (and similarly for N^{f+1}), and s should be taken as the number of non-separable Hamiltonian terms plus f^{-1} times the number of separable one-dimensional terms.

We see that the CMF scheme is superior — with regard to the computational effort — to the standard method provided that the number of modes f and the contraction efficiencies N_κ/n_κ are sufficiently large. A realistic example system with $f = 6$, $N = 30$, $n = 5$, $s = 50$, and $\bar{l} = 10$ shall illustrate this. For this system a calculation using the (brute force) standard method can be expected to take 4300 times longer than a CMF calculation. If the CMF run requires for this system, say, two hours of CPU time, the standard method would then need about one year! This shows that MCTDH can make investigations feasible that are impossible within the standard approach.

To complete our discussion we shall also compare the memory requirements of both MCTDH versions (VMF and CMF) and the standard method. Since for small systems the memory requirements usually do not pose a problem, we confine ourselves again to large systems (i.e. $n^f \gg fN^2$, when memory is concerned) where the only important contribution to the memory comes from the A-vectors.

In the VMF scheme the predictor-corrector routine we usually use is driven with a fixed order P. An overall number of $(P + 6)$ A-vectors must then be held in memory (including all auxiliary vectors), yielding $(P + 6)n^f$ complex numbers. Taking into account all A-vectors employed in the propagation, the step size control, the additional output of the auto-correlation function, as well as all auxiliary vectors, the CMF method requires the storage of $(L + 6)n^f$ complex numbers, where L is the maximum Lanczos order needed to integrate the intervals of length $\tau/2$. Typical values for the integration order are $P = 6$ and $L = 5$ to $L = 25$.

On the other hand, in the standard approach with a Chebyshev integrator [62] taken for the propagation, four wavefunctions, i.e. $4N^f$ complex numbers, must be stored in memory. So the memory gain of the MCTDH scheme with respect to the standard method, defined as the ratio between the memory requirements, ranges from about $1/8\ (N/n)^f$ to $1/3\ (N/n)^f$. Typically, n is about three to ten times smaller than N, leading to impressive memory gain factors if f is comparatively large.

For the above example system — assuming double precision arithmetics — the standard method would require the storage of 43 Gigabytes of data, which would by far exceed the memory of even the largest (single processor) machines available today. On the contrary, the MCTDH algorithm with, say, $L = 20$ needs merely 6 Megabytes, allowing to do the same calculation on a small workstation or even a personal computer!

5.2.7 Experiences with the CMF scheme

In order to illuminate the characteristics of the CMF integrator, let us summarise the experiences that have been made so far with the CMF scheme. These experiences are based on studies on the photo-dissociation of NOCl [106] and CH_3I [54], the reactive scattering of $H + H_2$ and $H + D_2$ [45,46], the photo-absorption of pyrazine [36,37], and the scattering of N_2 on an LiF surface [107]. A detailed investigation of the CMF method can be found in Ref. [54].

In these calculations the CMF error control was found to adjust the step size very reasonably. One aspect that has been examined is the accuracy of the CMF integrator in dependence of the chosen error tolerance ϵ. The finding was more or less the same for all the systems mentioned above: one typically obtains a good, excellent, and perfect agreement between the CMF and the VMF results for $\epsilon = 10^{-5}$, $\epsilon = 10^{-6}$, and $\epsilon = 10^{-7}$, respectively. This considerably simplifies the usage of the CMF integrator since it allows one to predict quite reliably the error tolerance necessary for a desired accuracy. The number of steps that had to be repeated because of a too large error was small in all these calculations.

In one study [54] the CMF error was monitored during the propagation and found to grow almost linearly with the propagation time. The CMF error was also compared with the MCTDH error, i.e. the error of the MCTDH scheme with respect to the standard method (see Sec. 2.2). The CMF error was slightly smaller than the MCTDH error when $\epsilon = 10^{-6}$ was used, and negligible for $\epsilon = 10^{-7}$. Furthermore, in all calculations with a Hermitian Hamiltonian the CMF method conserves the norm very strictly, because the SIL integrator explicitly constructs a normalised solution. Employing the VMF scheme, on the other hand, generally leads to a slight loss of norm due to numerical inaccuracies.

Another interesting property is of course the gain of the CMF over the VMF scheme. As explained in Sec. 5.2.6 one can expect a considerable reduction of the CPU time for systems for which the computation of the mean-fields is expensive, i.e. for systems with many degrees of freedom f (or particles p when modes are combined, see Sec. 4.5), many single-particle functions n, and a large number of Hamiltonian expansion terms s. In several studies this gain amounted to about a factor of ten, with virtually no loss of accuracy [54,45,46]. For the 24-mode pyrazine system [36,37] it is not manageable to perform a VMF run over the full propagation time, so the integration schemes were compared over only a short initial time segment; gain factors between 10 and 20 were then obtained. The CMF method was even for the rather small NOCl system ($f = 3$, $n = 5$, $s = 22$) about three times faster than the VMF scheme (see Sec. 9.1). The memory requirement of the CMF calculations, which mainly depends on the maximum Lanczos order, was nearly always comparable to that of the VMF method.

So far only one example — the scattering of N_2 on an LiF surface — has been found where the use of the CMF integrator led to only an insignificant reduction of the computation time, so that the VMF method was preferred [107]. In that study the spherical harmonics FBR was employed (cf. App. B.4.6) yielding non-diagonal potential matrices. This disables the summation of potential terms as discussed in Sec. 5.2.5, making the CMF scheme less efficient for this special case.

The studies that have been performed to date indicate that for sufficiently large systems the CMF integration scheme usually reduces the computational effort by one order of magnitude. Therefore, the CMF scheme has turned out to be the favoured integrator for large systems.

6 Product representation of potential energy surfaces

The knowledge of the electronic potential energy surface (PES) of the molecular system under consideration is a necessary prerequisite when investigating molecular dynamics. The PES may be given on a grid of, e.g. *ab initio*, points, or there may exist an analytical fit or a model potential which represents the PES. These representations are, by their nature, multi-dimensional and non-separable. The MCTDH algorithm, however, requires the potential to be represented as a linear combination of products of one-dimensional functions (except when employing the CDVR method, see Sec. 4.3).

In this section algorithms are discussed that allow the generation of such product representations. The product representation should converge fast, i.e. should require only a small number of expansion terms for representing the potential within some error bound. For more detailed discussions on product representation algorithms see Refs. [40,56,57].

6.1 Expansion in natural potentials

Given a real and continuous function of two variables the *Approximationstheorem* of Schmidt defines a constructive scheme to approximate this function as a sum of products of one-dimensional functions [108]. This approximation is proven to be optimal in the $\mathcal{L}^2$-sense. The approximation procedure requires the computation of the eigenvalues and eigenfunctions of an integral kernel of a homogeneous integral equation. Extending this ansatz to an arbitrary number of degrees of freedom is the basis of the product representation scheme which is outlined in the following.

First, the potential energy values $V_{i_1 \ldots i_f}$ are assumed to be given on a product grid,

$$V\left(Q_{i_1}^{(1)}, \ldots, Q_{i_f}^{(f)}\right) \equiv V_{i_1 \ldots i_f} \,, \tag{93}$$

where f denotes the number of degrees of freedom considered and $Q^{(\kappa)}$ the coordinate of the κth degree of freedom. Finally, $Q_{i_\kappa}^{(\kappa)}$ denotes the i_κth grid point of the κth one-dimensional grid with $1 \leq i_\kappa \leq N_\kappa$. The grids are precisely the grids used in the subsequent MCTDH calculation.

Next, symmetric positive semi-definite *potential density matrices* $\boldsymbol{\varrho}^{(\kappa)}$ are defined:

$$\varrho_{jl}^{(\kappa)} = \sum_{i_1=1}^{N_1} \cdots \sum_{i_{\kappa-1}=1}^{N_{\kappa-1}} \sum_{i_{\kappa+1}=1}^{N_{\kappa+1}} \cdots \sum_{i_f=1}^{N_f} V_{i_1 \ldots i_{\kappa-1} j i_{\kappa+1} \ldots i_f} V_{i_1 \ldots i_{\kappa-1} l i_{\kappa+1} \ldots i_f} \,. \tag{94}$$

The orthonormal eigenvectors $\boldsymbol{v}_j^{(\kappa)}$ (with components $v_{ij}^{(\kappa)}$) and the eigenvalues $\lambda_j^{(\kappa)}$ of the potential density matrix $\boldsymbol{\varrho}^{(\kappa)}$ are called *natural potentials* and *natural potential populations*, respectively. The natural populations are assumed to be in decreasing order, $\lambda_j^{(\kappa)} \geq \lambda_{j+1}^{(\kappa)}$, and it is convenient to introduce the notation $v_j^{(\kappa)}(Q_i^{(\kappa)}) := v_{ij}^{(\kappa)}$. This notation interprets the eigenvectors $v_j^{(\kappa)}$ as one-dimensional functions which, however, are defined on the set of grid points $\{Q_i^{(\kappa)}\}$ only. Choosing a set of expansion orders $\{m_\kappa\}$ one may now approximate the potential

$$\begin{aligned} V\left(Q_{i_1}^{(1)}, \ldots, Q_{i_f}^{(f)}\right) &\approx V^{\text{app}}\left(Q_{i_1}^{(1)}, \ldots, Q_{i_f}^{(f)}\right) \\ &= \sum_{j_1=1}^{m_1} \cdots \sum_{j_f=1}^{m_f} C_{j_1 \ldots j_f}\, v_{j_1}^{(1)}\left(Q_{i_1}^{(1)}\right) \ldots v_{j_f}^{(f)}\left(Q_{i_f}^{(f)}\right) . \end{aligned} \tag{95}$$

The expansion coefficients $C_{j_1 \ldots j_f}$ are determined by the overlaps between the potential and the natural potentials,

$$C_{j_1 \ldots j_f} = \sum_{i_1=1}^{N_1} \cdots \sum_{i_f=1}^{N_f} V_{i_1 \ldots i_f} v_{i_1 j_1}^{(1)} \ldots v_{i_f j_f}^{(f)} . \tag{96}$$

Since the orthonormal product basis set is complete over the grid points, we find that the approximated and the exact potential are identical at the grid points, if the expansion orders and the number of grid points are equal, i.e, $V^{\text{app}} \to V$ for $\{m_\kappa\} \to \{N_\kappa\}$. Note that the expansion coefficients are independent of the expansion orders.

The two-dimensional case is a special one. Here, the two potential density matrices have identical eigenvalues (except for possibly a different number of zero eigenvalues). The coefficient matrix is diagonal [27,29],

$$C_{ij} = \pm \delta_{ij} \sqrt{\lambda_i} , \tag{97}$$

and the expansion is optimal, i.e. the $\mathcal{L}^2$-error of the approximation is minimal (see *Approximationstheorem* by E. Schmidt [108]).

The $\mathcal{L}^2$-error Δ^2 is defined as the sum of the squares of the moduli of the fit errors on all product grid points,

$$\Delta^2 = \sum_{i_1=1}^{N_1} \cdots \sum_{i_f=1}^{N_f} \left(V_{i_1 \ldots i_f} - V_{i_1 \ldots i_f}^{\text{app}}\right)^2 . \tag{98}$$

For an arbitrary number of degrees of freedom it is shown in App. D that the $\mathcal{L}^2$-error Δ^2 can be expressed in terms of the expansion coefficients,

$$\Delta^2 = \sum_{j_1=m_1+1}^{N_1} \sum_{j_2=1}^{N_2} \cdots \sum_{j_f=1}^{N_f} \left|C_{j_1\dots j_f}\right|^2 + \sum_{j_1=1}^{m_1} \sum_{j_2=m_2+1}^{N_2} \sum_{j_3=1}^{N_3} \cdots \sum_{j_f=1}^{N_f} \left|C_{j_1\dots j_f}\right|^2$$
$$+ \dots + \sum_{j_1=1}^{m_1} \cdots \sum_{j_{f-1}=1}^{m_{f-1}} \sum_{j_f=m_f+1}^{N_f} \left|C_{j_1\dots j_f}\right|^2 . \qquad (99)$$

Since the natural populations represent an upper limit for the expansion coefficients (see App. D for more details),

$$\left|C_{j_1\dots j_f}\right|^2 \leq \min\left\{\lambda_{j_1}^{(1)}, \dots, \lambda_{j_f}^{(f)}\right\} , \qquad (100)$$

it is clear that one may safely truncate the expansion as soon as the natural populations become negligible.

It should be clear that both the methodology and the nomenclature is very similar to their MCTDH counterparts. The potential V replaces the wave function Ψ and the vector $C_{j_1\dots j_f}$ the MCTDH A-vector. The potential density matrices and the natural potentials have their counterparts in the (MCTDH) density matrices and natural orbitals; the expansion orders m_κ are similar in meaning to the numbers n_κ of single-particle functions.

6.2 Contraction over one mode

To decrease the number of expansion terms $s = \prod_{i=1}^{f} m_i$ in Eq. (95) by a factor of m_κ, one can define *contracted expansion functions*

$$D_{j_1\dots j_{\kappa-1} j_{\kappa+1}\dots j_f}\left(Q_{i_\kappa}^{(\kappa)}\right) = \sum_{j_\kappa=1}^{m_\kappa} C_{j_1\dots j_f} v_{i_\kappa j_\kappa}^{(\kappa)} \qquad (101)$$

and rewrite the expansion of the approximated potential as

$$V^{\mathrm{app}}\left(Q_{i_1}^{(1)}, \dots, Q_{i_f}^{(f)}\right) \qquad (102)$$
$$= \sum_{j_1=1}^{m_1} \cdots \sum_{j_{\kappa-1}=1}^{m_{\kappa-1}} \sum_{j_{\kappa+1}=1}^{m_{\kappa+1}} \cdots \sum_{j_f=1}^{m_f} v_{j_1}^{(1)}\left(Q_{i_1}^{(1)}\right) \dots v_{j_{\kappa-1}}^{(\kappa-1)}\left(Q_{i_{\kappa-1}}^{(\kappa-1)}\right)$$
$$\times D_{j_1\dots j_{\kappa-1} j_{\kappa+1}\dots j_f}\left(Q_{i_\kappa}^{(\kappa)}\right) v_{j_{\kappa+1}}^{(\kappa+1)}\left(Q_{i_{\kappa+1}}^{(\kappa+1)}\right) \dots v_{j_f}^{(f)}\left(Q_{i_f}^{(f)}\right) .$$

The summation in Eq. (101) can be performed over *all* natural potentials of the κth degree of freedom by replacing the upper summation limit m_κ with N_κ. This increases the accuracy of the potential approximation (95) without increasing the number of potential expansion coefficients. We will denote this procedure in the following as *contraction over the κth mode.* In Sec. 6.5 a measure is provided which helps in finding the optimal mode for the contraction.

In contrast to the two-dimensional case the expansion (95) is in general not optimal for more than two degrees of freedom, and there may exist another product basis for which the $\mathcal{L}^2$-error may be smaller for the same set of expansion orders $\{m_\kappa\}$. In order to arrive at these optimal potential functions one may iteratively improve the natural potentials by a multi-dimensional optimisation procedure.

Since the natural potentials form a complete set in which to represent the potential on the grid points, one can define the following *ansatz* for improved vectors $\tilde{\boldsymbol{v}}_j^{(\kappa)}$ of the κth degree of freedom,

$$\tilde{\boldsymbol{v}}_j^{(\kappa)} = \boldsymbol{v}_j^{(\kappa)} + \sum_{l=m_\kappa+1}^{N_\kappa} \mu_{jl}^{(\kappa)} \boldsymbol{v}_l^{(\kappa)}, \qquad j = 1, 2, \ldots, m_\kappa, \tag{103}$$

where $\boldsymbol{v}_j^{(\kappa)}$ denotes the natural potentials obtained by diagonalisation of the density matrix $\boldsymbol{\varrho}^{(\kappa)}$ (see Eq. (94)) and where m_κ and N_κ are the expansion order and the number of grid points for the κth degree of freedom, respectively.

The parameters $\mu_{jl}^{(\kappa)}$ may be understood as the unknown model parameters of a merit function χ^2,

$$\chi^2(\boldsymbol{\mu}) = \sum_{i_1=1}^{N_1} \cdots \sum_{i_f=1}^{N_f} \left(V_{i_1\ldots i_f} - \tilde{V}^{\text{app}}_{i_1\ldots i_f} \right)^2, \tag{104}$$

which is to be minimised with respect to $\boldsymbol{\mu}$, where $\boldsymbol{\mu}$ denotes the set $\left\{\boldsymbol{\mu}^{(\kappa)}\right\}$ of μ-matrices for each degree of freedom. The new representation of the potential in the basis of the new fit vectors is then given by

$$\tilde{V}^{\text{app}}_{i_1\ldots i_f} = \sum_{j_1=1}^{m_1} \cdots \sum_{j_f=1}^{m_f} \tilde{C}_{j_1\ldots j_f} \tilde{v}^{(1)}_{i_1 j_1} \cdots \tilde{v}^{(f)}_{i_f j_f}, \tag{105}$$

with the expansion coefficients $\tilde{C}_{j_1\ldots j_f}$ defined as in Eq. (96) by the overlaps of the improved (and re-orthonormalised) vectors $\tilde{\boldsymbol{v}}_j^{(\kappa)}$ with the potential V.

This nonlinear optimisation problem may be written as a set of linear equations for the parameters $\boldsymbol{\mu}^{(\kappa)}$ involving the calculation of the gradient and of the Hessian matrix of χ^2 with respect to $\boldsymbol{\mu}^{(\kappa)}$. The solution of this set of linear equations defines improved vectors according to Eq. (103) which can be iteratively optimised repeating the same procedure until the $\mu_{jl}^{(\kappa)}$ coefficients become sufficiently small (for further details see Ref. [102]).

We prefer a different approach to iteratively improve the natural potentials, and thereby to minimise the $\mathcal{L}^2$-error of the approximated potential energy surface as given by Eq. (99). The iteration scheme described in the following can be shown to be equivalent to the above-mentioned procedure, but we believe it is more stable and easier to implement.

Before the iteration scheme is outlined, *modified potential density matrices* $\tilde{\boldsymbol{\varrho}}^{(\kappa)}$ are introduced:

$$\tilde{\varrho}_{jl}^{(\kappa)} = \sum_{j_1=1}^{m_1} \cdots \sum_{j_{\kappa-1}=1}^{m_{\kappa-1}} \sum_{j_{\kappa+1}=1}^{m_{\kappa+1}} \cdots \sum_{j_f=1}^{m_f} C_{j_1 \cdots j_{\kappa-1} j j_{\kappa+1} \cdots j_f} C_{j_1 \cdots j_{\kappa-1} l j_{\kappa+1} \cdots j_f} \, . \tag{106}$$

The indices j and l run from 1 to N_κ such that the short potential coefficient vector $C_{j_1 \cdots j_f}$ of Eq. (95), where $1 \leq j_\kappa \leq m_\kappa$, is replaced by a long coefficient vector without index restriction. Note that in contrast to Eq. (94) the upper summation limits are the potential expansion orders m_κ and not the number of grid points N_κ. If the potential expansion orders m_κ equal the number of grid points N_κ in each degree of freedom, then the modified potential density matrix $\tilde{\boldsymbol{\varrho}}^{(\kappa)}$ becomes identical to the diagonalised form of the original potential density matrix $\boldsymbol{\varrho}^{(\kappa)}$, i.e. $\tilde{\varrho}_{ij}^{(\kappa)} \rightarrow \delta_{ij} \lambda_j^{(\kappa)}$ for $\{m_\kappa\} \rightarrow \{N_\kappa\}$. By diagonalising the modified potential density matrix $\tilde{\boldsymbol{\varrho}}^{(\kappa)}$ one arrives at an $\mathcal{L}^2$-optimal separation between the κth degree of freedom and the rest as currently approximated. Running through all the degrees of freedom one will eventually converge to a global $\mathcal{L}^2$-optimal product representation.

The individual steps of the iteration scheme can now be summarised:

(1) Start of iteration: For each degree of freedom the potential density matrices $\boldsymbol{\varrho}^{(\kappa)}$ are diagonalised, and *all* natural potentials $\boldsymbol{v}_{j_\kappa}^{(\kappa)}$ $(1 \leq j_\kappa \leq N_\kappa)$ are computed.

(2) For each degree of freedom the natural potentials are copied according to $\boldsymbol{v}_{j_\kappa}^{\mathrm{old},(\kappa)} := \boldsymbol{v}_{j_\kappa}^{(\kappa)}$.
All following steps are performed successively for each degree of freedom κ.

(3) The long vector of coefficients $C_{j_1 \cdots j_f}$, with $1 \leq j_\kappa \leq N_\kappa$, is computed as the overlap of the old potential vectors with the potential V (see Eq. (96))

$$C_{j_1 \cdots j_f} = \sum_{i_1=1}^{N_1} \cdots \sum_{i_f=1}^{N_f} V_{i_1 \cdots i_f} v_{i_1 j_1}^{\mathrm{old},(1)} \cdots v_{i_f j_f}^{\mathrm{old},(f)} \, . \tag{107}$$

(4) The modified potential density matrices $\tilde{\boldsymbol{\varrho}}^{(\kappa)}$ are computed according to Eq. (106) and diagonalised:

$$\tilde{\boldsymbol{\varrho}}_{\mathrm{diag}}^{(\kappa)} = \boldsymbol{U}^{(\kappa)\mathrm{T}} \tilde{\boldsymbol{\varrho}}^{(\kappa)} \boldsymbol{U}^{(\kappa)} \, . \tag{108}$$

$\boldsymbol{U}^{(\kappa)}$ denotes the orthogonal matrix of eigenvectors of the κth degree of freedom.

(5) Let $\boldsymbol{\mathcal{V}}^{\mathrm{new},(\kappa)} = \left(\boldsymbol{v}_1^{\mathrm{new},(\kappa)} \dots \boldsymbol{v}_{N_\kappa}^{\mathrm{new},(\kappa)}\right)$ and $\boldsymbol{\mathcal{V}}^{\mathrm{old},(\kappa)} = \left(\boldsymbol{v}_1^{\mathrm{old},(\kappa)} \dots \boldsymbol{v}_{N_\kappa}^{\mathrm{old},(\kappa)}\right)$ denote the matrices with the (improved) new $\boldsymbol{v}_{j_\kappa}^{\mathrm{new},(\kappa)}$ and the old $\boldsymbol{v}_{j_\kappa}^{\mathrm{old},(\kappa)}$ potential vectors as columns, respectively. The improved vectors are then given by an orthonormal transformation of the old ones,

$$\boldsymbol{\mathcal{V}}^{\mathrm{new},(\kappa)} = \boldsymbol{\mathcal{V}}^{\mathrm{old},(\kappa)} \boldsymbol{U}^{(\kappa)} \,. \tag{109}$$

(6) New expansion coefficients $C^{\mathrm{new}}_{j_1 \dots j_f}$ are determined as the overlap of the improved natural potentials $\boldsymbol{v}_j^{\mathrm{new},(\kappa)}$ with the potential V (see Eq. (96)).

(7) The new potential vectors of the κth degree of freedom are copied according to $\boldsymbol{v}_{j_\kappa}^{\mathrm{old},(\kappa)} := \boldsymbol{v}_{j_\kappa}^{\mathrm{new},(\kappa)}$.

(8) The steps (3) to (7) are repeated until convergence is reached, i.e. until the orthogonal eigenvector matrices $\boldsymbol{U}^{(\kappa)}$ are sufficiently close to unit matrices.

The procedure defined by the steps (1) to (8) is called *separable iteration* in the following. The naming should become clear when the *relevant-region* iteration scheme is introduced in Sec. 6.6. We have found that — at least for the examples we have treated — the separable iteration procedure lowered the $\mathcal{L}^2$-error only marginally. The direct expansion in natural orbitals, Eqs. (94) to (96), thus fortunately yields an expansion that is very close to an $\mathcal{L}^2$-optimal one and a further refinement does not seem to be necessary. The separable iteration procedure has been discussed here in detail because it will become important when non-separable weights are introduced (see Sec. 6.6).

6.4 Separable weights

In general, not all regions of the potential energy surface are equally relevant for the process under investigation. The introduction of an appropriately chosen weight function w then allows the enhancement of regions of the surface with greater physical relevance. Instead of minimising the global $\mathcal{L}^2$-error Δ (see Eq. (98)) one then tries to minimise the *weighted $\mathcal{L}^2$-error*: Δ^{w}

$$\begin{aligned}(\Delta^{\mathrm{w}})^2 = \sum_{i_1=1}^{N_1} \cdots \sum_{i_f=1}^{N_f} &\left[V\left(Q_{i_1}^{(1)}, \dots, Q_{i_f}^{(f)}\right) - V^{\mathrm{app}}\left(Q_{i_1}^{(1)}, \dots, Q_{i_f}^{(f)}\right)\right]^2 \\ &\times w^2\left(Q_{i_1}^{(1)}, \dots, Q_{i_f}^{(f)}\right) \,. \end{aligned} \tag{110}$$

The fit procedure allows an easy inclusion of a global weight function as long as it is given as a product of one-dimensional *separable weight functions*, i.e.

$$w\left(Q^{(1)}, \dots, Q^{(f)}\right) = w^{(1)}\left(Q^{(1)}\right) \dots w^{(f)}\left(Q^{(f)}\right) \,. \tag{111}$$

The variational problem (110) is then equivalent to a global $\mathcal{L}^2$-error minimisation of the weighted potential energy surface

$$V^{\mathrm{w}}_{i_1 \dots i_f} = V\left(Q^{(1)}_{i_1}, \dots, Q^{(f)}_{i_f}\right) \cdot w^{(1)}\left(Q^{(1)}_{i_1}\right) \dots w^{(f)}\left(Q^{(f)}_{i_f}\right) , \tag{112}$$

which can be expanded in a natural potential basis as defined by Eq. (95). The approximated potential surface then reads as

$$V^{\mathrm{app}}_{i_1 \dots i_f} = \sum_{j_1=1}^{m_1} \dots \sum_{j_f=1}^{m_f} C^{\mathrm{w}}_{j_1 \dots j_f} \left(v^{\mathrm{w},(1)}_{i_1 j_1} / w^{(1)}_{i_1}\right) \dots \left(v^{\mathrm{w},(f)}_{i_f j_f} / w^{(f)}_{i_f}\right) , \tag{113}$$

where $\boldsymbol{v}^{\mathrm{w},(\kappa)}$ and $C^{\mathrm{w}}_{j_1 \dots j_f}$ denote the natural potentials and expansion coefficients derived from the weighted potential energy surface V^{w}, Eq. (112), and where $w^{(\kappa)}_j = w^{(\kappa)}(Q^{(\kappa)}_j)$.

Separable weights have been successfully applied in the product representation of the S_1-surface of NOCl. There an appropriate choice of the separable weights led to a reduction of the number of necessary expansion terms by a factor of about five [56].

6.5 Error measures

So far we have defined the quality of a potential fit by its (global) $\mathcal{L}^2$-error. After weights have been introduced more refined error measures are necessary.

By $\Delta^{\mathrm{w}}_{\mathrm{rms}}$ we denote a *weighted root-mean-square* (rms) *error* which is defined as

$$\Delta^{\mathrm{w}}_{\mathrm{rms}} = \sqrt{S^{-1} \sum_{i_1=1}^{N_1} \dots \sum_{i_f=1}^{N_f} \left(V_{i_1 \dots i_f} - V^{\mathrm{app}}_{i_1 \dots i_f}\right)^2 w^{(1)^2}_{i_1} \dots w^{(f)^2}_{i_f}} , \tag{114}$$

where

$$S = \sum_{i_1=1}^{N_1} \dots \sum_{i_f=1}^{N_f} w^{(1)^2}_{i_1} \dots w^{(f)^2}_{i_f} . \tag{115}$$

Introducing *reduced natural populations*,

$$\lambda^{\mathrm{red}} = \lambda / S , \tag{116}$$

both the reduced natural populations λ^{red} and the weighted rms-error $\Delta_{\mathrm{rms}}^{\mathrm{w}}$ are invariant with respect to a multiplication of the weight functions by a constant scale factor.

If all weights equal 1, i.e. $w_i^{(\kappa)} \equiv 1$, S equals the number of grid points $N_{\mathrm{tot}} = \prod_{\kappa=1}^{f} N_\kappa$ and $\Delta_{\mathrm{rms}}^{\mathrm{w}}$ reduces to the (common) *global rms-error*

$$\Delta_{\mathrm{rms}} = \sqrt{N_{\mathrm{tot}}^{-1} \sum_{i_1=1}^{N_1} \cdots \sum_{i_f=1}^{N_f} \left(V_{i_1 \ldots i_f} - V_{i_1 \ldots i_f}^{\mathrm{app}} \right)^2} \,. \tag{117}$$

The reduced natural populations and the weighted rms-error are closely related. If one removes from a complete expansion (i.e. $m_\kappa = N_\kappa$) in one degree of freedom exactly those m natural potentials which correspond to the m lowest natural potential populations, one can immediately specify the resulting weighted rms-error [56]:

$$\Delta_{\mathrm{rms}}^{\mathrm{w}} = \sqrt{\sum_{j=N_\kappa-m}^{N_\kappa} \lambda_j^{\mathrm{red},(\kappa)}} \,. \tag{118}$$

Equation (118) may be generalised by summing over all those reduced natural populations corresponding to those natural potentials which have been removed from the expansion (95). This quantity still provides a good estimate for the resulting rms-error,

$$\Delta_{\mathrm{rms}}^{\mathrm{w}} \approx \sqrt{\sum_{\kappa=1}^{f} \sum_{j_\kappa=m_\kappa+1}^{N_\kappa} \lambda_{j_\kappa}^{\mathrm{red},(\kappa)}} \,. \tag{119}$$

This estimate is very helpful when choosing the potential orders, m_κ.

For two dimensions the approximation error can be expressed exactly, since the coefficient matrix of the product expansion in this case is diagonal (see Eq. (97)). Employing Eq. (118) one obtains in this case

$$\Delta_{\mathrm{rms}}^{\mathrm{w}} = \sqrt{\sum_{j=s+1}^{\min(N_1,N_2)} \lambda_j^{\mathrm{red}}} \,, \tag{120}$$

where $s = m_1 = m_2$ denotes the expansion order and N_1 and N_2 the number of grid points of the first and second degree of freedom, respectively.

Since the approximation error for given expansion order s in general is not independent of the degree of freedom over which the contraction (see Eq.

(102)) is performed it is important to choose the optimal degree of freedom for contraction. The reduced natural potential populations, as defined in Eq. (116), provide good criteria for choosing the optimal degree of freedom for contraction. Following the lines which led to the estimation Eq. (119) the optimal degree of freedom for contraction is that for which the measure

$$\left(\Delta^{(\kappa)}\right)^2 = \sum_{\substack{\kappa'=1 \\ \kappa'\neq\kappa}}^{f} \sum_{j=m_{\kappa'}+1}^{N_{\kappa'}} \lambda_j^{\mathrm{red},(\kappa')} \tag{121}$$

is minimal.

6.6 *Emulating non-separable weights*

More efficient than separable weights are of course general non-separable weights. The direct application of non-separable weights (see, e.g., chapter 15.5 of Ref. [102]), however, results in (often unsolvable) large coupled systems of linear equations. To circumvent this problem we emulate non-separable weights by modifying the potential to be approximated. To this end an f-dimensional function ω is introduced which assigns every potential value on the product grid a weight between 0 and 1,

$$0 \le \omega_{i_1\ldots i_f} \equiv \omega\left(Q_{i_1}^{(1)}, \ldots, Q_{i_f}^{(f)}\right) \le 1\,. \tag{122}$$

All *physically relevant* points are given the weight 1 and all physically less or even irrelevant points are given smaller weights or even the weight 0.

Having defined ω, the separable iteration procedure of Sec. 6.3 can be modified and extended in such a way that f-dimensional *non-separable weight functions* can be simulated. The concept and the individual steps of this *relevant region iteration* are described in the following.

To begin with, the exact potential V is expanded in the standard manner in a product basis of natural potentials according to Eq. (95), yielding V^{app}. Then a *modified reference potential* $\tilde{V}$ is defined as a linear combination of the exact potential V and of the potential fit V^{app},

$$\tilde{V}_{i_1\ldots i_f} = \omega_{i_1\ldots i_f} V_{i_1\ldots i_f} + (1-\omega_{i_1\ldots i_f}) V^{\mathrm{app}}_{i_1\ldots i_f}\,. \tag{123}$$

The modified reference potential $\tilde{V}$ equals the exact potential at points where $\omega = 1$, and becomes the fit-potential V^{app} when $\omega = 0$. In the following the modified reference potential $\tilde{V}$ serves as the new reference potential which is to be approximated. To this end a single iteration step, as described in detail in Sec. 6.3 is performed. As a result of this iteration step, improved one-dimensional potential vectors and corresponding potential expansion coefficients are determined. Improved means that the $\mathcal{L}^2$-error over the relevant region is reduced.

The individual steps of the relevant region iteration procedure can be repeated until some break-off criterion is satisfied. After each step the representation of the exact potential energy surface in the relevant region is improved.

Schematically the relevant region iteration procedure can be summarised as follows:

(0) Initialisation:
- The relevant regions and therewith the f-dimensional function ω are defined.
- The exact potential V is expanded in a product basis of natural potentials according to Eq. (95), yielding V^{app}.
- The counter is set to $k = 0$, and $\tilde{V}^{(0),\text{app}}_{i_1 \dots i_f} = V^{\text{app}}_{i_1 \dots i_f}$.

(1) The modified reference potential is defined:

$$\tilde{V}^{(k+1)}_{i_1 \dots i_f} = \omega_{i_1 \dots i_f} V_{i_1 \dots i_f} + (1 - \omega_{i_1 \dots i_f}) \tilde{V}^{(k),\text{app}}_{i_1 \dots i_f} \,. \tag{124}$$

(2) One separable iteration step as defined in Sec. 6.3 is performed. The only modification is that the exact potential V is replaced by the modified reference potential $\tilde{V}^{(k+1)}$. $\tilde{V}^{(k+1),\text{app}}$ then denotes the product representation of $\tilde{V}^{(k+1)}$.

(3) The step counter is increased by one: $k \leftarrow k + 1$.

(4) The steps (1) to (3) are repeated until some break-off criterion is satisfied.

The interpretation of the f-dimensional function ω (see Eq. (122)) can be substantially extended assuming that the relevant region iteration converges. In fact, in all examples investigated so far the relevant region iteration converged (as long as $\omega > 0$) even though the convergence property has not yet been proven in a strict mathematical sense. In the limit of convergence both the modified reference potential and the approximated potential by definition stay constant, i.e. $\lim_{k\to\infty} \tilde{V}^{(k+1)} = \tilde{V}$ and $\lim_{k\to\infty} \tilde{V}^{(k),\text{app}} = \tilde{V}^{\text{app}}$ hold.

For these converged quantities it follows immediately from Eq. (124) that

$$\tilde{V}_{i_1 \dots i_f} - \tilde{V}^{\text{app}}_{i_1 \dots i_f} = \omega_{i_1 \dots i_f} \left(V_{i_1 \dots i_f} - \tilde{V}^{\text{app}}_{i_1 \dots i_f} \right) \,. \tag{125}$$

Since the iteration procedure minimises the difference (in $\mathcal{L}^2$-sense) between the approximated potential $\tilde{V}^{\text{app}}$ and the modified reference potential $\tilde{V}$, it minimises the weighted difference appearing on the right hand side of Eq. (125). Thus, it minimises the weighted $\mathcal{L}^2$-error Δ^{w} defined by Eq. (110) for a general multi-dimensional weight function with ω replacing w.

Since we may now consider ω as a general weight function, the use of separable weights seems to be redundant. However, we prefer to keep the separable weights. Their use allows ω to be defined by a simple, vivid, and convenient procedure, namely by defining relevant regions where $\omega = 1$. Since the reference potential is not changed over the relevant region, the iteration procedure converges faster than in cases where ω takes on a complicated form. Additionally, the use of separable weights, with the aid of Eq. (119), provides a convenient tool for determining the optimal expansion orders m_κ.

To monitor the performance of the relevant-region iteration procedure additional error measures are introduced. The *relevant rms-error* $\Delta^{\mathrm{r}}_{\mathrm{rms}}$ and the *relevant and weighted rms-error* $\Delta^{\mathrm{rw}}_{\mathrm{rms}}$ are defined similarly to Eqs. (117) and (114) but the summations now run only over the relevant grid points, i.e. those points for which $\omega_{i_1 \ldots i_f} = 1$ holds.

6.7 Concluding remarks

The product representation scheme of potential energy surfaces outlined in the preceding sections has been mainly developed in order to represent (analytically) given potential energy surfaces in an MCTDH adapted product form. It should be noted though that the procedure itself is general, and is by no means restricted to being employed in connection with MCTDH.

In cases where the potential energy surface is not given analytically, but the potential values are provided on a product grid (i.e. as a set of *ab initio* points) the product representation scheme can also be used to interpolate multi-dimensional potential energy surfaces (see Ref. [56] for more details).

Another point worth mentioning is that exploiting the underlying symmetry of the potential under consideration can substantially reduce the computational effort in terms of CPU time and memory. This has been shown in Ref. [56] in the example of a Coulomb potential.

6.8 Applications

In order to illustrate the product representation scheme of potential energy surfaces, we will give some example calculations. The first one treats the S_1-potential energy surface used for the photo-dissociation process of NOCl [56]. The product representation scheme has also been extensively employed to describe two- and three-dimensional reactive scattering of $H+H_2$ and its isotopic variants in binding [40,109], Jacobian [45,46,57,109], and hyperspherical [41,42] coordinates. We will review some of these studies.

6.8.1 The S_1-surface of NOCl

The product representation of the three-dimensional S_1-potential energy surface of NOCl served as one of the first realistic examples [56]. The potential energy surface of Schinke *et al.* [110] was used which is given as a cubic-spline fit to more than 600 *ab initio* points.

To check the quality of different product representations, MCTDH photo-dissociation calculations were performed and photo-absorption spectra were determined [56]. Without using weights, about 100 expansion coefficients were necessary in order to accurately reproduce the spectra obtained by propagation on the Schinke surface [56]. Here, the contraction (see Sec. 6.2) was performed over the angular degree of freedom.

Employing separable weights as defined in Sec. 6.4 the number of expansion coefficients could be reduced. Only 20 expansion coefficients were then found to be necessary. Note that this reduction of the number of expansion coefficients by a factor of five speeds up the MCTDH calculation by almost the same factor.

The choice of the separable weights was straightforward and intuitive. For explicit parameters and functional forms of the separable weight functions the reader is referred to Ref. [56]. The parameters presented in that reference just serve as an example, and can be varied without causing drastic changes. The weight function for the dissociative degree of freedom reduces the importance of the high energy repulsive part of the surface corresponding to small distances of the dissociative coordinate. The two other weight functions further pronounce those regions of the potential energy surface which the wavepacket visits during the photo-dissociation process.

6.8.2 The collinear LSTH-surface

The product representation of the collinear Liu-Siegbahn-Truhlar-Horowitz (LSTH) surface [111–113] was studied in both Jacobian and binding coordinates. This example demonstrates that the choice of the coordinate system may strongly influence the rate of convergence of the product representation.

A second point studied here is the relevant region iteration procedure described in Sec. 6.6. By separating the coordinate space into regions of minor and major physical relevance the surface is no longer globally optimised, but specifically optimised in the regions of major physical relevance.

The definition of the relevant regions is not only dependent on the surface but also on the process to be described. The energy distribution of the initial wavepacket defines those regions of the potential energy surface which are energetically accessible for the propagated wavepacket. Thus, for all potential

	binding coordinates		Jacobian coordinates			
Error-	$s = 10$		$s = 20$		$s = 10$	
measures	sep. weight	rel. reg.	sep. weight	rel. reg.	sep. weight	rel. reg.
$\Delta^{\mathrm{rw}}_{\mathrm{rms}}$	0.13	0.04	0.05	0.01	15.4	3.65
$\Delta^{\mathrm{r}}_{\mathrm{rms}}$	0.44	0.14	0.18	0.04	53.1	12.7
Δ_{rms}	1.08	2.91	0.26	0.34	83.0	111
$\Delta^{\mathrm{r}}_{\mathrm{max}}$	1.90	0.70	1.37	0.35	428	97.8
Δ_{max}	4.54	13.8	1.95	2.62	857	1083

Table 1
Errors in meV of three product representations of the collinear LSTH-surface. The error measures are defined by Eqs. (114) to (117). Δ_{max} denotes the maximum energy difference over all grid points. The upper index r indicates that the error Δ is evaluated over the relevant region only. The number of potential terms included is denoted by s and the labels "sep. weight" and "rel. reg." denote that separable weights only and separable weights plus relevant region iteration have been employed, respectively.

regions with energies greater than some energy E_{rel}, the function ω (Eq. (122)) takes small or even zero values. Additionally, in regions covered by complex absorbing potentials (CAPs), the wavepacket is absorbed artificially and the potential there does not need to be represented as accurately as in the interaction region. The thus defined relevant region [81] covers about 30% of all grid points.

The relevant region iteration procedure impressively improves the representation of the surface in the relevant region. Some numbers may highlight the improvements obtained after about 20 to 50 iteration steps. For both coordinate systems all relevant error measures ($\Delta^{\mathrm{rw}}_{\mathrm{rms}}$, $\Delta^{\mathrm{r}}_{\mathrm{rms}}$, $\Delta^{\mathrm{r}}_{\mathrm{max}}$) are reduced by about a factor of 3 to 5. At the same time the representation in the regions of minor relevance remained acceptable (see Tab. 1).

We now discuss the impact of the chosen coordinate system on the convergence of the product representation. This impact is indeed considerable. For the same expansion order the error for the representation in Jacobian coordinates is about two orders of magnitude larger. For 10 expansion coefficients, for example, the relevant and weighted rms-errors of the representation in binding and in Jacobian coordinates accounts to $\Delta^{\mathrm{rw}}_{\mathrm{rms}} = 0.04$ meV and $\Delta^{\mathrm{rw}}_{\mathrm{rms}} = 3.65$ meV, respectively. The latter number drops to 0.01 meV when 20 expansion coefficients are employed. A representation in Jacobian coordinates hence requires about twice as many expansion coefficients as a representation in binding coordinates. Finally, Tab. 1 compiles the values of the different error measures for the various cases. Reference [81] provides a more detailed discussion on the product representation of the collinear LSTH surface.

6.8.3 The 3D LSTH surface

The influence of product expansions of differing accuracy on the quality of three-dimensional H+H_2 reactive scattering calculations for total angular momentum $J = 0$ has been investigated in detail in Ref. [57]. There reaction probabilities obtained from MCTDH wavepacket propagation calculations on different surfaces are compared with numerically exact results of Zhang *et al.* [114].

The definition of the relevant regions followed the lines given in the preceding section. On satisfying the constraints defined in Ref. [57], again about 30% of all grid points are located in the relevant potential region. Separable weights which pronounce the reaction channels and collinear configurations were employed. The contraction was performed over the dissociative degree of freedom after analysing the measure $\Delta^{(\kappa)}$ (see Eq. (121)).

For an expansion with 240 terms the relevant and weighted rms-error, $\Delta^{\mathrm{rw}}_{\mathrm{rms}}$, is reduced from 5.3 to 1.0 meV after 30 iteration steps. A very accurate representation is thus generated. Only 60 expansion terms were found to be required to obtain converged H+$H_2(\nu = j = J = 0)$ reaction probabilities for total energies up to 2 eV. Only 108 expansion coefficients were needed for H+D_2 coupled states calculations of initial state-selected reaction cross-sections [46]. Some of these coupled states results are presented in Sec. 9.2.

The numerical effort required for determining the product representation is comparatively small. It took about two minutes on an AIX RS/6000 power2 workstation to compute the 240-terms potential approximation. This timing includes all iteration steps and the (comparatively time consuming) calculation of the different error measures after each iteration.

7 Preparation of the initial wavepacket

As outlined in the introduction, solving the time-dependent Schrödinger equation by a wavepacket propagation method requires the generation of an initial state. The definition of the initial state depends on the physical process under consideration, whereas its representation must fit the form of the MCTDH wavefunction (19). In some cases the initial wavefunction has a simple product form, e.g. a Hartree product, and can therefore be used directly. In other cases it is necessary to generate a complicated initial wavefunction. In the following sections two methods are described which generate commonly needed, complicated initial wavefunctions.

7.1 Generation of eigenstates by energy relaxation

In many processes the initial state is the eigenfunction of a potential energy surface. For example, in applications which involve a transition from the electronic ground to an excited state, the initial function is the ground-state eigenfunction of the system placed on an excited electronic state energy surface. Such an eigenfunction can be generated by applying the method of energy relaxation to a guess function [115]. In this method the wavefunction is propagated in imaginary time $t = -i\tau$. In Eq. (1) the exponential $\exp(-iE_j t)$ is thus replaced by $\exp(-E_j \tau)$, and the high energy contributions of the wavefunction are damped out. Performing this relaxation using the MCTDH method automatically generates the eigenfunction in the desired form. Energy relaxation was hence the method of choice in the MCTDH studies on the photo-dissociation of NOCl [28], NO_2 [31], and CH_3I [32,33,54].

Conventionally, during relaxation the wavefunction must be regularly renormalised to compensate for the loss of norm. When a relaxation calculation is performed within the MCTDH framework, the constraint $g^{(\kappa)} = 0$ is used and it is sufficient to renormalise the MCTDH coefficients A_J only. This is because the single-particle functions remain orthonormalised even for imaginary times due to the position of the projection operator in Eq. (41). For the A-vector one has to employ the equation of motion (68) and imaginary times or, equivalently, to use the equation $\dot{\boldsymbol{A}} = -\boldsymbol{\mathcal{K}}\boldsymbol{A}$ and real times. However, we found it convenient to slightly modify this working equation and use the non-linear equation

$$\dot{\boldsymbol{A}} = -\left(\boldsymbol{\mathcal{K}} - E\mathbf{1}\right)\boldsymbol{A} \qquad \text{with} \qquad E = \frac{\langle \boldsymbol{A} \mid \boldsymbol{\mathcal{K}} \mid \boldsymbol{A} \rangle}{\langle \boldsymbol{A} \mid \boldsymbol{A} \rangle} \tag{126}$$

instead. The wavefunction then still converges to the lowest eigenfunction of the Hamiltonian, but automatically stays normalised.

The main advantage of performing a relaxation calculation in this manner is a technical one: renormalisation is somewhat tricky when using a multistep integration routine, as is typically used in the VMF integration scheme (Sec. 5.1), because the wavefunctions at previous times have to be modified accordingly.

Note that since Eq. (126) is non-linear it cannot be solved with the SIL scheme, which is the preferable integrator in the CMF approach (Sec. 5.2). When the Lanczos scheme is employed in the relaxation of the MCTDH coefficients we therefore compute E only before each SIL step and renormalise $\boldsymbol{A}$ afterwards.

7.2 Initial wavepacket correction schemes for scattering problems

In scattering calculations the initial wavepacket can often be written as a Hartree product undergoing free motion in the reactant asymptotic region of the potential energy surface. This region is however often far away from the scattering centre, and long propagation times are then required. Here, correction schemes are detailed which enable the initial wavepacket to be moved closer to the centre, while retaining the product form required by the MCTDH method. The schemes have been used in a study on the H+H$_2$ (D$_2$) reactive scattering system [45,46]. Although having been developed for MCTDH, these corrections can be useful for other propagation schemes as well.

7.2.1 Preliminaries

Before the correction schemes are detailed, some definitions and concepts are briefly reviewed. A coordinate system is assumed where R denotes the distance between the two scattering fragments and $\boldsymbol{x}$ collectively denotes all the other coordinates. The Hamiltonian of the scattering system is then written as

$$H = H_0 + V_{\mathrm{I}}\,, \tag{127}$$

where $V_{\mathrm{I}} = V_{\mathrm{I}}(R, \boldsymbol{x})$ denotes the interaction potential which may contain a centrifugal term. It vanishes for large values of R,

$$\lim_{R\to\infty} V_{\mathrm{I}}(R,\boldsymbol{x}) = 0\,. \tag{128}$$

The free Hamiltonian

$$H_0 = T_R + H_{\mathrm{int}} \tag{129}$$

is the sum of the kinetic energy of the relative motion of the fragments, $T_R = -(2\mu_R)^{-1}\partial^2/\partial R^2$, and the internal Hamiltonian H_{int} that operates on the internal coordinates $\boldsymbol{x}$ only. The spectrum of the internal Hamiltonian is assumed to be discrete,

$$H_{\text{int}}\, \xi_\nu(\boldsymbol{x}) = E_\nu\, \xi_\nu(\boldsymbol{x})\,. \tag{130}$$

The index ν collectively accounts for all internal (e.g. ro-vibrational) quantum numbers.

Next, energy normalised free scattering wavefunctions are introduced. These are eigenfunctions of H_0, and are defined as a product of an incoming or outgoing wave, and an $\boldsymbol{\mathcal{L}}^2$-normalised eigenfunction of H_{int},

$$\Phi^{\pm}_{E\nu}(R, \boldsymbol{x}) = \chi^{\pm}_{E\nu}(R)\, \xi_\nu(\boldsymbol{x})\,, \tag{131}$$

where

$$\chi^{\pm}_{E\nu}(R) = \sqrt{\frac{\mu_R}{2\pi p_\nu}} e^{\pm i p_\nu R}\,, \tag{132}$$

and $p_\nu = \sqrt{2\mu_R(E - E_\nu)}$.

Finally, $\Psi^{+}_{E\nu}$ denotes the exact, time-independent, and energy normalised scattering wavefunction,

$$H\, \Psi^{+}_{E\nu} \;=\; E\, \Psi^{+}_{E\nu}\,, \tag{133}$$

satisfying the outgoing boundary condition

$$\Psi^{+}_{E\nu}(R, \boldsymbol{x}) \overset{R\to\infty}{\longrightarrow} \Phi^{-}_{E\nu}(R, \boldsymbol{x}) \;- \sum_{\nu'} S_{\nu',\nu}(E)\, \Phi^{+}_{E\nu'}(R, \boldsymbol{x}) \tag{134}$$

with scattering matrix elements $S_{\nu',\nu}$. The scattering matrix elements are thus defined by the asymptotic behaviour of the time-independent scattering wavefunction.

Since the time-dependent Schrödinger equation is to be solved, a connection between the time-independent scattering wavefunction $\Psi^{+}_{E\nu}$ and a time-dependent wavepacket must be created. Formally, a stationary scattering eigenfunction can be obtained by an energy-time Fourier transform of an appropriately chosen initial wave packet Ψ_0 which has been propagated by the system's Hamiltonian H,

$$|\,\Psi^{+}_{E\nu}\rangle = \frac{1}{2\pi\Delta(E)} \int_{-\infty}^{\infty} e^{-i(H-E)t}\, |\,\Psi_0\rangle\, dt\,. \tag{135}$$

The coefficient $\Delta(E)$ describes the energy distribution of the initial wavepacket Ψ_0.

The conditions that must be fulfilled by an appropriately chosen initial wavepacket are now to be specified in some more detail. The initial wavepacket Ψ_0 is assumed to be $\mathcal{L}^2$-normalised. It is defined as the product of a wavepacket in the translational coordinate, $\chi_0(R)$, and an eigenstate of the internal Hamiltonian,

$$\Psi_0(R, \boldsymbol{x}) = \chi_0(R)\, \xi_\nu(\boldsymbol{x})\,. \tag{136}$$

In order to satisfy the asymptotic boundary condition (134), the function $\chi_0(R)$ must not contain outgoing momenta contributions. Therefore the Fourier transform of χ_0 must vanish for momenta pointing away from the scattering centre (denoted in the following as *positive momenta*). Otherwise the Fourier integral (135) still defines an eigenfunction of H, but not necessarily one satisfying the outgoing boundary condition (134). Furthermore, the initial wavepacket Ψ_0 is assumed to be located in the asymptotic region, i.e.

$$V_{\mathrm{I}}(R, \boldsymbol{x})\, \Psi_0(R, \boldsymbol{x}) \approx 0\,. \tag{137}$$

For negative times the propagator $\exp(-iHt)$ can then approximately be replaced in Eq. (135) by $\exp(-iH_0 t)$. In contrast to the full Hamiltonian H the free Hamiltonian H_0 cannot induce transitions among the eigenstates. For all negative times the wavepacket (136) thus remains exactly in that eigenstate ξ_ν of the internal Hamiltonian in which it was prepared for $t = 0$.

We now turn to the discussion of the energy distribution $\Delta(E)$ of the initial wavepacket. Since the stationary scattering wavefunction was assumed to be energy normalised, one obtains

$$\begin{aligned}
\delta(E - E') &= \langle \Psi^+_{E'\nu} \,|\, \Psi^+_{E\nu} \rangle \\
&= \frac{1}{2\pi\Delta(E)} \int\limits_{-\infty}^{\infty} \langle \Psi^+_{E'\nu} \,|\, e^{-i(H-E)t} \,|\, \Psi_0 \rangle \, dt \\
&= \frac{1}{2\pi\Delta(E)} \langle \Psi^+_{E'\nu} \,|\, \Psi_0 \rangle \int\limits_{-\infty}^{\infty} e^{-i(E'-E)t} \, dt\,.
\end{aligned} \tag{138}$$

The last integral is a representation of the δ-distribution, and the energy distribution of the initial wavepacket can be written as

$$\Delta(E) = \langle \Psi^+_{E\nu} \,|\, \Psi_0 \rangle\,. \tag{139}$$

Because the initial wavepacket Ψ_0 is located in the asymptotic region, the knowledge of the asymptotic form of the stationary scattering wavefunction

(134) is sufficient in order to determine the energy distribution of the initial wavepacket employing Eq. (139). Since it was required that the initial wavepacket Ψ_0 does not contain positive momenta, $\langle \Phi^+_{E\nu} \,|\, \Psi_0 \rangle = 0$ holds, and the energy distribution of the initial wavepacket reads [116,117]

$$\Delta(E) = \langle \Phi^-_{E\nu} \,|\, \Psi_0 \rangle = \sqrt{\frac{\mu_R}{2\pi p_\nu}} \int\limits_0^\infty \chi_0(R)\, e^{ip_\nu R}\, dR\,. \tag{140}$$

The energy distribution of the initial wavepacket is therewith given as a coordinate-momentum Fourier transform of the wavepacket in the translational coordinate $\chi_0(R)$. The knowledge of the energy distribution $\Delta(E)$ is essential when evaluating cross-sections, reaction probabilities, *etc.* (see Sec. 8.6).

7.2.2 Wentzel-Kramers-Brillouin (WKB) correction of energy distribution

In the case when the interaction potential V_I falls off slowly it becomes increasingly difficult to satisfy Eq. (137). In the following, modifications are introduced which allow the initial wavepacket to be moved closer to the scattering centre as long as the interaction potential does not induce transitions between internal states, i.e. as long as the product form of the initial wavepacket (cf. Eq. (136)) remains essentially exact.

Moving the initial wavepacket towards the scattering centre, the interaction potential becomes non-negligible and the exact scattering wavefunction can no longer be replaced by $\Phi^-_{E\nu}$. However, the validity of Eq. (134) can be extended to considerably smaller R-values if the free wave $\chi^-_{E\nu}$ (cf. Eqs. (131,132)) is replaced by a distorted wave which is the scattering solution of the (diabatic) mean-field potential

$$\bar{V}_\nu(R) = \langle \xi_\nu \,|\, H - T_R \,|\, \xi_\nu \rangle = \langle \xi_\nu \,|\, V_\mathrm{I} \,|\, \xi_\nu \rangle + E_\nu\,. \tag{141}$$

Since the mean-field potential is weak and smooth in the region where $\chi_0(R)$ is localised, the distorted wave can be computed to a good approximation using the WKB method. Hence we set

$$\Phi^-_{E\nu}(R, \boldsymbol{x}) = \chi^\mathrm{WKB}_{E\nu}(R)\, \xi_\nu(\boldsymbol{x})\,, \tag{142}$$

where

$$\chi^\mathrm{WKB}_{E\nu}(R) = \sqrt{\frac{\mu_R}{2\pi}}\, k(R)^{-1/2} \exp\left(-i \int\limits^R k(x)\, dx\right)\,, \tag{143}$$

with the local momenta

$$k(R) = \sqrt{2\,\mu_R\,(E - \bar{V}_\nu(R))} \tag{144}$$

being defined via the mean-field (141).

For the energy distribution of the initial wavepacket Ψ_0 (136) one thus obtains

$$\begin{aligned}\Delta(E) &= \langle \chi^{\mathrm{WKB}}_{E\nu} \xi_\nu \,|\, \Psi_0 \rangle \\ &= \sqrt{\frac{\mu_R}{2\pi}} \int\limits_0^\infty k(R)^{-1/2} \exp\left(i \int\limits^R k(x)\, dx \right) \chi_0(R)\, dR\,. \end{aligned} \tag{145}$$

Note that Eq. (140) is recovered if $\bar{V}_\nu(R) \to 0$. The initial state is left unchanged by the correction but the computation of its energy distribution now accounts for the presence of an interaction potential. To distinguish this correction scheme from the adiabatic one to be discussed next, we call it the *diabatic correction*.

7.2.3 Adiabatic initial state

The range of validity of a separable Hartree-type initial state (cf. Eq. (136)) can be extended if one turns from the diabatic to the adiabatic representation [81] of the internal states. To avoid confusion the set of initial internal quantum numbers will be called ν_0 (rather than ν) in the following.

The adiabatic correction is based on following considerations:

- The representation Eq. (134) of the exact scattering wavefunction is valid (to a very good approximation) for all values of the translational coordinate R for which the interaction potential has dropped to negligible small values. The range of validity of Eq. (134) can be extended to substantially smaller values of the translational coordinate R if the energy normalised free wavefunctions $\Phi^{\pm}_{E\nu_0}$ are replaced by their adiabatic counterparts:

  $$\Phi^{\pm,\mathrm{ad}}_{E\nu_0}(R, \boldsymbol{x}) = \chi^{\pm,\mathrm{ad}}_{E\nu_0}(R)\, \xi^{\mathrm{ad}}_{\nu_0}(\boldsymbol{x}; R)\,, \tag{146}$$

  where $\xi^{\mathrm{ad}}_{\nu_0}(\boldsymbol{x}; R)$ is an eigenfunction of an *adiabatic internal Hamiltonian* (see Eq. (148)). It depends parametrically on R, and in the limit $R \to \infty$ it approaches the diabatic eigenfunction $\xi_{\nu_0}(\boldsymbol{x})$ defined by Eq. (130). The functions $\chi^{\pm,\mathrm{ad}}_{E\nu_0}(R)$ are the scattering solutions of the adiabatic mean-field potential $V^{\mathrm{ad}}_{\nu_0}(R)$ and converge towards the free waves $\chi^{\pm}_{E\nu_0}(R)$ for $R \to \infty$. The WKB approximation is assumed to be sufficiently accurate for computing $\chi^{\pm,\mathrm{ad}}_{E\nu_0}$.

- Similarly, the initial wavepacket Ψ_0 is written as a product of a localised function $\chi_0(R)$, and an adiabatic internal eigenfunction $\xi^{\mathrm{ad}}_{\nu_0}(\boldsymbol{x};R)$,

  $$\Psi_0(R,\boldsymbol{x}) = \chi_0(R)\,\xi^{\mathrm{ad}}_{\nu_0}(\boldsymbol{x};R)\,. \tag{147}$$

  This initial wavepacket may be placed close to the scattering centre provided the internal state $\xi^{\mathrm{ad}}_{\nu_0}$ is not changed by the interaction. Since the adiabatic coupling is usually smaller than the diabatic one, the adiabatic correction scheme is preferable to the diabatic one.

In order to determine the adiabatic eigenfunctions $\xi^{\mathrm{ad}}_{\nu_0}(\boldsymbol{x};R)$ and the adiabatic potentials $V^{\mathrm{ad}}_{\nu_0}(R)$, the adiabatic mean-field Hamiltonian, depending parametrically on the translational coordinate R, is introduced,

$$\bar{H}^{\mathrm{ad}}(\boldsymbol{x};R) = H - T_R \;=\; H_{\mathrm{int}} + V_{\mathrm{I}}(R,\boldsymbol{x})\,, \tag{148}$$

represented in the basis of the (diabatic) internal eigenfunctions $\{\xi_\nu\}$,

$$(\bar{H}^{\mathrm{ad}})_{\nu\nu'} = \langle \xi_\nu \,|\, \bar{H}^{\mathrm{ad}} \,|\, \xi_{\nu'} \rangle \;=\; E_\nu\,\delta_{\nu\nu'} + \langle \xi_\nu \,|\, V_{\mathrm{I}} \,|\, \xi_{\nu'} \rangle\,, \tag{149}$$

and diagonalised,

$$\bar{H}^{\mathrm{ad}}(\boldsymbol{x};R)\,\xi^{\mathrm{ad}}_{\nu}(\boldsymbol{x};R) = V^{\mathrm{ad}}_{\nu}(R)\,\xi^{\mathrm{ad}}_{\nu}(\boldsymbol{x};R)\,. \tag{150}$$

In the limit $R \to \infty$ the adiabatic potentials $V^{\mathrm{ad}}_\nu(R)$ converge towards the corresponding internal energies E_ν of the free fragments. Using the components $c_\nu = \langle \xi_\nu \mid \xi^{\mathrm{ad}}_{\nu_0}\rangle$, i.e. the eigenvectors of the matrix (149), Eq. (147) can be reformulated:

$$\Psi_0(R,\boldsymbol{x}) = \chi_0(R) \sum_{\nu=0}^{\nu_{\max}} c_\nu(R)\,\xi_\nu(\boldsymbol{x})\,. \tag{151}$$

The representation of the wavepacket in Eq. (151) is not yet in the product form (19) required by a MCTDH wavefunction. (The internal wavefunctions ξ_ν are assumed to be already in product form.) Choosing the χ_k as a set of single-particle functions which are orthonormal to χ_0, the MCTDH wavefunction can be expanded in this basis,

$$\Psi_0(R,\boldsymbol{x}) = \sum_{k=0}^{k_{\max}} \sum_{\nu=0}^{\nu_{\max}} A_{k\nu}\,\chi_k(R)\,\xi_\nu(\boldsymbol{x})\,. \tag{152}$$

Taking $\chi_0(R)$ as a Gaussian wavepacket

$$\chi_0(R) = \left(\sqrt{2\pi}\,\sigma_R\right)^{-1/2} \exp\!\left(-\left(\tfrac{R-R_0}{2\sigma_R}\right)^2\right) e^{-ip_0(R-R_0)}\,, \tag{153}$$

all remaining single-particle functions $\chi_k(R)$ are conveniently defined as

$$\chi_k(R) = R^k \chi_0(R) \,, \tag{154}$$

and then Schmidt-orthonormalised. Equating equations (151) and (152), multiplying to the left by $\chi^*_{k'}\xi^*_{\nu'}$, integrating over $\boldsymbol{x}$ and R, and renaming the indices gives the MCTDH expansion coefficients of the adiabatically corrected initial wavepacket,

$$\begin{aligned} A_{k\nu} &= \langle \chi_k \, \xi_\nu \,|\, \Psi_0 \rangle \\ &= \int\limits_0^\infty \chi^*_k(R) \, \chi_0(R) \, c_\nu(R) \, dR \,. \end{aligned} \tag{155}$$

Defining the local WKB momenta by the adiabatic potential

$$k(R) = \sqrt{2 \, \mu_R \left(E - V^{\mathrm{ad}}_{\nu_0}(R) \right)} \,, \tag{156}$$

one obtains for the WKB-corrected energy distribution of the adiabatic initial wavepacket Ψ_0, Eq. (147):

$$\begin{aligned} \Delta(E) &= \langle \chi^{\mathrm{WKB}}_{E\nu_0} \xi^{\mathrm{ad}}_{\nu_0} \,|\, \Psi_0 \rangle \\ &= \sqrt{\frac{\mu_R}{2\pi}} \int\limits_0^\infty k(R)^{-1/2} \exp\left(i \int\limits^R k(x) \, dx \right) \chi_0(R) \, dR \,. \end{aligned} \tag{157}$$

The energy distributions of the diabatic and of the adiabatic initial wavepackets — see Eqs. (145) and (157) — are formally identical, but differ in the definition of their local WKB momenta (see Eqs. (144) and (156)). Whereas the diabatic correction only changes the energy distribution $\Delta(E)$, the adiabatic correction additionally modifies the form of the initial wavepacket compared with the free state (136).

A more comprehensive discussion of the correction scheme can be found in Refs. [45,109] where (reactive) atom–diatom scattering is considered. For collinear H+H_2 reactive scattering it was found that the centre of the initial wavepacket had to be placed at $R_0 = 6.78\,\text{a.u.}$, $R_0 = 4.76\,\text{a.u.}$, or $R_0 = 4.12\,\text{a.u.}$, when no, diabatic, or adiabatic correction is used [109]. A similar reduction from 7.5 a.u (no correction) to 4.5 a.u. (adiabatic correction) was found in 3D ($J = 0$) calculations [45]. The correction becomes essential when going to larger total angular momenta [46].

8 Analysis

The propagated wavefunction contains all the information necessary to determine the observable quantities of interest. In the analysis step these quantities are extracted from the wavefunction. To be applicable to an MCTDH calculation, an analysis method has to be compatible with the particular form of the wavefunction (19). For an approximate method like MCTDH it is also important to monitor the accuracy of a calculation after, or better during, the propagation.

8.1 Matrix elements of operators

When extracting observable quantities from an MCTDH calculation, one often has to take into account the fact that two MCTDH wavefunctions, either at different times or from different calculations, are in general formed in different basis sets, because the single-particle functions are time-dependent. This, for example, prohibits the simple summation of MCTDH wavefunctions. Hence, Fourier transforming $\Psi(t)$ is a difficult task.

In general, use is made of the fact that matrix elements of operators in product form can be evaluated very quickly. Let $\Psi = \sum_J A_J \Phi_J$ and $\tilde{\Psi} = \sum_L \tilde{A}_L \tilde{\Phi}_L$ be two MCTDH wavefunctions, and let $\hat{\Omega} = \sum_r^M c_r \, \hat{\omega}_r^{(1)} \cdots \hat{\omega}_r^{(f)}$ be an operator given in product form, then

$$\begin{aligned}\langle \Psi \,|\, \hat{\Omega} \,|\, \tilde{\Psi} \rangle = & \sum_{r=1}^{M} c_r \sum_{j_1} \dots \sum_{j_f} A^*_{j_1 \dots j_f} \\ & \times \sum_{l_1} \langle \varphi^{(1)}_{j_1} \,|\, \hat{\omega}^{(1)}_r \,|\, \tilde{\varphi}^{(1)}_{l_1} \rangle \dots \sum_{l_f} \langle \varphi^{(f)}_{j_f} \,|\, \hat{\omega}^{(f)}_r \,|\, \tilde{\varphi}^{(f)}_{l_f} \rangle \tilde{A}_{l_1 \dots l_f} \,. \end{aligned} \tag{158}$$

Only one-dimensional integrals are thus required.

In the following subsections, the single-set formulation is used to simplify the notation. Extension to the multi-set formalism, important for non-adiabatic calculations can be made, remembering that the single-particle function sets of the various electronic states are not orthonormal to each other.

8.2 Difference between MCTDH wavefunctions

A useful quantity that shows the accuracy of a calculation is the time evolution of the difference between wavefunctions propagated under different conditions, e.g. different numbers of single-particle functions, different integrators, or the comparison of a numerically exact wavefunction with an MCTDH one. By a reformulation of the problem, sums and differences of MCTDH wavefunctions can be simply evaluated.

For example the straightforward difference between two wavefunctions,

$$\Delta = \| \Psi - \tilde{\Psi} \| \,, \tag{159}$$

can be evaluated using the relationship

$$\| \Psi - \tilde{\Psi} \|^2 = \| \Psi \|^2 + \| \tilde{\Psi} \|^2 - 2 \, \mathrm{Re} \, \langle \Psi \, | \, \tilde{\Psi} \rangle \,, \tag{160}$$

and use then made of Eq. (158), with $\hat{\omega}_s^{(\kappa)} = 1$, to write the overlap $\langle \Psi \mid \tilde{\Psi} \rangle$ as a sum of one-dimensional overlaps of the single-particle functions.

For the analysis of the difference between two wavefunctions it is also informative to calculate the phase error

$$\phi = \arctan \left(\frac{\mathrm{Im} \, \langle \Psi \, | \, \tilde{\Psi} \rangle}{\mathrm{Re} \, \langle \Psi \, | \, \tilde{\Psi} \rangle} \right) . \tag{161}$$

This may then be used to define the phase corrected error

$$\bar{\Delta}^2 = \| \Psi - e^{-i\phi} \tilde{\Psi} \|^2 = \| \Psi \|^2 + \| \tilde{\Psi} \|^2 - 2 \, | \langle \Psi \, | \, \tilde{\Psi} \rangle | \ . \tag{162}$$

Note that $\bar{\Delta}$ is computed without explicitly knowing ϕ. It is clear that $\bar{\Delta} \leq \Delta$ holds. If $\bar{\Delta} \ll \Delta$ one should suspect large phase errors caused, for example, by an inconsistent definition of the zero points of the potential energies.

A further useful quantity is the Hilbert-space angle:

$$\vartheta = \arccos \left(\frac{| \langle \Psi \, | \, \tilde{\Psi} \rangle |}{\| \Psi \| \, \| \tilde{\Psi} \|} \right) . \tag{163}$$

This error measure is sensitive to the form of the wavefunction only; it is insensitive to both phase and norm errors.

Auto- and cross-correlation functions are simple overlaps between wavefunctions. They are thus easy to evaluate with the aid of Eq. (158) by setting $\hat{\Omega} = 1$. Of particular interest is the auto-correlation function because it contains all information necessary for determining absorption spectra.

The auto-correlation function $c(t)$ is defined as the overlap between the initial and the propagated wavefunction, i.e.

$$c(t) = \langle \Psi(0) \,|\, \Psi(t) \rangle \,. \tag{164}$$

If the Hamiltonian is Hermitian it fulfils the relation

$$c(-t) = c^*(t) \,. \tag{165}$$

Fortunately, this relation remains true for a CAP augmented Hamiltonian, because one has to switch the sign of the CAP for negative times to ensure that the wavepacket is absorbed for $t \to -\infty$ as well.

Furthermore, as

$$\begin{aligned} &\langle \Psi(0) \,|\, \exp(-iHt) \,|\, \Psi(0) \rangle \\ &\qquad = \left\langle \left(\exp(-iH^{\dagger *}t/2)\, \Psi^*(0) \right)^* \,|\, \exp(-iHt/2)\, \Psi(0) \right\rangle \,, \end{aligned} \tag{166}$$

the following very useful relation is obtained [31,118,119] if the initial state $\Psi(0)$ is real and the Hamiltonian is symmetric (i.e. $H = H^T \equiv H^{\dagger *}$) :

$$c(t) = \langle \Psi^*(t/2) \,|\, \Psi(t/2) \rangle \,. \tag{167}$$

The Hamiltonians we are dealing with are usually real symmetric and thus both Eqs. (165) and (167) hold even when a CAP is augmented. Because Eq. (167) allows the propagation of the wavefunction Ψ over only half the time for which the auto-correlation function is needed, this is the preferable way to compute $c(t)$. Note that for an approximate propagation method the two expressions above are not strictly equivalent. In general, Eq. (167) is the more accurate one because wavefunctions at earlier times contain smaller errors.

The auto-correlation function can be utilised in the computation of photo-dissociation or photo-absorption spectra. Let $\Psi_i(\boldsymbol{Q}, 0)$ denote the nuclear wavefunction of the initial electronic state, with $\boldsymbol{Q}$ being the vector of the nuclear coordinates $Q_1, \ldots, Q_f$. The nuclear wavefunction of the excited electronic state is then determined by $\Psi_f(\boldsymbol{Q}, 0) = \boldsymbol{e} \cdot \boldsymbol{\mu}_{fi}(\boldsymbol{Q})\, \Psi_i(\boldsymbol{Q}, 0)$, where $\boldsymbol{e}$

specifies a unit vector in the direction of the electric field and $\boldsymbol{\mu}_{fi}$ is the transition dipole moment vector. (Within the Condon approximation, the transition dipole moment is assumed to be independent of the nuclear coordinates $\boldsymbol{Q}$, implying a vertical transition from the initial to the excited state.) Propagating $\Psi_f(\boldsymbol{Q},0)$ in time on the excited potential energy surface yields $\Psi_f(\boldsymbol{Q},t)$ and the corresponding auto-correlation function $c(t)$. From this one obtains the total absorption cross-section at photon energy E by

$$\sigma(E) \;\sim\; E\int_{-\infty}^{+\infty} c(t)\, e^{i(E+E_i)t}\, dt = 2E\int_{0}^{\infty} \mathrm{Re}\left(c(t)\, e^{i(E+E_i)t}\right) dt\,, \tag{168}$$

i.e. the Fourier transform of the auto-correlation function (see e.g. Ref. [2] for a derivation). Here E_i is the energy of the initial state.

The auto-correlation function $c(t)$ vanishes for increasing t when the system is dissociating. For bound systems, however, $c(t)$ does not vanish and one introduces an approximation if one replaces the upper limit of integration in Eq. (168) by some finite time T. (Remember that due to Eq. (167) the propagation can be stopped at $T/2$.) The thus computed spectrum is the exact one convoluted with the resolution function

$$\tilde{g}_0(E) = 2\sin\left(ET\right)/E\,. \tag{169}$$

This convolution broadens the computed spectrum and introduces spurious structures into the spectrum (Gibbs phenomenon) because of the long oscillating tails of $\tilde{g}_0$. This spurious cut-off effect can be weakened (at the price of a slightly larger broadening) by multiplying the auto-correlation function with some appropriate damping function $g(t)$. A convenient choice is

$$g(t) = \cos\left(\frac{\pi t}{2T}\right)\,\theta\left(1-|t|/T\right)\,, \tag{170}$$

where $\theta(x)$ denotes Heaviside's step function. Multiplying $c(t)$ with $g(t)$ is equivalent to convoluting the spectrum with the Fourier transform of $g(t)$, which in this case reads

$$\tilde{g}(E) = \frac{4\pi T\cos(ET)}{(\pi-2ET)\,(\pi+2ET)}\,. \tag{171}$$

Note that $\tilde{g}$ falls off with E^{-2} for large detunings E, whereas $\tilde{g}_0$ falls off only with E^{-1}. The negative parts of $\tilde{g}$ are also much smaller than those of $\tilde{g}_0$. The full width at half maximum (FWHM) is $\Delta E = 2.5$ eV·fs/T for $\tilde{g}_0$ and $\Delta E = 3.4$ eV·fs/T for $\tilde{g}$.

Equation (168) of the previous section can be employed in the computation of continuous spectra, as found in photo-dissociation processes, or quasicontinuous spectra, as found in photo-absorption processes of bound systems in which the ro-vibrational energy levels are extremely numerous and dense. If one is however interested in fully resolving the ro-vibrational spectrum of a bound system, the Fourier technique is not a suitable method, since it would require impracticable long propagation times to determine the discrete energy levels.

A very efficient and accurate time-dependent approach to such applications is the filter-diagonalisation (FD) method [120–122]. In the FD scheme a short-time wavefunction propagation is used to construct a finite basis set that covers the space spanned by those eigenfunctions of the Hamiltonian that represent a given energy range. Hereby the contributions of distant eigenstates are removed. Contributions of closely lying states are then eliminated by diagonalising a small Hamiltonian matrix, formed in these basis functions, to yield the eigenvalues in the given energy window. If desired, the entire spectrum can be determined by employing different windows. The FD algorithm can also be applied to the extraction of energies and widths of resonant states [123–125].

When an approximate propagation method like MCTDH is combined with the FD method, higher order auto-correlation functions

$$c^{(k)}(t) = \langle \Psi(0) \,|\, H^k \,|\, \Psi(t) \rangle \,, \qquad k = 0, 1, 2 \,, \tag{172}$$

can be utilised to increase the accuracy of the results [126]. For a real initial state these functions can again be computed more efficiently via

$$c^{(k)}(t) = \langle \Psi^*(t/2) \,|\, H^k \,|\, \Psi(t/2) \rangle \,. \tag{173}$$

The relation $c^{(k)}(-t) = {c^{(k)}}^*(t)$ also holds.

The efficiency and accuracy of the FD framework can be further increased by using cross- rather than auto-correlation functions [121,127,128]. Instead of propagating a single wavepacket and determining its auto-correlation function, one then evolves S initial wavepackets, $\Psi_1(0), \ldots, \Psi_S(0)$, and computes the cross-correlation matrices

$$c^{(k)}_{\alpha\beta}(t) = \langle \Psi_\alpha(0) \,|\, H^k \,|\, \Psi_\beta(t) \rangle \,; \quad k = 0, 1, 2 \,; \quad \alpha, \beta = 1, \ldots, S \,. \tag{174}$$

(The analogue of Eq. (173) is also valid.) As the informational content of the cross-correlation matrices is by about a factor S larger than that of the single auto-correlation function, one obtains a similar accuracy of the results with a propagation time that is shorter by a factor of S. Since approximate propagation methods are more accurate for short time evolution, the use of cross-correlation functions is favourable within the MCTDH scheme.

Up to now no calculations have been performed that combine an MCTDH wavefunction propagation with the filter-diagonalisation method. However, having in mind the accuracy and efficiency of both the MCTDH and the FD method, this hybrid approach seems very promising to us. If our expectations are fulfilled, this would open a new field of applications for the MCTDH method. Work on this is in progress.

8.5 State populations

For systems which involve more than one electronic state, a quantity of particular interest is of course the population $p_\alpha(t)$ of each state α as a function of time t. The evaluation of the state population depends on whether one uses the single- or multi-set formulation (see Sec. 3.5). In the multi-set approach, the state population is simply given by the norm of the corresponding state function, i.e.

$$p_\alpha(t) = \| \, \Psi^{(\alpha)}(t) \, \|^2 \, , \tag{175}$$

with $\Psi^{(\alpha)}$ defined as in Eq. (59). In the single-set formulation, the state population can be computed with the aid of the density matrix, Eq. (27), as

$$p_\alpha(t) = \rho^{(\kappa_e)}_{\alpha\alpha}(t) \, , \tag{176}$$

where κ_e denotes the electronic degree of freedom.

8.6 Excitation and reaction probabilities computed by flux analysis

When investigating scattering processes through wavepacket propagation one finally has to determine the S-matrix elements from the knowledge of the time-dependent wavepacket. A straightforward way to compute S-matrix elements is to propagate the wavepacket well into the asymptotic region of the product arrangement channel and than project it onto the free asymptotic states [129–131,33], i.e. onto a product of a free wave in the dissociative coordinate and an eigenstate of the internal product channel Hamiltonian. Note that the projection onto a free wave is equivalent to a position-momentum (R, p)-Fourier transform.

A second class of algorithms makes use of an energy-time (E, t)-Fourier transform to (formally) generate the time-independent energy-normalised scattering solution with outgoing boundary conditions Ψ_E^+ (see Eqs. (133) to (135)). One may then evaluate [132] the T-matrix elements by the well-known expression $T_{fi} = \langle \Phi_{E,f} \,|\, V \,|\, \Psi_{E,i} \rangle$. This, however, requires that the wavepacket is Fourier transformed at *every* grid point.

A more efficient procedure is to evaluate the S-matrix elements by inspecting the asymptotic behaviour of Ψ_E^+. This method, developed by Balint-Kurti *et al.* [133,134], requires the (E, t)-Fourier transform of the wavepacket (or overlaps thereof) only at the surface $R = R_c$, where R_c is chosen such that the interaction potential can be considered to vanish for all $R \geq R_c$ (R denotes the coordinate leading to dissociation).

The more recent treatment of Tannor and Weeks [116,117,135] is very similar to that of Balint-Kurti's approach, although the derivations of the two methods look quite different. In fact the Tannor and Weeks approach becomes equivalent to the Balint-Kurti formalism when the final wavepacket is chosen to be a product of the δ-function $\delta(R - R_c)$ with an eigenstate of the internal channel Hamiltonian.

An important advantage of the two latter methods is that the wavefunction is no longer needed for $R > R_c$. One may hence remove it in this region with the aid of a complex absorbing potential (CAP) (see Sec. 4.7). This allows shorter grids to be used than in the projection method mentioned above.

The fourth method to be discussed makes use of the flux operator to determine excitation or reaction *probabilities*, i.e. modulo squares of S-matrix elements, or even of sums of these. The first extensive use of flux operators was made by Miller, Schwartz and Tromp [136], when they derived formally exact expressions for quantum mechanical rate constants. Later this work was extended to compute rate constants and cumulative [96,97] as well as state specific [137] reaction probabilities within a time-independent formalism.

In the time-dependent picture of reactive scattering, Neuhauser *et al.* [138,139] were the first to employ flux operators to extract total as well as state specific reaction probabilities from the time-dependent wavepacket. This has since become the standard method [140–143].

In the following, the latter approach will be extended and a convenient and efficient formula for evaluating reaction probabilities will be derived [109]. Our formalism does not require the derivative (with respect to the dissociative coordinate) of the wavepacket. More importantly, it avoids the need to (E, t)-Fourier transform the wavepacket at every grid point on the dividing surface (or equivalently to (E, t)-Fourier transform every overlap of the wavepacket at the dividing surface with a (complete) set of internal functions). Only Fourier integrals over matrix elements are required. This feature makes the proposed method particularly well suited for analysing wavepackets that are propagated with MCTDH.

8.6.1 Coordinate systems and arrangement channels

In a similar manner to Sec. 7.2 we distinguish a translational coordinate R from the internal coordinates $\boldsymbol{x}$. However, when turning to reactive scattering there are different arrangement channels because the system can fragment into different subsystems (e.g. into AB+C, AC+B, or BC+A in the case of a triatomic system). Hence each channel has its own separation into translational and internal coordinates and the coordinates, wavefunctions and operators must now be characterised by an additional channel index. In the following we will denote the initial (reactant) channel by α and a general arrangement channel by γ. The equations in Sec. 7.2.1 then generalise to

$$\begin{aligned}
H &= H_0^\gamma + V_\mathrm{I}^\gamma &(177)\\
H_0^\gamma &= T_R^\gamma + H_\mathrm{int}^\gamma &(178)\\
H_\mathrm{int}^\gamma\, \xi_{\gamma\nu}(\boldsymbol{x}_\gamma) &= E_{\gamma\nu}\, \xi_{\gamma\nu}(\boldsymbol{x}_\gamma) &(179)\\
\Phi^\pm_{E\gamma\nu}(R_\gamma, \boldsymbol{x}_\gamma) &= \chi^\pm_{E\gamma\nu}(R_\gamma)\, \xi_{\gamma\nu}(\boldsymbol{x}_\gamma) &(180)\\
\Psi^+_{E\alpha\nu}(R_\gamma, \boldsymbol{x}_\gamma) &\xrightarrow{R_\gamma\to\infty} \Phi^-_{E\alpha\nu}(R_\alpha, \boldsymbol{x}_\alpha)\, \delta_{\alpha\gamma} \\
&\qquad - \sum_{\nu'} S_{\gamma\nu',\alpha\nu}(E)\, \Phi^+_{E\gamma\nu'}(R_\gamma, \boldsymbol{x}_\gamma) &(181)\\
\Psi_0(R_\alpha, \boldsymbol{x}_\alpha) &= \chi_0(R_\alpha)\, \xi_{\alpha\nu}(\boldsymbol{x}_\alpha)\,. &(182)
\end{aligned}$$

Remember that $\Phi^\pm_{E\gamma\nu}$ and $\Psi^+_{E\alpha\nu}$ are eigenfunctions of H_0^γ and H, respectively, with eigenenergy E. The initial state Ψ_0 is $\mathcal{L}^2$-normalised. Additionally, Eqs. (132) and (135) have to be generalised to include the arrangement channel index γ.

8.6.2 Flux operator and scattering matrix

Let Θ_γ be a characteristic function in the asymptotic part of arrangement channel γ, i.e. Θ_γ is 1 there and 0 everywhere else. The occupation of this region changes according to

$$\frac{d}{dt}\langle\Psi\,|\,\Theta_\gamma\,|\,\Psi\rangle = i\,\langle\Psi\,|\,[H,\Theta_\gamma]\,|\,\Psi\rangle\,. \qquad (183)$$

Since this time derivative of the occupation is the flux going into arrangement channel γ, one defines the flux operator by

$$F_\gamma = i\,[H,\Theta_\gamma]\,. \qquad (184)$$

An obvious choice for Θ_γ is given by

$$\Theta_\gamma = \theta\left(R_\gamma - R_{\gamma c}\right) \, , \tag{185}$$

where θ denotes Heaviside's step function, and where $R_{\gamma c}$ is chosen to be sufficiently large to ensure asymptotic motion for all $R_\gamma \geq R_{\gamma c}$.

Since this Θ_γ commutes with the interaction potential and with H^γ_{int}, one arrives at

$$F_\gamma = \frac{-i}{2\mu_{R_\gamma}} \left(\frac{\partial}{\partial R_\gamma} \, \delta(R_\gamma - R_{\gamma c}) + \delta(R_\gamma - R_{\gamma c}) \, \frac{\partial}{\partial R_\gamma} \right) \, . \tag{186}$$

It is now easy to compute the expectation value of this operator. With the aid of Eqs. (132), (180), and (181) it follows for $\gamma \neq \alpha$ that

$$\langle \Psi^+_{E\alpha\nu} \,|\, F_\gamma \,|\, \Psi^+_{E\alpha\nu} \rangle = \frac{1}{2\pi} \sum_{\nu'} |S_{\gamma\nu',\alpha\nu}(E)|^2 \, . \tag{187}$$

The sum over the internal states may be removed by employing projectors onto these states,

$$P_{\gamma\nu} = |\, \xi_{\gamma\nu} \rangle \langle \xi_{\gamma\nu} \,| \, , \tag{188}$$

yielding

$$\langle \Psi^+_{E\alpha\nu} \,|\, P_{\gamma\nu'} F_\gamma P_{\gamma\nu'} \,|\, \Psi^+_{E\alpha\nu} \rangle = \frac{1}{2\pi} \, |\, S_{\gamma\nu',\alpha\nu}(E) \,|^2 \, . \tag{189}$$

The flux through a surface is independent of the detailed shape of the surface. This is an important point because it allows us to choose the dividing surface (i.e. the surface where Θ_γ jumps from zero to one) quite arbitrarily as long as it separates the arrangement channel γ from the rest. Equations (187) and (189) remain valid for any such dividing surface.

8.6.3 Flux analysis via complex absorbing potentials

Having introduced the notation, we are ready to derive an expression for the calculation of initial-state selected reaction probabilities and state-to-state inelastic reaction probabilities from a time-dependent wavepacket utilising complex absorbing potentials (CAPs) [109].

CAPs were introduced originally [88,89] in order to artificially damp those parts of the wavefunction which penetrate the outer regions of the grid (see

Sec. 4.7). This ensures that the amplitude of the wavefunction remains zero at the edges and thus allows smaller grid sizes. As demonstrated by Neuhauser *et al.* (see Ref. [144] and references therein) CAPs can also effectively decouple scattering into any particular arrangement channel from that into others and therefore allow the propagation of the initial wavepacket solely in the reagent arrangement channel coordinates. Here we show that CAPs cannot only be used for these purposes, but also for an efficient calculation of the flux and hence of reaction or excitation probabilities [109].

In order to derive the working equations we replace the system's Hamiltonian H by (the no longer Hermitian) Hamiltonian $\tilde{H}$,

$$\tilde{H} = H - iW\,, \tag{190}$$

where $-iW$ is a complex absorbing potential which can be split with respect to the different arrangement channels,

$$W = W_\alpha + W_\beta + \dots\ . \tag{191}$$

Here the W_γ ($\gamma = \alpha, \beta, \ldots$) are real non-negative potential functions that vanish outside the region characterised by Θ_γ, i.e.

$$\Theta_\gamma W = \Theta_\gamma W_\gamma = W_\gamma\,. \tag{192}$$

To give an example: When Θ_γ is given by Eq. (185), then one may choose W_γ to be

$$W_\gamma(R_\gamma, \boldsymbol{x}_\gamma) = \eta_\gamma\,(R_\gamma - R_{\gamma c})^2\,\theta(R_\gamma - R_{\gamma c})\,, \tag{193}$$

where η_γ denotes an appropriately chosen strength parameter. However, as emphasised above, more general forms of Θ_γ and W_γ are possible.

If the CAP is non-reflecting — this can essentially be achieved by making the CAP strengths $\eta_{\tilde{\gamma}}$ sufficiently small — then one may propagate the initial wave packet Ψ_0 by H rather than by H without changing the values of the propagated wavefunction at points where the CAP vanishes.

Thus propagating with $\tilde{H}$ and employing Eqs. (135) and (182) one may write the reactive flux going into product arrangement channel $\gamma \neq \alpha$ as

$$\begin{aligned} &\langle \Psi^+_{E\alpha\nu} \,|\, F_\gamma \,|\, \Psi^+_{E\alpha\nu} \rangle \\ &\quad = \frac{1}{(2\pi)^2\,|\,\Delta(E)\,|^2} \int\limits_{-\infty}^{\infty} dt \int\limits_{-\infty}^{\infty} dt'\, \langle \Psi_0 \,|\, e^{i(\tilde{H}^\dagger - E)t} F_\gamma\, e^{-i(\tilde{H}-E)t'} \,|\, \Psi_0 \rangle\,. \end{aligned} \tag{194}$$

The initial wavepacket Ψ_0 is located in the reagent arrangement channel α but outside the CAP. It can reach the product arrangement channel $\gamma \neq \alpha$ only for positive times because of its particular momentum distribution. Hence we may safely replace the two lower integral limits by zero. Moreover, the flux operator F_γ, defined as the commutator of the system's Hamiltonian and of an appropriately chosen characteristic function, can be written as (see Eqs. (190) to (192))

$$F_\gamma \equiv i[H, \Theta_\gamma] = i[\tilde{H}, \Theta_\gamma] = 2W_\gamma + i(\tilde{H}^\dagger - E)\Theta_\gamma - i\Theta_\gamma(\tilde{H} - E)\,. \tag{195}$$

Inserting the last expression into Eq. (194) leads to

$$\begin{aligned} &\langle \Psi^+_{E\alpha\nu} \,|\, F_\gamma \,|\, \Psi^+_{E\alpha\nu} \rangle \\ &\quad = \frac{1}{(2\pi)^2 \,|\,\Delta(E)\,|^2} \int\limits_0^\infty dt \int\limits_0^\infty dt' \left[2\,\langle \Psi_0 \,|\, e^{i(\tilde{H}^\dagger - E)t}\, W_\gamma\, e^{-i(\tilde{H}-E)t'} \,|\, \Psi_0 \rangle \right. \\ &\qquad \left. + \left(\frac{d}{dt} + \frac{d}{dt'} \right) \langle \Psi_0 \,|\, e^{i(\tilde{H}^\dagger - E)t}\, \Theta_\gamma\, e^{-i(\tilde{H}-E)t'} \,|\, \Psi_0 \rangle \right]. \end{aligned} \tag{196}$$

This expression can be further simplified. Because $\Theta_\gamma \Psi_0 = 0$ and $e^{-i\tilde{H}t}\Psi_0 \to 0$ for $t \to \infty$ due to the CAPs, the integral over the time-derivatives vanishes.

Defining $\Psi(t) = e^{-i\tilde{H}t}\Psi_0$ and using Eq. (187) we arrive at the desired result

$$\sum_{\nu'} |\, S_{\gamma\nu',\alpha\nu}(E)\,|^2 = \frac{1}{\pi \,|\, \Delta(E)\,|^2} \int\limits_0^\infty dt \int\limits_0^\infty dt'\, \langle \Psi(t) \,|\, W_\gamma \,|\, \Psi(t') \rangle\, e^{-iE(t-t')}\,. \tag{197}$$

In order to obtain an expression which can be evaluated more efficiently, Eq. (197) is reformulated:

$$\sum_{\nu'} |\, S_{\gamma\nu',\alpha\nu}(E)\,|^2 = \frac{2}{\pi \,|\, \Delta(E)\,|^2}\, \mathrm{Re} \int\limits_0^\infty g(\tau)\, e^{iE\tau}\, d\tau\,, \tag{198}$$

where

$$g(\tau) = \int\limits_0^\infty dt\, \langle \Psi(t) \,|\, W_\gamma \,|\, \Psi(t+\tau) \rangle\,. \tag{199}$$

Equations (198) and (199) are the working equations. They relate the time-evolution of the initial wavepacket Ψ_0, via the product arrangement channel CAP W_γ, to the desired initial-state selected reaction probabilities. The energy distribution $\Delta(E)$ of the initial wavepacket determines the energy range for which the reaction probabilities can be computed in one step from a single propagation.

When state-to-state transition probabilities are required, one may adopt Eq. (189) to obtain

$$|\,S_{\gamma\nu',\alpha\nu}(E)\,|^2 = \frac{2}{\pi\,|\,\Delta(E)\,|^2}\,\mathrm{Re}\int_0^\infty g_{\gamma\nu'}(\tau)\,e^{iE\tau}\,d\tau\,, \tag{200}$$

with $g_{\gamma\nu'}$ defined as

$$g_{\gamma\nu'}(\tau) = \int_0^\infty dt\,\langle\Psi(t)\,|\,P_{\gamma\nu'}W_\gamma P_{\gamma\nu'}\,|\,\Psi(t+\tau)\rangle\,. \tag{201}$$

Here it is appropriate to add several remarks:

- Since the wavepacket is absorbed with increasing time, the integrals (197) to (201) converge rapidly, and their upper limit can safely be replaced by a finite time.
- For the sake of simplicity we have assumed that W_γ is real. In the case when one is using a complex function, or even a general operator (that must however commute with Θ_γ), one should replace W_γ in Eqs. (197), (199), and (201) by $(W_\gamma^\dagger + W_\gamma)/2$.
- We have always assumed $\gamma \neq \alpha$. However, one can show that the working equations (197) to (201) remain valid for $\gamma = \alpha$.
- Since we are propagating only forward in time, a backward moving part in Ψ_0 (i.e. a contribution from positive momenta) is not harmful. The backward moving part gets immediately absorbed by W_α and plays no further role. Hence in this respect there is no need to carefully design Ψ_0. However, if non-reactive or elastic scattering is considered, ($\gamma = \alpha$ in Eqs. (198) and (199) or $\gamma = \alpha$ and $\nu = \nu'$ in Eqs. (200) and (201)) Ψ_0 must not contain a backwards moving contribution.
- The propagation of the wavepacket and the evaluation of the matrix elements of W_γ (cf. Eqs. (197) and (199)) may be performed in any suitable coordinate system. The projector $P_{\gamma\nu}$, however, can be expressed conveniently only in the Jacobian coordinates of the arrangement channel γ. Equations (200) and (201) are thus particularly useful when inelastic non-reactive scattering is considered.
- So far it has been assumed that the dividing surface and therewith the product CAP are placed in the asymptotic region of the product channel, where the interaction potential is negligible. This constraint can be relaxed. It is possible to move the dividing surface closer to the scattering centre, as long as the interaction potential remains too weak to change the direction of parts of the flux from reactive to non-reactive, or — in cases when Eq. (200) is used — to cause transitions among the internal states ν'.

8.6.4 Numerical considerations

In order to roughly estimate the numerical effort, let us assume that the wavefunction depends on f coordinates and is represented on a product grid consisting of N points in each of the f dimensions. The wavefunction is thus represented by N^f points. The absorbing potential W_γ vanishes at most of the grid points; it is non-zero on mN^{f-1} points with $m \ll N$. Let T denote the number of time-quadrature points, i.e. times at which $\Psi(t)$ is known.

The numerical effort of the proposed method lies almost entirely in evaluating the matrix elements $W_{tt'} = \langle \Psi(t) \,|\, W_\gamma \,|\, \Psi(t') \rangle$ which — because of the $t \leftrightarrow t'$ exchange symmetry — requires $\frac{1}{2}T^2 m N^{f-1}$ operations. Employing, for example, the flux operator approach developed by Neuhauser *et al.* (see Ref. [144] and references therein) one must perform a time-energy Fourier transform of the wavepacket and of its spatial derivative on the $(f-1)$-dimensional hypersurface that separates the arrangement channels. The numerical effort thus amounts to approximately $2N^{f+1} T \log_2 T$, which in fact is preferable to the scaling mentioned above.

The effort of calculating the matrix elements $W_{tt'}$ is drastically reduced when propagating the wavepacket within the MCTDH scheme. The CAP is an operator which is in MCTDH product form (cf. Eq. (158)) consisting usually of only a single term. Assuming that there are n single-particle functions for each degree of freedom one finds that the effort scales with $\frac{1}{2}T^2 f (n^{f+1} + n^2 N)$. Since n is typically 3 to 20 times smaller than N, the latter effort may be considerably smaller than the above one, in particular when treating many degrees of freedom. More importantly, Eqs. (197) and (201) can make use of the MCTDH form of the wavepacket. This ensures that the size of the memory required stays comparatively small ($\approx 2n^f + 2fnN$ complex numbers). The conventional flux method [144] requires the storage of at least N^{f-1} complex numbers, which may become a difficult task for large f.

8.7 Run-time analysis of the accuracy of the propagation

Due to the approximate nature of MCTDH, it is important to have internal run-time checks on the accuracy of the calculation.

The simplest check made on a calculation is that, unless CAPs are included in the Hamiltonian, the norm and the energy remain constant. Using Eq. (158) with $\tilde{\Psi} = \Psi$ and $\hat{\Omega} = 1$, and assuming that the single-particle functions remain orthonormal, one obtains a simple expression for the norm:

$$\| \Psi \| = \sqrt{\langle \Psi \,|\, \Psi \rangle} = \left(\sum_{j_1} \cdots \sum_{j_f} A^*_{j_1 \ldots j_f} A_{j_1 \ldots j_f} \right)^{1/2} . \tag{202}$$

For a more detailed analysis, loss of orthonormality must also be considered, and Eq. (158) must be used, i.e. the overlap matrices of the single-particle functions are to be included.

To efficiently evaluate the energy during the propagation, use can be made of the relationship between the time-derivative of the A-coefficients and the Hamiltonian (Eq. (40) or Eq. (43)) to avoid the re-evaluation of the non-separable part of the Hamiltonian in the single-particle function basis.

An important criterion for the quality of an MCTDH calculation is the convergence with respect to the single-particle function basis set. A measure of this is given by the natural populations (see Sec. 3.3). The population of the natural orbitals reflect their importance in the representation of the wavefunction. If the highest natural orbital thus has a small population, and as the addition of further single-particle functions will have an even smaller effect, the calculation can be taken as being converged.

Unfortunately, different properties have different sensitivities to changes in the wavefunction, and the natural populations do not provide an absolute measure of convergence. For example the wavefunction required for the calculation of an auto-correlation function does not seem to be as sensitive as that required to calculate transition probabilities. In our experience, for the former natural orbitals with a population less than 10^{-3} can be ignored, while in the latter all natural orbitals with a population greater than 10^{-5} are required.

A more direct measure of convergence can be obtained by looking at the effect of the highest natural orbital on the property of interest. After transforming the basis functions, φ, to natural orbitals, $\tilde{\varphi}$, the wavefunction can be written in terms of the natural orbitals for the κth particle as

$$\Psi(t) = \sum_{j=1}^{n_\kappa} \sqrt{\rho_j^{(\kappa)}}\, \tilde{\varphi}_j^{(\kappa)} \tilde{\Psi}_j^{(\kappa)} , \tag{203}$$

where $\rho_j^{(\kappa)}$ is the jth eigenvalue of the density matrix $\rho^{(\kappa)}$, and $\tilde{\Psi}_j^{(\kappa)}$ is a normalised single-hole function, analogous to Eq. (25), using the natural orbitals as single-particle functions. We now define the wavefunction ignoring the least populated natural orbital,

$$\psi_{(n-1)}^{(\kappa)} = \sum_{j=1}^{n_\kappa - 1} \sqrt{\rho_j^{(\kappa)}}\, \tilde{\varphi}_j^{(\kappa)} \tilde{\Psi}_j^{(\kappa)} \tag{204}$$

and estimate the change in the property on removing this natural orbital. For example, for the auto-correlation function:

$$\begin{aligned}\Delta^{(\kappa)}(t) &= |\, C(t) - \tilde{C}(t)\,|^2 \\ &= |\, \langle \Psi(0)\,|\,\Psi(t)\rangle - \langle \Psi(0)\,|\,\psi_\kappa^{(n-1)}(t)\rangle\,|^2 \\ &= \rho_{n_\kappa}^{(\kappa)}\,|\,\langle \Psi(0)\,|\,\tilde{\varphi}_{n_\kappa}^{(\kappa)}\tilde{\Psi}_{n_\kappa}^{(\kappa)}\rangle\,|^2\ .\end{aligned} \tag{205}$$

From this equation it is clear that the convergence of the auto-correlation function is related to the natural populations. By comparing the value of $\Delta^{(\kappa)}(t)$ for each degree of freedom, it is possible to see how complete the various sets of single-particle functions are, and where more single-particle functions are required. Experience has shown that it is important to use a balanced basis set, i.e. all the degrees of freedom are converged to the same degree.

A measure for the convergence of the calculation is then obtained by calculating the value

$$\Delta(t) = |\, \langle \Psi(0)\,|\,\Psi(t)\rangle - \langle \Psi(0)\,|\,\Psi'(t)\rangle\,|^2\,, \tag{206}$$

where $\Psi'(t)$ is the wavefunction ignoring the least populated natural orbital of all degrees of freedom. Unfortunately, due to the error accumulated during propagation, $\Delta(t)$ is not an upper bound of the error but is less than the true difference between a calculation and the related calculation made with one less single-particle function per degree of freedom. It is still however a useful function for the reason that the value of real interest is that for the addition of a single-particle function, which will be less than that for the removal of a function. In practice, it was found that when $\Delta(t)$ remains under 10^{-3}, changes to the auto-correlation function on adding an extra single-particle function to each particle are indeed negligible, and the calculation is considered as converged.

The last important check to be made is that the primitive basis set is large enough. By monitoring the expectation values of the mean and standard deviation of the one-dimensional position operators it is possible to see whether the grid is wide enough. These expectation values can be evaluated from the diagonal elements of the density operator in the DVR basis (see Sec. 4.1 for the nomenclature),

$$\rho^{(\kappa)}(Q_\alpha, Q_\alpha) = \langle \chi_\alpha^{(\kappa)}\,|\,\Psi\rangle\langle\Psi\,|\,\chi_\alpha^{(\kappa)}\rangle = \sum_{j=1}^{n_\kappa} \rho_j^{(\kappa)}\,|\,\tilde{\varphi}_j^{(\kappa)}(Q_\alpha)\,|^2\,, \tag{207}$$

from which the quantities

$$\langle Q^{(\kappa)}\rangle = \sum_{\alpha=1}^{N_\kappa} Q_\alpha \rho^{(\kappa)}(Q_\alpha, Q_\alpha) \tag{208}$$

$$\langle (Q^{(\kappa)})^2 \rangle = \sum_{\alpha=1}^{N_\kappa} Q_\alpha^2 \rho^{(\kappa)}(Q_\alpha, Q_\alpha) \tag{209}$$

$$\Delta Q^{(\kappa)} = \left(\langle (Q^{(\kappa)})^2 \rangle - \langle Q^{(\kappa)} \rangle^2 \right)^{1/2} \tag{210}$$

are derived. For a DVR basis similar expressions for the average occupation number, and spread over the occupancies, are obtained after transforming the single-particle functions to the FBR representation. This enables one to check that enough FBR functions have been included. (See App. B for a definition of the acronyms DVR and FBR). For an FFT basis, the average momentum, and the standard deviation around this average, are obtained after transformation to the momentum picture. This again provides a check on the grid parameters: the width of the grid in momentum space is related to the grid spacing in coordinate space. All these quantities, as well as the natural populations are monitored throughout the MCTDH calculation.

A more detailed analysis on the primitive basis set convergence can be made by monitoring the population of the first and last grid point as a function of time. This analysis can be made in coordinate space as well as in FBR or momentum space.

9 Selected applications

Since the first paper announcing the MCTDH method appeared in 1990 [27], over 25 papers have been published, applying the method to 15 different systems. The systems treated include photo-dissociation [28,31–34,145,146], dissociation of an absorbate on a metal surface [47–50,145], vibrational predissociation [39,145], inelastic surface scattering [51–53], bi-molecular reactive scattering [40,45,42,43,46], and photo-excitation [35–37]. Tab. 2 summarises the calculations made to date using the MCTDH method.

The majority of these studies obtain properties directly from the propagation, using the auto-correlation function. The method has also been incorporated into ways to calculate directly reaction-rate constants [42] and resonance Raman spectroscopy [146].

There are various problems that need to be addressed in order to successfully apply the MCTDH method to a system of interest:

(1) The form of the Hamiltonian.
(2) The primitive basis (DVR) to be used to describe the various degrees of freedom.
(3) The choice of single-set or multi-set representation, if more than one electronic state is included.
(4) The combination scheme to be used, i.e. whether to treat degrees of freedom using single- or multi-mode single-particle functions.
(5) The integration scheme and integrators to be used.
(6) The initial wavepacket required.
(7) The evaluation of data from the propagation to extract the quantities of interest.

In the following sections these questions will be addressed for four typical examples, highlighting the effect different choices make. The systems examined include photo-dissociation, reactive scattering, surface scattering, and the photo-excitation of a molecule with a conical intersection between the excited states.

9.1 Photo-dissociation of NOCl

The first realistic problem that was investigated with the MCTDH approach was the photo-dissociation of NOCl [28]. The NOCl system consists (for total angular momentum $J = 0$) of $f = 3$ internal degrees of freedom. In Jacobian coordinates these are the (vibrational) N–O distance r, the (dissociative) distance R between the Cl atom and the centre of mass of the N–O diatom, and

Table 2. Calculations to date using the MCTDH method. The year quoted is for the first publication. The size of the system is the number of nuclear degrees of freedom, with the number of electronic states in parenthesis

System	Type	Size	Main property calculated	Year	Ref.
Henon-Heiles	Model	2 (1)	None	1990	[27]
NOCl	Photo-dissociation	3 (1)	Absorption spectrum	1992	[28]
NO_2	Photo-dissociation	3 (1)	Absorption spectrum	1992	[31]
CH_3I	Photo-dissociation	5 (3)	Absorption spectrum	1993	[32,33]
H_2 / Metal surface	Adsorbate dissociation	2 (1)	Dissociation probability	1993	[47]
CH_3I / MgO surface	Adsorbate photo-dissociation	2 (2)	Electronic state populations	1994	[48]
CH_3I / MgO surface	Adsorbate photo-dissociation	4 (2)	Fragment angular distribution	1995	[49,145]
Cl_2Ne	Vibrational predissociation	3 (1)	State lifetimes	1995	[39,145]
ICN	Photo-dissociation	2 (2)	Absorption spectrum	1995	[34,145]
$H + H_2$	Reactive scattering	2 (1)	Reaction probability	1995	[40,109]
CH_4 / Ni surface	Adsorbate dissociation	2 (1)	Dissociation probability	1995	[50]
Pyrazine ($C_4H_4N_2$)	Photo-excitation	24 (2)	Absorption spectrum	1996	[35–38]
H_2 / LiF surface	Inelastic scattering	4 (1)	State transition probabilities	1996	[51]
N_2 / LiF surface	Inelastic scattering	5 (1)	State transition probabilities	1996	[52]
CH_3I	Photo-dissociation	4 (2)	Resonance Raman spectrum	1997	[146]
$H + H_2$	Reactive scattering	3 (1)	Thermal rate constants	1997	[42]
CH_4 / Ni surface	Inelastic scattering	10 (1)	Excitation probabilities	1998	[53]
$H + H_2$ (D_2)	Reactive scattering	3 (1)	Reaction probability	1998	[45,46]
H_2 (D_2) + OH	Reactive scattering	6 (1)	Thermal rate constants	1998	[43]

the angle θ between the two corresponding axes. This rather small application already reveals many properties of the MCTDH scheme. It can also be regarded as a typical representative of the class of photo-dissociation phenomena. We will therefore discuss this process in some detail.

A photo-dissociation process is initiated by photo-excitation of a molecule from a lower electronic state — typically the ground state — to a higher one (or several higher vibronically coupled states). In the case of NOCl this excitation takes place from the electronic ground state S_0 to the S_1 state. Assuming zero temperature, the molecule is found in the lowest vibrational state of the S_0 surface before excitation. The corresponding nuclear wavefunction can be obtained with the MCTDH method by energy relaxation, as described in Sec. 7.1. The initial wavefunction for the relaxation can in principle be arbitrary, but to achieve a fast convergence one usually approximates the energy surface around its minimum by a harmonic oscillator potential, and takes the corresponding lowest eigenstate, i.e. a simple Hartree product of Gaussians, as a starting point. During the relaxation one monitors the energy expectation value and stops when it remains constant within the desired accuracy.

Employing the Condon approximation explained in Sec. 8.3, the wavepacket is then vertically shifted from the ground to the excited electronic state. Propagating this $\Psi(0)$ in time on the excited potential energy surface, i.e. S_1 for NOCl, yields $\Psi(t)$ and the corresponding auto-correlation function $c(t)$. From this, one can extract the total absorption cross-section by using Eq. (168).

After these rather general statements we now detail, for the NOCl example, how a concrete photo-dissociation calculation can be performed within the MCTDH scheme. First, the Hamiltonian H describing the system has to be defined. We split the Hamiltonian into a kinetic and potential part, $H = T + V$. The kinetic part is the same for both relaxation and propagation. For $J = 0$ it reads

$$T = -\frac{1}{2\mu_R}\frac{\partial^2}{\partial R^2} - \frac{1}{2\mu_r}\frac{\partial^2}{\partial r^2} - \frac{1}{2I_\theta \sin\theta}\frac{\partial}{\partial\theta}\sin\theta\,\frac{\partial}{\partial\theta}\,, \tag{211}$$

where $\mu_R = (1/(m_\mathrm{N} + m_\mathrm{O}) + 1/m_\mathrm{Cl})^{-1}$ and $\mu_r = (1/m_\mathrm{N} + 1/m_\mathrm{O})^{-1}$ are the reduced masses, and $I_\theta = (1/(\mu_R\, R^2) + 1/(\mu_r\, r^2))^{-1}$ specifies the moment of inertia. As usual, the wavefunction is divided by rR in order to simplify both the kinetic energy and the volume element.

The S_0 and S_1 potential energy surfaces are taken from Refs. [147] and [110], respectively. Neither of these potentials has the required product form (64) in the coordinates chosen. These surfaces can be incorporated into an MCTDH calculation in different ways. First, one may construct an analytical expression that satisfies the product form and fit it to the potential. This was done in the original work of Manthe *et al.* [28]. A second possibility is to use the CDVR approach described in Sec. 4.3. Finally, an expansion in natural potentials (cf. Sec. 6) can be determined. The performance of these methods is discussed below.

In order to represent the Hamiltonian and the wavefunction, one has to select a DVR basis for the single-particle functions. The dissociative coordinate R was set up in a sine DVR basis with $N_R = 96$ grid points, spanning the range from 3.8 to 8.3 a.u. For the vibrational degree of freedom r a Hermite DVR employing $N_r = 24$ harmonic oscillator functions was used, with the centre chosen to be at the equilibrium geometry of the NO diatom, and the width to correspond to the vibrational frequency of NO. The angular coordinate θ was described by a Legendre DVR including $N_\theta = 60$ rotor functions. The convergence with respect to the numbers of grid points was checked according to the criterions given in Sec. 8.7. The chosen DVR basis defines the matrix representation of the Hamiltonian terms. We refer the reader to App. B for more information.

The number of grid points necessary to describe the dissociative motion can be reduced to $N_R = 36$ with no deterioration of the results by adding a complex absorbing potential (see Sec. 4.7) to the S_1 surface. The CAP we used is of the monomial form given by Eq. (80). The strength $\eta = 0.357$ a.u., the order $b = 3$, and the initial point $R_\mathrm{c} = 5.0$ a.u. were chosen according to Ref. [99] in such a way that the sum of the reflection from and the transmission through the CAP is minimised. The upper boundary of R can then be replaced by 5.6 a.u. The introduction of this CAP reduced the computation time for the propagation on the S_1 surface by about one third. (The precise result depends on the particular choices for the integrators, constraints, *etc.*) In the following we will therefore discuss only propagation calculations involving a complex absorbing potential.

To examine the influence of the various choices on CPU time, memory, and accuracy we have performed a series of calculations, the results of which are compiled in Tab. 3. The first column enumerates the calculations made. In the second column the calculation type, i.e. propagation or relaxation, is given. Column three defines the potential energy surface used. We take as a benchmark a calculation where the S_1 potential of Ref. [110] was included as a non-separable 3-dimensional function, i.e. the matrix elements $\langle \Phi_J \mid H \mid \Phi_L \rangle$ and mean-fields $\langle H_\mathrm{R} \rangle_{jl}^{(\kappa)} = \langle \Psi_j^{(\kappa)} \,|\, H_\mathrm{R} \,|\, \Psi_l^{(\kappa)} \rangle$ were determined by f-fold and $(f-1)$-fold integrations, respectively ("3D function"). This calculation is compared with an expansion in natural potentials with expansion orders $m_R = m_r = 15$, i.e. $15 \times 15 = 225$ terms ("nat. pot. I"), a natural potential expansion with $m_R = 5$ and $m_r = 4$ ("nat. pot. II"), the above-mentioned fit of Manthe *et al.* ("prod. fit"), and the CDVR method. (For the natural potential expansions (see Sec. 6), we contracted over the θ-mode, and used the relevant region iteration scheme.) The integrator column specifies whether the standard method of Sec. 2.2 ("exact"), the VMF (Sec. 5.1), or the CMF (Sec. 5.2) integration

Table 3
Comparison of computational resources needed for propagating the wavefunction of the photo-dissociation process of NOCl. The first column enumerates the calculations made. The second column selects between relaxation and propagation calculations. In the third column the potential energy surface is specified. Columns four and five define the integration scheme and the constraint used. The next two columns give the CPU time and memory required. Finally, "Error" is the maximum of the error $\| \Psi(t) - \tilde{\Psi}(t) \|$ of the wavefunction Ψ with respect to a reference $\tilde{\Psi}$.

Run	Type	PES	Integrator	g	CPU [s]	Memory [MB]	Error
1	prop.	3D function	VMF	h	857	3.9	—
2	prop.	nat. pot. I	VMF	h	1159	2.8	0.0015
3	prop.	nat. pot. II	VMF	h	166	1.3	0.057
4	prop.	prod. fit	VMF	h	191	1.3	0.54
5	prop.	CDVR	VMF	h	329	1.2	0.0046
6	prop.	prod. fit	exact	—	2120	19.5	—
7	prop.	prod. fit	VMF	0	173	1.3	0.046
8	prop.	prod. fit	VMF	h	191	1.3	0.046
9	prop.	prod. fit	CMF	0	59	1.3	0.046
10	prop.	prod. fit	CMF	h	104	1.3	0.046
11	relax.	prod. fit	exact	—	1883	20.3	—
12	relax.	prod. fit	VMF	0	57	1.1	0.00044
13	relax.	prod. fit	CMF	0	60	1.1	0.00044

scheme was used. The next column displays the constraints employed, namely $g^{(\kappa)} = 0$ or $g^{(\kappa)} = h^{(\kappa)}$ (cf. Sec. 3.2). The next two columns present the CPU time and memory required. Finally, the error, which is defined as the maximum of $\| \Psi(t) - \tilde{\Psi}(t) \|$ during the propagation (see Eq. (159)), is given. Here $\tilde{\Psi}$ is a reference wavefunction, obtained in run 1, 6, and 11, respectively. Note that an error of 0.01, for instance, is equivalent to an overlap $\mathrm{Re}\,\langle \Psi(t) \,|\, \tilde{\Psi}(t) \rangle$ of 0.99995.

We used for each degree of freedom $n = 3$ single-particle functions in the relaxation and $n = 5$ in the propagation calculations. The single-particle functions were represented as standard orbitals (Sec. 3.1). The time interval was 60 fs for the relaxation and 25 fs for the propagation calculations. Note that according to Eq. (167) the auto-correlation function is then known up to twice the final propagation time. All runs have been performed on a 120 MHz Intel Pentium PC running under Linux.

With runs 1 to 5 we want to judge the quality of the possible ways of including the S_1 surface in an MCTDH propagation. The reference calculation, run 1, where the potential matrix elements and mean-fields were determined by multi-dimensional integration, is rather slow and requires about one third of the CPU time of the numerically exact calculation, run 6. This underlines the importance of representing the potential in product form. Run 2 shows that the natural potential expansion is able to represent the potential very accurately, however at the price that many expansion terms are needed, which slows down the calculation. Note that the accuracy of this potential representation is much higher than necessary for determining observable quantities, such as absorption spectra. Due to the smallness of the system, including the potential as a 3-dimensional function is faster than the high-accuracy natural potential expansion. For larger systems, however, this will not be the case.

Calculations more typical for MCTDH applications are given in runs 3 to 5. In runs 3 and 4 the potential energy was approximated by natural potentials and the fit of Manthe *et al.*, respectively. Note that the number of non-separable potential terms of the natural potential expansion is 20, and thus the same as in the fit. The natural potential expansion is noticeable faster and at the same time considerably more precise than the fit done “by hand”. The higher accuracy of the natural potentials is not surprising as they are optimal in a weighted $\mathcal{L}^2$-sense. The error of the product fit, i.e. the norm of the difference between the wavefunctions of runs 1 and 4, is rather large. The spectra computed from these wavefunctions, however, agree reasonably well, because the auto-correlation function from which the spectra are generated is insensitive to errors in the wavefunction that are orthogonal to $\Psi(0)$.

In the particular case of NOCl the CDVR approach gives remarkably precise results, though at the price of a CPU time two times larger than with natural potentials. Unfortunately, we have found that this high accuracy of CDVR is generally not reached for other systems. (See also our comment on CDVR at the end of Sec. 4.3.) The memory requirements were very similar for the three methods.

Calculations 6 to 10 compare both the available integration schemes and the influence of the constraints. The error tolerances of the VMF and CMF integrators were chosen such that the integrator errors were small compared with the MCTDH error, i.e. the convergence with respect to the single-particle functions. The most efficient MCTDH calculation, run 9, is 36 times faster, and needs 15 times less memory than the standard method. When employing the constraint $g^{(\kappa)} = 0$ the CMF scheme is about three times faster than the VMF scheme. This is a comparatively small gain, but this was to be expected for such a small system (In the VMF run, only 36% of the CPU time results from the computation of the mean-fields). In all MCTDH calculations the same amount of memory was necessary.

It is illuminating to compare the measured gain of the CMF scheme with respect to the standard method with the predicted gain of Eq. (92). Using the parameters given above, as well as an effective $s = 23$ (see the discussion below Eq. (92)), and $\bar{l} = 5$, one obtains a gain of 111. However, NOCl is a small system and the effort of propagating the single-particle functions is not negligible, as assumed when deriving Eq. (92), but amounts to 73% of the total effort. Thus the predicted gain must be multiplied with 0.27, yielding a gain of 30. This value is in fact close to the measured one of 36, demonstrating the reliability of Eq. (92).

We want to point out that it was necessary to cut large potential energy values when using the standard method. This is because the potential fit of Manthe *et al.* shows large *negative* values in an unphysical region, which force the integrator of the standard method to take small steps. Due to this, a large gain factor of 150 was reported in an earlier publication [28]. The MCTDH algorithm, on the other hand, is less sensitive to large potential energy values. Cutting the potential thus speeds up the exact calculation and lets the gain factor drop to the value presented here.

The influence of the constraints $g^{(\kappa)} = 0$ and $g^{(\kappa)} = h^{(\kappa)}$ in a VMF run is demonstrated in runs 7 and 8. While generally it is advantageous to set $g^{(\kappa)} = h^{(\kappa)}$, since then only the residual Hamiltonian (42) is involved in the propagation of the MCTDH coefficients, this is not the case for the NOCl system. The reasons are that the A-vector is short ($n^f = 125$), and that there are merely 4 out of 26 Hamiltonian terms that are separable. On the other hand, using the constraint $g^{(\kappa)} = h^{(\kappa)}$ causes the single-particle functions to change more rapidly, which enforces smaller integration steps. For NOCl the latter effect dominates. In the CMF scheme, this effect is typically much more dramatic, as can be seen from runs 9 and 10. Therefore, the constraint $g^{(\kappa)} = 0$ is generally used when the CMF scheme is applied.

Our last study concerns the influence of the different integration schemes in a relaxation calculation, runs 11 to 13. A numerically exact calculation using the standard method needs more than 30 times more CPU time, and almost 20 times more memory than an MCTDH calculation. Comparing the VMF and CMF schemes, one finds that a VMF run is slightly faster. This surprising outcome is due to the smallness of the system. Since merely $n^f = 27$ configurations are involved, almost all computational effort is spent for the propagation of the single-particle functions. The error estimate of the CMF scheme, which requires the single-particle functions to be propagated one and a half times, then negates all other savings. For larger systems, however, the CMF method performs very well in relaxation calculations, as the wavefunction soon becomes nearly converged, allowing the mean-fields to be kept constant for rather long time steps. Reference [54] gives an example.

The above calculations demonstrate that even for small systems the use of the MCTDH scheme can lead to a considerable reduction of the computational resources compared with the standard method of Sec. 2.2. The results also show that the natural potential expansion offers a convenient, efficient and accurate way to incorporate the NOCl potential energy surface into an MCTDH calculation. Finally, for the example under consideration the CMF algorithm turns out to be advantageous to the VMF integrator, even though the system is small.

9.2 Reactive scattering of $H+D_2$

The $H+H_2$ reaction and its isotopic variants are probably the elementary reactions most extensively studied during the last decade. They are thus often considered as typical examples of elementary bimolecular reactions, by experimentalists as well as by theoreticians [148,149]. From the theoretical point of view, the resolution of this scattering problem is not as trivial as the small size of the system might suggest. Even thermal rate constants, which are averaged quantities, have been shown to be highly dependent on the accuracy of both the electronic potential energy surface and the method of nuclear dynamics used for the calculation [150–152].

Turning to MCTDH it should be noted that H_3 is a rather small system. It consists of light atoms, and is defined by only three (internal) coordinates. On the other hand — like any reactive system — its motion is highly correlated as the products are represented in the Jacobian coordinates of the reactants. Additionally, the complicated potential energy surface has to be represented in product form, requiring many expansion terms.

Hence, $H+H_2$ reactive scattering is a problem not particularly suitable for MCTDH. Being a small system, N and f are small, but being highly correlated, n is comparatively large. In addition to that, there is a rather large number, s, of Hamiltonian terms. (Compare with Secs. 4.4 and 5.2.6). However, as shown below, the $H+H_2$ reactive scattering system has been successfully treated by MCTDH. It is thus to be expected that MCTDH will perform very efficiently when turning to larger reactive scattering systems, e.g. four atom systems.

In order to profit at least a little from the favourable MCTDH scaling, we shall concentrate in the following on the isotopic variant $H+D_2$ and consider translational energies up to the rather large value of 2.5 eV, computing cumulative initial-state selected cross-sections for the $H+D_2(\nu, j) \to HD+D$ reaction [46]. To compare with experimental results [153–155], these cross-sections are thermally averaged over a room-temperature Boltzmann distribution of the D_2 rotational states. The D_2 molecule is taken to be in the vibrational ground or first excited state. To our knowledge, these are the first calculations on vibrationally excited, $\nu=1$, D_2 target molecules.

Denoting the D–D bond distance by r, the distance from the H atom to the centre-of-mass of the D_2-molecule by R, and the angle between these axes by θ, the total Hamiltonian in the body-fixed frame within the coupled states approximation can be written as [64,65,156]

$$H^{JK}(R,r,\theta) = T_R + T_r + T_\theta + V_{\mathrm{LSTH}}(R,r,\theta) + \frac{J(J+1) - 2K^2}{2\mu_R R^2}\,, \tag{212}$$

where

$$T_R = -\frac{1}{2\mu_R}\frac{\partial^2}{\partial R^2}\,, \tag{213}$$

$$T_r = -\frac{1}{2\mu_r}\frac{\partial^2}{\partial r^2}\,, \tag{214}$$

$$T_\theta = \left(\frac{1}{2\mu_R R^2} + \frac{1}{2\mu_r r^2}\right)\hat{\jmath}^2\,, \tag{215}$$

and

$$\hat{\jmath}^2 = -\left(\frac{1}{\sin\theta}\frac{\partial}{\partial\theta}\sin\theta\frac{\partial}{\partial\theta} - \frac{K^2}{\sin^2\theta}\right)\,. \tag{216}$$

Here μ_R denotes the reduced mass of the H atom and the D_2-diatom, and μ_r the reduced mass of the two D atoms. Within the coupled states approximation not only the total angular momentum quantum number J, but also the quantum number K denoting the projection of the total angular momentum onto the body-fixed axis $\boldsymbol{R}$ are conserved, i.e. remain unchanged during the reaction process. V_{LSTH} denotes the Liu-Siegbahn-Truhlar-Horowitz (LSTH) potential energy surface for the H_3 system in its lowest electronic state [111–113].

For an efficient implementation of the MCTDH algorithm, it is necessary for the system's Hamiltonian to be in a product form (see Sec. 4.2). On inspection of Eqs. (212) to (216) this is the case for the kinetic energy and centrifugal potential terms. The LSTH potential energy surface, $V_{\mathrm{LSTH}}(R,r,\theta)$, can be expanded in a product basis employing the product representation scheme discussed in Sec. 6. Instead of expanding the entire LSTH surface the interaction potential

$$\begin{aligned} V_{\mathrm{I}}^{JK}(R,r,\theta) &= V_{\mathrm{I}}(R,r,\theta) + \frac{J(J+1) - 2K^2}{2\mu_R R^2} \\ &\approx \sum_{i=1}^{m_r}\sum_{j=1}^{m_\theta} D_{ij}(R)\, v_i^{(r)}(r)\, v_j^{(\theta)}(\theta) \end{aligned} \tag{217}$$

was expanded in a product basis of natural potentials. The first term on the right hand side of Eq. (217) is defined as the difference between the LSTH-potential V_{LSTH} and the potential V_{D_2} of the free diatom D_2,

$$V_{\mathrm{I}}(R, r, \theta) = V_{\mathrm{LSTH}}(R, r, \theta) - V_{\mathrm{D}_2}(r)\,, \tag{218}$$

which vanishes for sufficiently large values of the translational coordinate R.

In order to avoid a decrease in integrator step size due to high potential values, an energy cut-off has been applied to the potential V_{I}^{JK} before it was expanded. This is the reason why the centrifugal term is included in the expansion. To reduce the number of expansion coefficients, a contraction over the translational degree of freedom R proved to be the most advantageous (see Eq. (121)). For the definition of the relevant regions the reader is referred to Ref. [57].

The interaction potential V_{I}^{JK} (Eq. (217)) was expanded for each set of quantum numbers (J, K). The expansion orders were taken as $m_r = 12$ and $m_\theta = 9$, resulting in 108 expansion coefficients. The computational effort for the determination of the product expansion was negligible: it took less than 2 min on an IBM RS/6000 power2 workstation to compute one expansion.

The initial wavepacket $\Psi_0 = \Psi(t = 0)$ is defined as the product of a Gaussian wavepacket χ_0 (Eq. (153)), a vibrational eigenfunction $\varphi_{j_0\nu_0}$ (Eq. (220)), and a $\mathcal{L}^2$-normalised associated Legendre polynomial $\tilde{P}_{j_0}^{K}$ (Eq. (222)),

$$\Psi_0(R, r, \theta) = \chi_0(R)\,\varphi_{j_0\nu_0}(r)\,\tilde{P}_{j_0}^{K}(\cos\theta)\,. \tag{219}$$

The vibrational functions are defined as the eigenfunctions,

$$H_{0,j}(r)\,\varphi_{j\nu}(r) = E_{j\nu}\,\varphi_{j\nu}(r)\,, \tag{220}$$

of the internal channel Hamiltonian corresponding to the rotational quantum number j,

$$H_{0,j}(r) = T_r + V_{\mathrm{D}_2}(r) + \frac{j(j+1)}{2\mu_r r^2}\,. \tag{221}$$

The $\mathcal{L}^2$-normalised associated Legendre polynomials

$$\tilde{P}_j^{K}(\cos\theta) = \sqrt{\frac{2j+1}{2}\frac{(j-K)!}{(j+K)!}}\,P_j^{K}(\cos\theta) \tag{222}$$

are eigenfunctions of the $\hat{\jmath}^2$-operator (see Eq. (216)) with eigenvalues $j(j+1)$.

The initial wavepacket, Ψ_0, (if uncorrected) must be located in the asymptotic region of the reactant channel,

$$\left(V_{\mathrm{I}}(R,r,\theta) + \frac{j(j+1)}{2\mu_R R^2} + \frac{J(J+1) - 2K^2}{2\mu_R R^2}\right) \Psi_0(R,r,\theta) \approx 0\,. \tag{223}$$

This equation can always be satisfied by choosing the centre of the wavepacket, R_0, large enough. However, inspection of Eq. (223) shows that the higher the total rotational quantum number J, the slower the centrifugal potential falls off, and the further away from the scattering centre the initial wavepacket has to be placed. This results in larger grid sizes and longer propagation times. For example, for total angular momentum quantum number $J_{\max} = 40$, and vanishing quantum number $K = 0$, the centrifugal potential at the outer edge of the translational grid, $R_{\max} = 10$ a.u., takes on considerable values:

$$\frac{J_{\max}(J_{\max}+1)}{2\mu_R R_{\max}^2} \approx 0.15\,\mathrm{eV}\,. \tag{224}$$

Instead of placing the initial wavepacket Ψ_0 far out in the asymptotic region of the educt channel, the adiabatic correction scheme was employed, which allows the initial wavepacket to be moved close to the scattering centre. The adiabatic correction follows the lines presented in Sec. 7.2, but only the vibrational state was corrected adiabatically; the rotational state was treated diabatically [46]. This is reasonable because the rotational motion is slow compared with the translational one.

Initial momentum $p_0 = -8.76$ (-7.00) a.u. and width $\sigma_R = 0.18$ a.u. of the Gaussian wavepacket χ_0 (Eq. (153)) were chosen in accordance with the desired initial energy distribution $\Delta(E)$ (Eq. (157)). The value in brackets corresponds to vibrationally excited H+D$_2(\nu = 1)$ calculations. The initial wavepackets were placed quite close to the interaction region: the centre of the wavepacket was placed at $R_0 = 4.5$ a.u. for the D$_2$-molecule in its vibrational ground state, which for the vibrationally excited D$_2$ had to be moved to $R_0 = 5.5$ a.u. to account for the larger spatial extension of the $\varphi_{j_0\nu=1}$ vibrational eigenfunction compared with the spatial extension of the ground-state $\varphi_{j_0\nu=0}$ eigenfunction.

Without the adiabatic correction scheme it would have been necessary to locate the initial wavepacket much further away from the scattering centre. For vanishing total angular momentum $J = 0$, and initial $j = 0, \nu = 0$, a value of $R_0 = 7.5$ a.u. was found to be necessary [45].

For each set of quantum numbers (ν_0, j_0, J, K), the adiabatically corrected initial wavepacket is provided in an MCTDH-compatible product basis of appropriately chosen single-particle functions,

$$\Psi_0(R,r,\theta) = \sum_{k=0}^{n_R-1} \sum_{\nu=0}^{n_r-1} A_{k\nu j_0}\, \chi_k(R)\, \varphi_{j_0\nu}(r)\, \tilde{P}_{j_0}^{K}(\cos\theta)\,. \tag{225}$$

The single-particle functions of the dissociative degree of freedom $\chi_k(R)$ are defined according to Eq. (154), Schmidt-orthonormalised, and are orthogonal to the Gaussian wavepacket χ_0 (Eq. (153)). The $\varphi_{j_0\nu}$ are vibrational eigenfunctions of the internal channel Hamiltonian H_{0,j_0} (Eq. (221)), corresponding to the initial rotational quantum number j_0. The vibrational eigenfunctions $\varphi_{j_0\nu}$ for fixed rotational quantum number j_0 were determined by diagonalisation of the diabatic channel Hamiltonian (Eq. (221)) represented by sine DVR (cf. App. B.4.4).

The single-particle functions of the dissociative and of the vibrational degree of freedom were represented on an equidistant grid by sine DVR. The single-particle functions of the rotational degree of freedom were represented by *symmetrised Legendre DVR*, exploiting the underlying potential symmetry due to the homonuclear diatom. Employing symmetrised Legendre DVR the number of grid points is halved (see App. B.4.3 for more details). The numbers of single-particle functions used were $n_R = 16$ (18), $n_r = 12$ (14), and $n_\theta = 12$. Values in brackets correspond to vibrationally excited H+D$_2$($\nu = 1$) calculations.

The wavepackets were propagated using the constant mean-field integration scheme (see Sec. 5.2). The use of the constant mean-field integrator reduced the computational effort by about an order of magnitude compared with the variable mean-field integration scheme (see Sec. 5.1). This was accomplished without a deterioration of the accuracy, and with stable self-regulation of the integrator step size.

Initial-state selected reaction probabilities, $P_{\nu j}^{JK}(E)$, were determined for a broad energy range by analysing the reactive flux into the configuration channel of the products. To this end the combined flux operator/complex absorbing potential approach of Sec. 8.6 was employed.

The complex absorbing potential $-iW$ was defined as a sum of two one-dimensional potentials of monomial form given by Eq. (80):

$$W(R,r) = W_R(R) + W_r(r)\,. \tag{226}$$

The strength parameters $\eta_R = \eta_r = 0.003$ a.u., the starting points $R_\mathrm{c} = 6.04$ (7.00) a.u. and $r_\mathrm{c} = 3.24$ a.u., and the orders $b_R = b_r = 3$ were chosen according to the rules given in Ref. [99]. Again, the value in brackets corresponds to the vibrationally excited H+D$_2$($\nu = 1$) calculation.

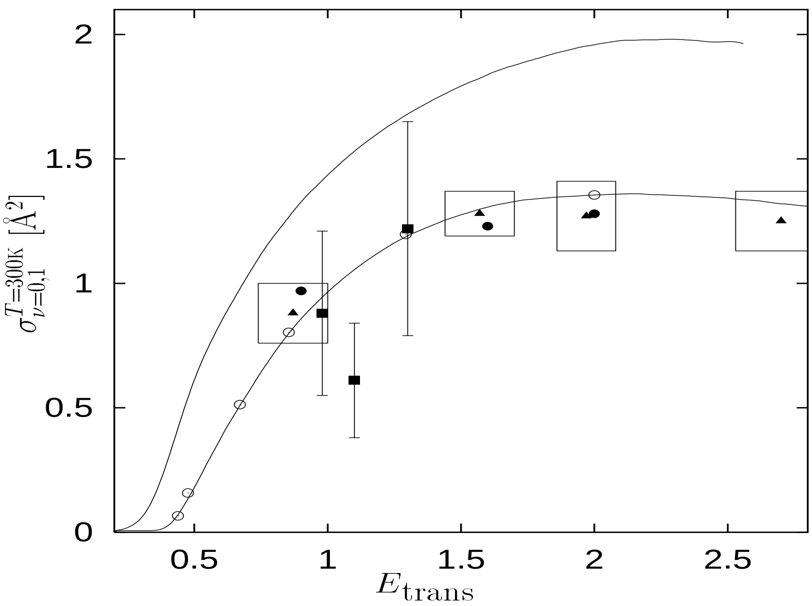

Fig. 3. Comparison of experimental and theoretical reaction cross-sections as a function of the translational energy for the H+D$_2$($\nu = 0$) and H+D$_2$($\nu = 1$) reaction. The cross-sections are rotationally Boltzmann averaged for $T = 300$ K. The solid lines show the results of MCTDH calculations [46]. The lower curve represents the $\nu = 0$ and the upper curve the $\nu = 1$ cross-sections. Experimental cross-sections of Brownsword *et al.* [155], Levene *et al.* [154], and Johnston *et al.* [153] are depicted by filled circles, squares, and triangles, respectively. The error-boxes and the error-bars show the errors as given by Johnston *et al.* and Levene *et al.*, respectively. The errors of the Brownsword *et al.* cross-sections are comparable to those of Johnston *et al.* For reasons of clarity they are not shown. The results of rotationally averaged coupled states calculations employing a recently developed Toeplitz approach of Charutz *et al.* [157] are represented by open circles. The Charutz values are taken from Fig. 9 of Ref. [157]. This figure has been reprinted from Ref. [46].

The initial-state selected reaction probabilities are related to the interaction of the time evolved wavepacket $\Psi(t)$ with the product arrangement channel CAP W_r. The energy distribution $\Delta(E)$ of the initial wavepacket determines the energy range for which the reaction probabilities can be computed in one step by a single propagation. To obtain room temperature rotationally-averaged reaction cross-sections $\sigma^{T=300\mathrm{K}}_{\nu=0,1}(E)$ for translational energies up to 2.5 eV, wavepacket propagations are performed with initial quantum numbers up to $j_{\max} = 4$ and $J_{\max} = 40$. As K takes values from 0 to j, 600 separate wavepacket propagations had to be performed for each initial vibrational state.

Figure 3 shows the results of MCTDH calculations [46], and compares these with experimental [153–155] and theoretical [157] values determined by other groups. Depicted are rotationally averaged ($T = 300$ K) reaction cross-sections for the H+D$_2$($\nu = 0$) and H+D$_2$($\nu = 1$) reaction as a function of the relative translational energy. The solid lines show the results of the MCTDH calculations. The lower curve represents the $\nu = 0$, and the upper curve the $\nu = 1$ cross-sections.

For $\nu = 0$, the MCTDH results are compared with the theoretical values (open circles) of Charutz *et al.* [157]. The Charutz values are results of rotationally averaged coupled states calculations employing a Toeplitz operator approach. Charutz *et al.* computed reaction cross-sections for six energy values, and the MCTDH results are in excellent agreement with these data. The experimental $\nu = 0$ values of Brownsword *et al.* [155], Levene *et al.* [154], and Johnston *et al.* [153] are also depicted. Within the experimental errors there is excellent agreement between the MCTDH values and the experimental measurements.

Computational speed is of importance, since 600 independent wavepacket propagations have to be performed for a given initial vibrational state. Each single calculation is specified by a set of initial quantum numbers (ν, j, J, K). Total angular momentum values up to $J_{\text{max}} = 40$ were necessary to obtain converged results in the energy range under investigation. The computational cost for a single calculation on a 400 MHz Dec-alpha workstation varies between 60 and 90 minutes CPU time, depending on the initial quantum numbers. This is fast but the CPU times are comparable with those of other optimised wavepacket propagation methods. If one takes into account that H+D_2 is a small but strongly coupled system, this fact is very encouraging. When turning to larger systems we therefore expect MCTDH to perform considerably faster than standard wavepacket propagation. Note that the MCTDH memory requirements are always low. The present calculations need only 5 MB RAM.

9.3 Surface scattering of N_2/LiF(001)

Several molecule-surface scattering problems have been studied using the MCTDH method [47–53]. Here we consider the scattering of a diatom from a corrugated rigid surface. The three Cartesian coordinates (x, y, z) define the position of the centre of mass of the molecule with the z-axis being perpendicular to the surface. The orientation of the diatom is described by the polar and azimuthal angles (θ, ϕ) with respect to the z-axis. Treating the molecule as a rigid-rotor there are thus five degrees of freedom. The Hamiltonian reads

$$H = -\frac{1}{2M}\left(\frac{\partial^2}{\partial x^2} + \frac{\partial^2}{\partial y^2} + \frac{\partial^2}{\partial z^2}\right) + H_{\text{rot}}(\theta, \phi) + V(x, y, z, \theta, \phi)\,, \tag{227}$$

where

$$H_{\text{rot}} = -\frac{1}{2\mu r^2}\left[\frac{1}{\sin\theta}\frac{\partial}{\partial\theta}\sin\theta\frac{\partial}{\partial\theta} + \frac{1}{\sin^2\theta}\frac{\partial^2}{\partial\phi^2}\right] \tag{228}$$

denotes the operator of rotational energy and where M and μ are the total and reduced mass of the diatom, respectively.

The molecule-surface interaction potential is the surface-dumbbell model [158]

$$\begin{aligned} V(x,y,z,\theta,\phi) = 2A\exp(-\alpha z)\Big[&\cosh\left(\tfrac{\alpha r}{2}\cos\theta\right) \\ &+\beta\cosh\left(\tfrac{\alpha r}{2}\cos\theta\right)\Big\{\cos\left(\tfrac{2\pi x}{a}\right)\cos\left(\tfrac{\pi r}{a}\sin\theta\cos\phi\right) \\ &\qquad+\cos\left(\tfrac{2\pi y}{b}\right)\cos\left(\tfrac{\pi r}{b}\sin\theta\sin\phi\right)\Big\} \\ &+\beta\sinh\left(\tfrac{\alpha r}{2}\cos\theta\right)\Big\{\sin\left(\tfrac{2\pi x}{a}\right)\sin\left(\tfrac{\pi r}{a}\sin\theta\cos\phi\right) \\ &\qquad+\sin\left(\tfrac{2\pi y}{b}\right)\sin\left(\tfrac{\pi r}{b}\sin\theta\sin\phi\right)\Big\}\Big]. \end{aligned} \tag{229}$$

The potential parameters can be chosen to model the N_2/LiF(001) interaction by taking the potential range, corrugation, internuclear distance of the rigid rotor, and lattice constants as $\alpha = 1.9012$ a.u., $\beta = 0.1$, $r = 2.0673$ a.u., and $a = b = 5.3669$ a.u., respectively. The potential strength parameter A is arbitrary as it merely shifts the potential along the z-axis. Note that this model potential satisfies the MCTDH product form requirement, Eq. (64).

The angular degrees of freedom θ and ϕ are strongly coupled through the term $\sin^{-2}\theta\, \partial^2/\partial\phi^2$ which appears in $H_{\rm rot}$. This coupling, in fact, becomes singular for $\theta \to 0$ or $\theta \to \pi$. It thus causes numerical problems and slows down the convergence when treated as separable. The singularity is removed by combining the two angular degrees of freedom (see Sec. 4.5) and representing the resulting two-mode single-particle functions by spherical harmonics $Y_{jm_j}(\theta,\phi)$. In this primitive basis $H_{\rm rot}$ is diagonal with diagonal elements $j(j+1)/2\mu r^2$.

The z-degree of freedom describes the distance from the surface and requires rather many grid points. It is thus convenient to represent it by FFT. The motion parallel to the surface needs to be represented only over one lattice constant because of the periodicity of the interaction. Periodic boundary conditions are then required and FFT is thus the obvious choice for representing the x and y degrees of freedom. Since these degrees of freedom require a comparatively small number of grid points, it is of advantage to combine them and treat them as one particle (see Sec. 4.5 and 9.4). The five-dimensional problem is thus treated as a three particle one, two of the particles being two-dimensional.

The N_2/LiF(001) surface scattering problem has been investigated by the MCTDH scheme [52], and by other methods [159,160], for scattering energies up to 100 meV. We recently returned to this problem and studied it over an extended energy range of 60 to 300 meV [107]. The recent technical advances, such as the correction scheme (see Sec. 7.2.2) and the use of CAPs (see Sec. 4.7) combined with the flux analysis (see Sec. 8.6), allowed the z-grid length to be shortened by roughly a factor of three. However, because of the higher energy the grid spacings must now be finer, making the problem much larger than the one studied previously [52,159,160]. A converged calculation requires $(N_x, N_y, N_z, N_{\theta\phi}) = (24{,}24{,}108{,}223)$ grid points or primitive basis functions ($j_{\max} = 36$, $m_{j,\max} = 6$, and taking only even j's leads to 223 spherical harmonics as basis functions). The numbers of single-particle functions required are $(n_{xy}, n_z, n_{\theta\phi}) = (35{,}17{,}70)$. A single wavefunction represented in the primitive basis needs 210 MB storage, making the standard method (see Sec. 2.2) very difficult, if not infeasible, for this problem. A MCTDH wavefunction, on the other hand, requires merely 1.2 MB and the MCTDH calculation takes about 15 MB, being feasible even on small computers.

For a large system like the present one with several ten thousand open states, it is no longer useful to investigate state-to-state transition probabilities. Averaged quantities like the *average rotational energy transfer* (ARET) or the *average parallel energy transfer* (APET) are often more meaningful. The flux analysis method is very well suited for the calculation of averaged quantities. The totally averaged rotational energy transfer is e.g. given by

$$\mathrm{ARET}(E) = \frac{2}{\pi\,|\,\Delta(E)\,|^2}\,\mathrm{Re}\int_0^\infty g_{\mathrm{rot}}(\tau)\, e^{iE\tau}\, d\tau\,, \tag{230}$$

where the correlation function g_{rot} is defined as

$$g_{\mathrm{rot}}(\tau) = \int_0^\infty dt\, \langle \Psi(t)\,|\, H_{\mathrm{rot}} W \,|\, \Psi(t+\tau)\rangle \tag{231}$$

(compare with Eqs. (198) to (201)). Note that the CAP W depends on z alone and thus commutes with H_{rot}.

The diffraction channel-specific ARET is defined similarly by replacing g_{rot} with $g_{nm,\mathrm{rot}}$ where

$$g_{nm,\mathrm{rot}}(\tau) = \int_0^\infty dt\, \langle \Psi(t)\,|\, P_{nm} H_{\mathrm{rot}} W \,|\, \Psi(t+\tau)\rangle\,. \tag{232}$$

Here $P_{nm} = |nm\rangle\langle nm|$ is the projector on the nmth diffraction channel and

$$\langle xy\,|\,nm\rangle = (ab)^{-1/2} \exp(2\pi i n x/a + 2\pi i m y/b) \tag{233}$$

is the nmth eigenfunction of parallel motion (normal incidence is assumed). Note that P_{nm}, H_{rot} and W mutually commute. The APET is defined analogously by exchanging H_{rot} with the expression for the parallel energy and P_{nm} with the projector on a specific rotational state P_{jm_j}. Finally, if H_{rot} is removed from Eq. (232) such that only $P_{nm}W$ (or alternatively $P_{jm_j}W$) remains, one computes the rotationally averaged transition probability to the nmth diffraction channel (or the diffraction channel averaged transition probability to the jm_j rotational state). The use of the operator $P_{nm}P_{jm_j}W$ eventually provides state-to-state transition probabilities.

The totally averaged ARET shows a very simple course: $\mathrm{ARET}(E) = 0.095E$. Thus 9.5% of the initial kinetic energy is transferred to rotational energy, almost independently of the kinetic energy. This finding is for the initial rotational state $j = 0$ and normal incidence. The diffraction channel averaged transition probability to final rotational states depicts a strong rotational rainbow structure in particular for $j_{final} \geq 10$ and $E \geq 100$ meV. More details on results may be found in [52,159] and in a forthcoming publication [107].

9.4 Photo-excitation of pyrazine

The photo-excitation of the pyrazine molecule ($C_4H_4N_2$) has been extensively investigated, both experimentally and theoretically. The UV-absorption spectrum [161,162] shows two bands close in energy. The most important feature is that while the lower energy, S_1, band shows a set of discrete lines, the upper, S_2, band is broad with very little structure. This lack of structure is attributed to a conical intersection between the two states, resulting in a fast radiationless transition from the upper to lower state.

For such a set of vibronically coupled states, a model Hamiltonian has been developed [163]. The excited states are taken in a diabatic representation, and the Hamiltonian thus has a matrix form where the matrix indices refer to the diabatic states. The diabatic potential energy surfaces, expressed in the ground-state normal modes, are expanded in a Taylor series around the ground-state equilibrium position:

$$\boldsymbol{H} = \boldsymbol{H}_0 + \boldsymbol{H}_1 + \boldsymbol{H}_2 + \dots \ . \tag{234}$$

The zeroth order expansion term is the ground-state potential energy surface and a term for the energy splitting between the states,

$$\boldsymbol{H}_0 = \sum_i \frac{\omega_i}{2}\left(-\frac{\partial^2}{\partial Q_i^2} + Q_i^2\right)\begin{pmatrix} 1 & 0 \\ 0 & 1 \end{pmatrix} + \begin{pmatrix} -\Delta & 0 \\ 0 & \Delta \end{pmatrix} , \tag{235}$$

where ω_i is the frequency of the ith normal mode with dimensionless coordinate Q_i. The splitting between the two potential energy surfaces at the equilibrium position, $\boldsymbol{Q} = 0$, is 2Δ.

The first order terms are then linear in the normal mode coordinates, while the second order terms are quadratic and bi-linear,

$$\boldsymbol{H}_1 = \sum_{i \in G_1} \begin{pmatrix} \kappa_i^{(1)} & 0 \\ 0 & \kappa_i^{(2)} \end{pmatrix} Q_i + \sum_{i \in G_3} \begin{pmatrix} 0 & \lambda_i \\ \lambda_i & 0 \end{pmatrix} Q_i \,, \tag{236}$$

$$\boldsymbol{H}_2 = \sum_{(i,j) \in G_2} \begin{pmatrix} a_{ij} & 0 \\ 0 & b_{ij} \end{pmatrix} Q_i Q_j + \sum_{(i,j) \in G_4} \begin{pmatrix} 0 & c_{ij} \\ c_{ij} & 0 \end{pmatrix} Q_i Q_j \,. \tag{237}$$

Here, symmetry considerations play a major role. The pyrazine molecule has the point group $\mathrm{D_{2h}}$, and the $\mathrm{S_1}$ and $\mathrm{S_2}$ states have symmetry $\mathrm{B_{3u}}$ and $\mathrm{B_{2u}}$ respectively. The first order off-diagonal coupling elements are thus non-zero only for modes with $\mathrm{B_{1g}}$ symmetry, and the set G_3 contains only the $\nu_{10\mathrm{a}}$ mode. The linear on-diagonal coupling elements are non-zero for vibrational modes which are totally symmetric, and the set G_1 contains the five $\mathrm{A_g}$ modes: $\nu_{6\mathrm{a}}$, ν_1, $\nu_{9\mathrm{a}}$, $\nu_{8\mathrm{a}}$, and ν_2. The non-zero second order coupling elements are governed by the symmetry of products of modes. The set G_4 comprises products of modes with resulting $\mathrm{B_{1g}}$ symmetry, while the set G_2 products with $\mathrm{A_g}$ symmetry. For more details see Ref. [37].

Previous theoretical studies have shown [164,165] that the experimental spectrum can be qualitatively reproduced when the Hamiltonian is expanded to first order, i.e. only coupling matrix elements linear in the normal mode coordinates are included. Thus only the modes in sets G_1 and G_3 are relevant. Ignoring two totally symmetric modes which have very weak coupling constants leads to a 4-mode model with the modes $\nu_{10\mathrm{a}}, \nu_{6\mathrm{a}}, \nu_1$, and $\nu_{9\mathrm{a}}$. A phenomenological broadening of the spectrum from this model is then used to account for the remaining 20 modes.

It thus seems reasonable to turn the problem into a system-bath interaction study, and replace these 20 modes by a heat bath [166]. A simple form for a bath is a set of harmonic oscillators coupled linearly to the electronic states, i.e.

$$\boldsymbol{H}_{\mathrm{bath}} = \sum_{b=1}^{n_{\mathrm{bath}}} \frac{\omega_b}{2} \left(-\frac{\partial^2}{\partial Q_b^2} + Q_b^2 \right) \begin{pmatrix} 1 & 0 \\ 0 & 1 \end{pmatrix} + \begin{pmatrix} \kappa_b^{(1)} & 0 \\ 0 & \kappa_b^{(2)} \end{pmatrix} Q_b \,, \tag{238}$$

where n_{bath} is the number of bath modes. The full Hamiltonian is then $\boldsymbol{H} = \boldsymbol{H}_0 + \boldsymbol{H}_1 + \boldsymbol{H}_{\mathrm{bath}}$.

This is a much simpler problem than if the symmetries of the 20 less important vibrational modes are correctly taken into account. Treating the pyrazine molecule in a more realistic manner, and expanding the Hamiltonian to second order results in a large number of terms correlating the various modes, and a much more complicated potential energy surface topology. This system has also been examined successfully [37], but here the simpler 4-mode system coupled to the bath model (238) will be used to demonstrate the application of the MCTDH method to a large system exhibiting a conical intersection.

The property of interest is the absorption spectrum. This can be obtained from the auto-correlation function of the system (see Sec. 8.3), propagating the ground-state wavefunction on the excited surfaces. In this system the ground state is a set of harmonic oscillators, and so the initial wavefunction is a product of Gaussian functions.

The model Hamiltonian described above is immediately in the product form required for the efficient implementation of the MCTDH method, and thus it can be used without further thought. The choice of primitive DVR basis is also straightforward: the degrees of freedom are all bound oscillators, and so a harmonic oscillator DVR is the most efficient. In particular, if the DVR functions are generated using the ground-state normal mode frequencies and the ground-state equilibrium position, the initial wavefunction can be exactly represented.

There are three basic choices that still need to be made: the representation of the electronic basis, the choice of integrator, and how to treat such a large number of degrees of freedom. An idea of the optimal choices can be obtained from studying the 4-mode model of pyrazine described above, i.e. including only significant linear coupling terms.

The first step is to find the optimal number of primitive grid points. This can be achieved using a series of calculations, which do not need to be converged with respect to the number of single-particle functions. By analysing the population at the ends of the one-dimensional grids, and monitoring changes in the auto-correlation function, the effect of the basis size can be observed. A primitive basis with 22, 32, 21, and 12 grid points for the modes $\nu_{10\mathrm{a}}, \nu_{6\mathrm{a}}, \nu_1$, and $\nu_{9\mathrm{a}}$, respectively, was found to be sufficient.

The next step is to obtain convergence with respect to the single-particle function basis. This was done by monitoring the auto-correlation function, using the analysis procedure described in Sec. 8.7 to show where more functions are required. Tab. 4 describes the memory and CPU time required for converged MCTDH calculations, propagating the wavepacket for 120 fs using various propagation methods. A calculation using the standard method with the SIL integrator is given as a comparison.

Table 4
Comparison of computational resources needed for the propagation of pyrazine including 4 modes. The first column enumerates the calculations made. The second column selects between the integration schemes. The label "exact" refers to the standard method, Sec. 2.2. In the third column the type of single-particle function basis with respect to the electronic degree of freedom is specified (see Sec. 3.5). Column four defines whether standard, interaction picture, or natural orbitals were used. The next two columns give the CPU time and memory required on an IBM RS/6000 power2 workstation. Finally, "Error" is the maximum error of the calculation with respect to the standard method calculation, i.e. $\| \Psi - \Psi_{\text{exact}} \|$. Note that an error of 0.01 is equivalent to an overlap of 0.99995 (see Eq. (160)).

Run	Integrator	Basis type	Orbitals	CPU [s]	Memory [MB]	Error
1	exact	—	—	6565	67.3	—
2	VMF	single-set	standard	1421	6.1	0.042
3	VMF	multi-set	standard	820	3.0	0.034
4	VMF	multi-set	int. pic.	580	3.1	0.035
5	VMF	multi-set	natural	877	3.1	0.057
6	CMF	multi-set	standard	370	3.3	0.035

The required resources listed in Tab. 4 again demonstrate a large gain factor for all MCTDH calculations with respect to the standard method calculation: the fastest calculation using the CMF integrator and multi-set formulation was a factor of 18 times faster and required 20 times less memory. Note that this gain in CPU time is in good agreement with the estimated gain of 16, Eq. (92). The efficiency of the MCTDH method is especially pleasing when one considers that the problem studied here is a system demonstrating chaotic dynamics, i.e. the wavepacket does not remain localised as in the case of the photo-dissociation of NOCl (see Sec. 9.1). As a result, rather a large number of single-particle functions is required.

In the single-set formulation a single-particle function basis set of $(n_{\nu_{10a}}, n_{\nu_{6a}}, n_{\nu_1}, n_{\nu_{9a}}) = (16, 15, 8, 7)$ was required for convergence, where the notation describes the number of functions required for each degree of freedom respectively. Thus although the factor N/n is not very large the compact form of the wavefunction results in highly efficient propagation. The number of single-particle functions required for the different degrees of freedom reflects the relative strengths of the coupling constants.

In the multi-set formulation, a basis set of $(n_{\nu_{10a}}, n_{\nu_{6a}}, n_{\nu_1}, n_{\nu_{9a}}) =$ S1(9, 15, 8, 6), S2(9, 13, 7, 5) was required, where S1 and S2 denote the sets used for the wavepackets for the respective electronic states. Comparing calculations 2 and 3 shows that, despite the increase in single-particle functions required, this formulation is more efficient than the single-set formulation. The reason for this is that by using this formulation the number of expansion coefficients has been reduced from 26 880 to 10 575 (remember that in the single-set formulation there is an electronic “degree of freedom” with 2 basis functions).

On comparing calculations 3, 4, and 6 the required CPU time for the propagation is seen to decrease on using the more efficient interaction picture and CMF integration schemes. Calculation 5 demonstrates that there is no gain in using the natural orbital picture over the standard single-particle functions. In fact this calculation required more time and the accuracy was lower than calculation 3. This is due to the extra numerical inaccuracies introduced in using the natural orbital constraints (see Eq. (56)).

The error, the maximum difference between the standard method and the MCTDH wavefunctions during the propagation, demonstrates another advantage of the method. The error in the MCTDH wavefunction is between 3-6%, yet the property of interest, the auto-correlation function is converged. Thus effort is not wasted in representing unimportant parts of the wavefunction.

Having obtained a feel for the behaviour of the MCTDH method for the treatment of the 4-mode model, we now turn to treating a system which is impossible to treat using the standard method: the 4-mode system coupled to the strongest 5 bath modes. The coupling constants are listed in Tab. 1 of Ref. [36]. The bath modes included here are numbers b_1 to b_5.

After some small calculations it was decided that 6 primitive basis functions are sufficient for the bath modes. Thus, keeping the primitive basis size as before, a primitive basis set of $(N_{\nu_{10a}}, N_{\nu_{6a}}, N_{\nu_1}, N_{\nu_{9a}}, N_{b_1}, N_{b_2}, N_{b_3}, N_{b_4}, N_{b_5}) = (22, 32, 21, 12, 6, 6, 6, 6, 6)$ was used. This is a total of 1.38×10^9 functions, and a single standard method wavefunction would require 21 GB of memory.

This 9-mode system is a good demonstration of the use of combined modes to reduce the computational resources needed for large calculations (see Sec. 4.5). Tab. 5 lists three calculations using different combination schemes. Again the propagation time was 120 fs and, after the results from the 4-mode calculations, the multi-set formulation was used with the CMF integration scheme.

The first is a straightforward 9-mode MCTDH calculation, i.e. no modes are combined. The single-particle basis set is listed in the table, and despite the large number of expansion coefficients, 3 253 248, the calculation is feasible, although over 7 days of computer time were required. It is interesting to note that the four pyrazine sub-system modes required fewer single-particle functions than in the calculations without the bath modes. This is due to the faster relaxation in the larger system, leading to a simplification of the dynamics.

For the second calculation a combination scheme was used in which the 4 sub-system degrees of freedom were treated as two 2-dimensional particles,

Table 5

Comparison of computational resources needed for the propagation of pyrazine including 9 modes. The first column denotes the combination scheme used. The vibrational modes are listed ν_{10a}, ν_{6a}, ν_1, ν_{9a}, b_1, b_2, b_3, b_4, b_5, and the numbers denote how many modes are combined together, following the order of the list. In the second column the number of single-particle functions is specified. As the multi-set formalism was used S1 and S2 denote the sets used for the different electronic states. The next two columns give the CPU time and memory required on an IBM RS/6000 power2 workstation. The final two columns lists the storage in complex numbers required for the expansion coefficients and single-particle functions.

Combination scheme	No. single-particle functions	CPU [min]	Mem. [MB]	Coefficient storage	spf storage
1,1,1,1,1,1,1,1,1	S1(8,14,7,5,3,4,3,4,4)	10 400	560	3 253 248	1 775
	S2(8,12,6,4,3,4,4,3,3)				
2,2,2,3	S1(27,19,9,12)	185	49	74 024	46 028
	S2(19,14,7,10)				
2,3,4	S1(27,22,16)	325	101	13 950	130 448
	S2(19,18,13)				

while the bath was treated by a 2-dimensional particle and a 3-dimensional particle. Thus the effective number of modes, i.e. the number of particles, was reduced to 4, but the primitive basis for these four particles was increased to 704, 252, 36, and 216 functions. Importantly, the inequality Eq. (78) holds. For example in the first calculation the major two modes, ν_{10a} and ν_{6a}, required $8 \times 14 = 112$ single-particle functions for the S1 electronic state wavepacket, while in the combined calculation the 2-dimensional mode combining these degrees of freedom required only 27 functions. Thus the number of expansion coefficients is dramatically reduced to 74 014, resulting in the enormous saving of resources seen in the table. We mention in passing that a CPU gain of 5000 is estimated when comparing with the standard method.

Using a slightly different combination scheme in the third calculation, in which three particles are used, demonstrates that if the primitive grids become too long the required resources rise. Here the multi-dimensional primitive grids have 704, 1512, and 1296 points. While the number of expansion coefficients drops further to 14 770, the memory and CPU time required rises. One should also note here that, due to the long grids, in the combined mode calculations the CMF integrator needs a factor of 2-3 more memory than the VMF scheme. This is due to the storage of the mean-field tensor, Eq. (90). This storage is usually negligible, but when combined modes with large combined grids are used, this extra storage may become considerable.

A further example of the inefficient use of combined modes is if the 4-mode model calculation is made using two 2-dimensional particles. The single-particle function basis required for convergence is S1(20,20), S2(15,15). Comparing this calculation to calculation 6 in Tab. 4, the number of expansion coefficients is reduced to 697. The memory and CPU time requirements however rise from 3.3 MB and 370 seconds to 27 MB and 5480 seconds.

Thus a balance of combining degrees of freedom together to reduce the number of expansion coefficients, while taking care not to produce long multi-dimensional grids for the single-particle function representations, can result in the treatment of large systems. As a rule of thumb we note that the number of particles, p, should in general satisfy $p \approx d+2$, or equivalently $p \approx \sqrt{f+1}+1$. The power of this approach is clear, and a carefully chosen combination scheme enabled the accurate study of the full 24-dimensional pyrazine-bath problem outlined here [36,38], as well as the realistic 24-dimensional pyrazine system including linear and bi-linear coupling terms [37].

10 Conclusions and outlook

With the accurate treatment of the dynamics of the pyrazine molecule after photo-excitation (see Ref. [36–38] and Sec. 9.4), a system with 24 degrees of freedom and 2 strongly coupled, and thus highly anharmonic potential energy surfaces, it can be claimed that the MCTDH method has come of age. This achievement demonstrates conclusively that the method can live up to its early promise of being capable of treating many degrees of freedom at an affordable cost.

Since the original formulation of the MCTDH equations of motion ten years ago, the techniques needed to implement and use the method have developed a long way. Focusing on typical examples from photo-dissociation, reactive scattering, surface scattering, and photo-excitation, emphasis has been placed on making the method general, able to treat a wide range of dynamical phenomena. In particular, much work has been invested in using the special, extremely compact, form of the MCTDH wavefunction.

Technical developments, such as the CMF integration scheme (see Sec. 5.2), have optimised the efficiency of the algorithm used to solve the equations of motion. Combined with the increase in hardware performance, this has led to a reduction in the CPU time required for the study of the photo-dissociation of NOCl (see Sec. 9.1) from 58 minutes [28] to 8 seconds on a modern workstation. At the same time, the use of combined modes (see Sec. 4.5), has reduced the memory requirements for large systems. The automatic fitting of potential energy surfaces to a product form (see Sec. 6) has also enabled the efficient study of a variety of systems.

Looking ahead, there are still a number of possibilities that would bring further improvements to the method. The development of new DVRs will enable other types of motion, particularly rotational, to be efficiently included in a calculation. Ways of using multi-dimensional potential energy functions can also be improved, with the CDVR method (see Sec. 4.3) providing a possible basis for this. For the study of large systems it is also essential to further reduce the memory and CPU requirements. A possible strategy is the selection of important configurations. This would break the exponential growth of the method with the number of degrees of freedom, at the price of reduced accuracy.

Another goal is the study of solvated systems. Here, the relevant sub-system may be represented by a reduced density matrix [79] and the influence of the solvent is then accounted for by dissipative operators of the Redfield [167] or Lindblad [168] type. Such an approach requires the extension of MCTDH to density matrices [169]. An alternative route is to retain the wavefunction picture and account for only a finite number (10 to 30 say) of solvent atoms.

There are thus many solvent degrees of freedom, but the solvation dynamics may be very simple, so allowing an approximate, e.g. semi-classical, treatment of the solvent dynamics. Both these extensions of the MCTDH approach are currently under investigation.

In conclusion, the MCTDH method opens up the possibility to study molecular dynamics in a general and efficient manner. It is therefore likely to play a major role in the theoretical study of the dynamics of molecules in the years ahead.

Acknowledgements

There are several people who over the years contributed to the research presented here. The first one to mention is U. Manthe who wrote the very first MCTDH program and performed the first applications as part of his PhD-thesis. We then like to thank our former post-docs M. Ehara and M.-C. Heitz, as well as A. Raab and U. V. Riss for their contributions to the MCTDH project and for many lively discussions. Last but not least we like to thank L. S. Cederbaum for his continuous interest in and his strong support of the MCTDH project.

This work has been financially supported by the Deutsche Forschungsgemeinschaft, partly through the Schwerpunktprogramm *Zeitabhängige Phänomene und Methoden in Quantensystemen der Physik und Chemie*. This support is very gratefully acknowledged.

A Variational principles for the time-dependent Schrödinger equation

The first variational principle (VP) for solving time-dependent quantal problems was introduced by Dirac [19] and Frenkel [66]. This Dirac-Frenkel variational principle reads

$$\langle \delta\Psi \,|\, H - i\,\partial_t \,|\, \Psi \rangle = 0\,, \tag{A.1}$$

where ∂_t denotes the partial derivative with respect to time. This VP has been criticised by McLachlan [20] for not being a minimum principle. McLachlan proposed the VP

$$\|\, i\theta - H\Psi \,\|^2 = \mathrm{Min}\,, \tag{A.2}$$

where θ is to be varied and $\dot{\Psi}$ is then set to the optimal value of θ. Finally, a third VP has been set up by employing the usual Lagrange formulation [170]

$$\delta \int_{t_1}^{t_2} L\,dt \;=\; 0\,, \tag{A.3}$$

where the Lagrangian L is given by

$$L = \langle \Psi \,|\, H - i\,\partial_t \,|\, \Psi \rangle \tag{A.4}$$

and the usual boundary conditions $\delta L(t_1) = \delta L(t_2) = 0$ apply.

It has been shown [21] that the two latter VPs can be reformulated to yield

$$\mathrm{Im}\,\langle \delta\Psi \,|\, H - i\,\partial_t \,|\, \Psi \rangle = 0 \tag{A.5}$$

for the McLachlan VP, and

$$\mathrm{Re}\,\langle \delta\Psi \,|\, H - i\,\partial_t \,|\, \Psi \rangle = 0 \tag{A.6}$$

for the Lagrangian VP. Hence all three VPs become equivalent when $i\,\delta\Psi$ is an allowed variation for each allowed variation $\delta\Psi$. Assume that the model function Ψ depends on a set of parameters $\{\lambda_k\}$. The allowed variations are then just the partial derivatives with respect to the parameters: $\delta\Psi = \partial\Psi/\partial\lambda_k$. If the parameters λ_k are complex and Ψ is complex differentiable with respect to its parameters then the criterion above is fulfilled, and all three VPs are equivalent. In this case one should use the Dirac-Frenkel VP because it is the simplest of the three.

The space of allowed variations, $\{\delta\Psi\}$, is the space built by all linear combinations of the partial derivatives $\partial\Psi/\partial\lambda_k$ where, however, only real coefficients are allowed if the parameters λ_k are real. For later reference we note that $\dot{\Psi} \in \{\delta\Psi\}$ always holds because $\dot{\Psi} = \sum \dot{\lambda}_k \, \partial\Psi/\partial\lambda_k$. On the other hand, $\Psi \in \{\delta\Psi\}$ does not necessarily hold. It is true if the length of the vector Ψ can be varied, e.g. if the parameters are linear.

The parameters to be varied in case of an MCTDH model wavefunction are the coefficients $A_{j_1 \dots j_f}$ and the single-particle functions $\varphi^{(\kappa)}_{j_\kappa}$. These parameters are complex and it is sufficient to use the Dirac-Frenkel VP. The space of all allowed variations, $\{\delta\Psi\}$, is thus the complex linear space

$$\{\delta\Psi\} = \mathrm{span}\left\{\Phi_J, \Psi^{(\kappa)}_{l_\kappa}\chi^{(\kappa)}\right\} , \tag{A.7}$$

where "span" denotes the complex linear space spanned by the arguments. $\Psi^{(\kappa)}_{l_\kappa}$ denotes a single-hole function as defined in Sec. 3.1, $\chi^{(\kappa)}$ denotes an arbitrary square-integrable function and the indices J, κ and l_κ run over their usual sets. $\Psi \in \{\delta\Psi\}$ holds for MCTDH wavefunctions because $\Psi = \sum A_J \, \Phi_J$.

Theorem
The equations of motion derived from the Dirac-Frenkel variational principle conserve both norm and energy, if the Hamiltonian is explicitly time-independent, $\partial_t H = 0$, and if the model wavefunction Ψ itself is contained in the space of the allowed variations: $\Psi \in \{\delta\Psi\}$.

In order to prove this theorem, first an expression for the time derivative of the expectation value of the nth moment of the Hamiltonian is derived:

$$\begin{aligned}
\frac{d}{dt}\langle\Psi\,|\,H^n\,|\,\Psi\rangle &= \langle\dot{\Psi}\,|\,H^n\,|\,\Psi\rangle + \langle\Psi\,|\,H^n\,|\,\dot{\Psi}\rangle \\
&= 2\,\mathrm{Re}\,\langle\Psi\,|\,H^n\,|\,\dot{\Psi}\rangle \\
&= -2\,\mathrm{Im}\,\langle H^n\Psi\,|\,{-i}\,\partial_t\,|\,\Psi\rangle \\
&= -2\,\mathrm{Im}\,\langle H^n\Psi\,|\,H - i\,\partial_t\,|\,\Psi\rangle \,.
\end{aligned} \tag{A.8}$$

The transformation of the last line was performed by addition of the real expectation value $\langle\Psi\,|\,H^{n+1}\,|\,\Psi\rangle$.

For $n = 0$ Eq. (A.8) proves the conservation of norm:

$$\frac{d}{dt}\langle\Psi\,|\,1\,|\,\Psi\rangle = -2\,\mathrm{Im}\,\langle\Psi\,|\,H - i\,\partial_t\,|\,\Psi\rangle = 0\,, \tag{A.9}$$

as Eq. (A.1) ensures that $\langle \Psi \mid H - i\,\partial_t \mid \Psi \rangle$ vanishes because $\delta\Psi = \Psi$ is an allowed variation by assumption.

The case $n = 1$ demonstrates the conservation of energy:

$$\begin{aligned}
\frac{d}{dt}\langle \Psi \,|\, H \,|\, \Psi \rangle &= -2\,\mathrm{Im}\,\langle H\Psi \,|\, H - i\,\partial_t \,|\, \Psi \rangle \\
&= -2\,\mathrm{Im}\Big[\langle (H - i\,\partial_t)\,\Psi \,|\, (H - i\,\partial_t)\,\Psi \rangle + \langle i\,\partial_t\Psi \,|\, H - i\,\partial_t \,|\, \Psi \rangle\Big] \\
&= 2\,\mathrm{Re}\,\langle \partial_t\Psi \,|\, H - i\,\partial_t \,|\, \Psi \rangle \\
&= 0\,, \qquad\qquad (\mathrm{A.10})
\end{aligned}$$

since $\delta\Psi = \partial_t\Psi$ is always an allowed variation (see above).

Finally, $n = 2$ yields the energy deviation:

$$\begin{aligned}
\frac{d}{dt}\langle \Psi \,|\, H^2 \,|\, \Psi \rangle &= -2\,\mathrm{Im}\,\langle H^2\Psi \,|\, H - i\,\partial_t \,|\, \Psi \rangle \\
&= -2\,\mathrm{Im}\Big[\langle (H - i\,\partial_t)\,\Psi \,|\, H \,|\, (H - i\,\partial_t)\,\Psi \rangle \qquad (\mathrm{A.11}) \\
&\qquad + \langle i\,\partial_t\Psi \,|\, H\,(H - i\,\partial_t) \,|\, \Psi \rangle\Big] \\
&= -2\,\mathrm{Im}\,\langle i\,\partial_t\Psi \,|\, H\,(H - i\,\partial_t) \,|\, \Psi \rangle \\
&= 2\,\mathrm{Re}\,\langle H\,\partial_t\Psi \,|\, H - i\,\partial_t \,|\, \Psi \rangle \\
&\neq 0 \quad \text{in general}\,, \qquad\qquad (\mathrm{A.12})
\end{aligned}$$

since, in general, $\delta\Psi = H\,\partial_t\Psi$ is not an allowed variation.

B Discrete variable representation (DVR)

The discrete variable representation (DVR) is a powerful method for representing wavefunctions and operators. It is a general approach which is of interest on its own and is only loosely connected to MCTDH. We therefore find it convenient to adopt here a notation that is well suited for the following discussion, but is slightly different from the one used elsewhere in this review. The coordinate is now called x (rather than Q), and φ denotes a basis function which must not be confused with a single-particle function. To clearly distinguish operators from their matrix representation and eigenvalues, we indicate an operator by a hat ($\hat{}$), and mark vectors and matrices by bold face type.

B.1 VBR and FBR representation of the potential

We consider a one-dimensional problem and choose a complete square-integrable basis set

$$\{\varphi_j(x)\}_{j=1}^{\infty} \ , \tag{B.1}$$

where $x\varphi_j(x)$ and $\varphi_j'(x) = d\varphi_j/dx$ are also square-integrable. It is further assumed that the matrix elements

$$Q_{jk} = \langle \varphi_j \,|\, \hat{x} \,|\, \varphi_k \rangle \tag{B.2}$$
$$D^{(1)}_{jk} = \langle \varphi_j \,|\, d/dx \,|\, \varphi_k \rangle \tag{B.3}$$
$$D^{(2)}_{jk} = \langle \varphi_j \,|\, d^2/dx^2 \,|\, \varphi_k \rangle \tag{B.4}$$

can be evaluated analytically. We truncate the basis set to its first N members, $\{\varphi_j(x)\}_{j=1}^{N}$, and introduce the projector onto the finite basis set,

$$\hat{P} = \sum_{j=1}^{N} |\,\varphi_j\rangle\langle\varphi_j\,| \ , \tag{B.5}$$

as well as the $N \times N$ matrices $\boldsymbol{Q}$, $\boldsymbol{D}^{(1)}$ and $\boldsymbol{D}^{(2)}$, the matrix elements of which are given by Eqs. (B.2), (B.3), and (B.4).

As a result, as the matrices $\boldsymbol{D}^{(1)}$ and $\boldsymbol{D}^{(2)}$ are known, there is no problem in evaluating the kinetic energy when computing matrix elements of the Hamiltonian $\hat{H} = \hat{T} + \hat{V}$. The evaluation of matrix elements of the potential,

$$V^{\mathrm{VBR}}_{jk} = \langle \varphi_j \,|\, \hat{V} \,|\, \varphi_k \rangle \ , \tag{B.6}$$

is however in general non-trivial. In fact, the computation of these matrix elements by accurate numerical integration may take considerable more computational time than the full diagonalisation of the Hamilton matrix. The superscript VBR appearing in the above equation stands for *variational basis-set representation.* This naming [85] emphasises that the eigenvalues of the thus obtained Hamiltonian matrix are variational upper bounds to the exact ones.

The potential operator $\hat{V}$ can be considered as a real function V of the position operator $\hat{x}$, i.e. $\hat{V} = V(\hat{x})$. Turning from operators to their matrix representation one may consider the potential matrix as a function of the position matrix $\boldsymbol{Q}$, i.e.

$$\boldsymbol{V}^{\mathrm{FBR}} = V(\boldsymbol{Q}) \ , \tag{B.7}$$

where the superscript FBR stands for *finite basis-set representation.*

Equation (B.7) would be exact (i.e. $\boldsymbol{V}^{\mathrm{FBR}}$ would equal $\boldsymbol{V}^{\mathrm{VBR}}$) if the basis set were complete. Since we are using a truncated basis set, however, we are introducing an error. This can be most easily seen by considering the quadratic potential $V(x) = x^2$. Then

$$\hat{V}^{\mathrm{VBR}} = \hat{P}\hat{V}\hat{P} = \hat{P}\hat{x}^2\hat{P} \tag{B.8}$$

and

$$\hat{V}^{\mathrm{FBR}} = V\left(\hat{P}\hat{x}\hat{P}\right) = \hat{P}\hat{x}\hat{P}\hat{x}\hat{P} \, . \tag{B.9}$$

However, Eq. (B.7) is a useful approximation. To evaluate it one diagonalises $\boldsymbol{Q}$,

$$\boldsymbol{Q} = \boldsymbol{U}\boldsymbol{X}\boldsymbol{U}^{\dagger} \, , \tag{B.10}$$

where $\boldsymbol{U}$ denotes the eigenvector matrix and $\boldsymbol{X}$ is the diagonal matrix of eigenvalues x_α, i.e. $X_{\alpha\beta} = x_\alpha \, \delta_{\alpha\beta}$. (Note that we are numbering the basis functions by Latin letters $j, k, \ldots$ and the grid points, x_α, by Greek letters $\alpha, \beta, \ldots$) The potential matrix elements in the finite basis-set representation are then given by

$$V_{jk}^{\mathrm{FBR}} = \sum_{\alpha=1}^{N} U_{j\alpha} \, V(x_\alpha) \, U_{k\alpha}^{*} \, . \tag{B.11}$$

This idea of evaluating potential matrix elements by diagonalisation of the position operator goes back to Harris *et al.* [83].

It is instructive to investigate the relationship between Eq. (B.11) and a quadrature formula,

$$V_{jk}^{\mathrm{quad}} = \sum_{\alpha=1}^{N} w_\alpha \, \varphi_j^*(x_\alpha) \, V(x_\alpha) \, \varphi_k(x_\alpha) \, , \tag{B.12}$$

where w_α are the weights of the quadrature. Equating V^{FBR} with V^{quad} yields

$$w_\alpha^{1/2} = U_{k\alpha}^* / \varphi_k(x_\alpha) \, , \tag{B.13}$$

which implies that $U_{k\alpha}^*/\varphi_k(x_\alpha)$ must be independent of k, but there is no reason why this should hold in general. However, for tridiagonal representations of the position operator Dickinson and Certain [84] were able to show that the FBR representation (B.7) and (B.11) is equivalent to a Gaussian quadrature. Provided $\boldsymbol{Q}$ is tridiagonal for all N, Eq. (B.13) holds and its right hand side is independent of k. Moreover, the Gaussian quality (see Sec. B.3) of the quadrature ensures that the overlap integrals as well as the matrix elements of the position operator are then given *exactly* by quadrature:

$$\sum_{\alpha=1}^{N} w_\alpha \, \varphi_j^*(x_\alpha) \, \varphi_k(x_\alpha) = \langle \varphi_j \, | \, \varphi_k \rangle = \delta_{jk} \, , \tag{B.14}$$

$$\sum_{\alpha=1}^{N} w_\alpha \, \varphi_j^*(x_\alpha) \, x_\alpha \, \varphi_k(x_\alpha) = \langle \varphi_j \, | \, \hat{x} \, | \, \varphi_k \rangle = Q_{jk} \, . \tag{B.15}$$

One therefore expects that the FBR is more accurate when using basis functions φ_j that tridiagonalise $\hat{x}$, e.g. harmonic oscillator functions.

B.2 Diagonalisation DVR

We have introduced the FBR approach in order to efficiently (but approximately) evaluate potential matrix elements. To this end the eigenvalues x_α and the eigenvector matrix $\boldsymbol{U}$ of the position operator were needed. The knowledge of the unitary matrix $\boldsymbol{U}$ allows us to perform a conceptually new step: the matrix $\boldsymbol{U}$ is used to unitarily transform the FBR to the *discrete variable representation* (DVR). To this end we establish the DVR functions

$$\chi_\alpha(x) = \sum_{j=1}^{N} \varphi_j(x) \, U_{j\alpha} \, . \tag{B.16}$$

These functions are orthonormal, $\langle \chi_\alpha \,|\, \chi_\beta \rangle = \delta_{\alpha\beta}$, and diagonalise — by construction — the position operator $\langle \chi_\alpha \,|\, \hat{x} \,|\, \chi_\beta \rangle = x_\alpha \, \delta_{\alpha\beta}$. From the last equation follows:

$$\hat{x}\, \chi_\alpha(x) = x_\alpha \, \chi_\alpha(x) + r_\alpha(x)\,, \tag{B.17}$$

where the residual term r_α is orthogonal to the basis, i.e. $\hat{P} r_\alpha = 0$. If r_α vanished, χ_α would necessarily be proportional to $\delta(x - x_\alpha)$. Hence χ_α acts like a δ-function within the space spanned by the basis set.

Next we transform the Hamiltonian, i.e. the kinetic energy T and the potential V, to the DVR:

$$\boldsymbol{T}^{\mathrm{DVR}} = \boldsymbol{U}^\dagger \, \boldsymbol{T} \, \boldsymbol{U}\,, \tag{B.18}$$
$$\boldsymbol{V}^{\mathrm{DVR}} = \boldsymbol{U}^\dagger \, \boldsymbol{V}^{\mathrm{FBR}} \, \boldsymbol{U}\,, \tag{B.19}$$

with $T_{jk} = \langle \varphi_j \,|\, \hat{T} \,|\, \varphi_k \rangle$. Note that $T^{\mathrm{DVR}}_{\alpha\beta} = \langle \chi_\alpha \,|\, \hat{T} \,|\, \chi_\beta \rangle$ is an exact expression, while $V^{\mathrm{DVR}}_{\alpha\beta} = \langle \chi_\alpha \mid \hat{V} \mid \chi_\beta \rangle$ holds only approximately because the FBR approximation has been adopted. Using Eqs. (B.11) and (B.19) one immediately finds that

$$V^{\mathrm{DVR}}_{\alpha\beta} = V(x_\alpha) \, \delta_{\alpha\beta}\,. \tag{B.20}$$

It is this relation what makes the DVR so attractive.

It has been discussed in the previous section that the FBR approximation is related to a Gaussian quadrature if the representation of the position operator is tridiagonal. If the DVR is based on such an FBR we will speak of a proper DVR, and of an improper DVR if the matrix $\boldsymbol{Q}$ is not tridiagonal. In the following we shall concentrate on proper DVRs, but note that the CDVR method of Sec. 4.3 is based on an improper DVR.

For a proper DVR it is not difficult to prove that the following results hold: *discrete orthonormality*,

$$\sum_{\alpha=1}^{N} w_\alpha \, \varphi_j^*(x_\alpha) \, \varphi_k(x_\alpha) = \delta_{jk}\,, \tag{B.21}$$

discrete completeness,

$$\sum_{j=1}^{N} (w_\alpha w_\beta)^{1/2} \, \varphi_j^*(x_\alpha) \, \varphi_j(x_\beta) = \delta_{\alpha\beta}\,, \tag{B.22}$$

discrete δ-property,

$$\chi_\alpha(x_\beta) = w_\alpha^{-1/2}\,\delta_{\alpha\beta} \tag{B.23}$$

and

$$\langle \chi_\alpha \,|\, \psi \rangle = w_\alpha^{1/2}\,\psi(x_\alpha)\,, \tag{B.24}$$

where the last equation is only valid if ψ lies entirely in the basis set, i.e. $\hat{P}\psi = \psi$. Equation (B.24) turns a (proper) DVR into a collocation method. The wavefunction is no longer represented by its overlaps with basis functions, but by its values on grid points x_α, i.e.

$$\psi(x) \to \boldsymbol{\psi} = \left(w_1^{1/2}\psi(x_1), w_2^{1/2}\psi(x_2), \ldots, w_N^{1/2}\psi(x_N)\right)^T\,. \tag{B.25}$$

As a final remark we note that it is sometimes advantageous not to diagonalise the position operator $\hat{x}$ but some real, invertable function of it, $\hat{\tilde{x}} = g(\hat{x})$. Such a change of variables may be necessary in order to arrive at a tridiagonal representation (see Secs. B.4.2, B.4.3, B.4.4 and B.4.5). The grid points are then given by $x_\alpha = g^{-1}(\tilde{x}_\alpha)$, where the $\tilde{x}_\alpha$ are the eigenvalues of the matrix representation of $\hat{\tilde{x}}$.

B.3 Quadrature DVR

A (proper) DVR may be alternatively derived from a Gaussian quadrature, circumventing the diagonalisation of the position operator. This route was followed by Light and coworkers [85,86,171,172], who coined the abbreviations VBR, FBR and DVR.

Assume that there are a non-negative weight function $w(x)$ and polynomials $p_j(x)$, $(j = 0, 1, \ldots)$ of degree j, which are orthogonal to each other with respect to the weight function $w(x)$. (For example, the Hermite polynomials are orthogonal to each other with respect to the weight function $w(x) = \exp(-x^2)$.) Then there exists a Gaussian quadrature formula [102] with weights w_α and nodes x_α such that

$$\int w(x)\, f(x)\, dx = \sum_{\alpha=1}^{N} w_\alpha\, f(x_\alpha) \tag{B.26}$$

holds exactly for all polynomials of degree lower or equal to $2N - 1$.

Next one defines the basis functions φ_j as

$$\varphi_j(x) = A_j \, w^{1/2}(x) \, p_{j-1}(x) \,, \qquad j = 1, \ldots, N \,, \tag{B.27}$$

where A_j is a normalisation constant. This is an orthonormal basis set by construction. Because the Gaussian quadrature rule (B.26) is exact for all polynomials up to $(2N-1)$th degree, one finds that all overlap integrals and all matrix elements of the position operator are exactly reproduced by the quadrature formula, i.e. Eqs. (B.14) and (B.15) hold.

Following Light *et al.* [85] we introduce a transformation matrix

$$Y_{\alpha j} = w_\alpha^{1/2} \, \varphi_j(x_\alpha) \tag{B.28}$$

and find that this matrix is unitary,

$$\left(\boldsymbol{Y}^\dagger \boldsymbol{Y}\right)_{jk} = \sum_{\alpha=1}^{N} w_\alpha \, \varphi_j^*(x_\alpha) \, \varphi_k(x_\alpha) = \delta_{jk} \,. \tag{B.29}$$

The unitarity of $\boldsymbol{Y}$ implies that $\left(\boldsymbol{Y} \boldsymbol{Y}^\dagger\right)_{\alpha\beta} = \delta_{\alpha\beta}$ also holds, which — when inserting Eq. (B.28) — proves discrete completeness, Eq. (B.22). Introducing the DVR functions

$$\chi_\alpha(x) = \sum_{j=1}^{N} Y_{\alpha j}^* \, \varphi_j(x) = \sum_{j=1}^{N} w_\alpha^{1/2} \, \varphi_j^*(x_\alpha) \, \varphi_j(x) \,, \tag{B.30}$$

it is easy to show that these functions satisfy the δ-property, Eqs. (B.23) and (B.24). (Set $x = x_\beta$ in the last equation and use discrete completeness.) All potential matrix elements are evaluated by the Gaussian quadrature rule. This and the δ-property leads to the DVR formula (B.20) for the potential.

Finally, when comparing Eq. (B.13) with Eq. (B.28), one finds that $\boldsymbol{Y} = \boldsymbol{U}^\dagger$ holds, showing that a quadrature DVR and a (proper) diagonalisation DVR are equivalent. (There is no improper quadrature DVR.) As discussed in the previous section it may be advantageous to transform the variable x to $\tilde{x} = g(x)$, because there may be a Gaussian quadrature rule only when integrating over the new variable $\tilde{x}$. See Secs. B.4.2, B.4.3, B.4.4, and B.4.5 for examples.

B.4 Examples

In the following sections some particular DVRs and related representations will be discussed.

B.4.1 Harmonic oscillator DVR

In the *harmonic oscillator DVR* the harmonic oscillator functions

$$\begin{aligned}\varphi_j(x) = &\left(2^j j!\right)^{-1/2} (m\omega/\pi)^{1/4}\, H_j\left(\sqrt{m\omega}\,(x - x_{\text{eq}})\right) \\ &\times \exp\left(-\tfrac{1}{2}\, m\omega\,(x - x_{\text{eq}})^2\right)\end{aligned} \tag{B.31}$$

are taken as basis functions. H_j denotes the jth Hermite polynomial [173] and — in order to be consistent with the usual nomenclature — we here let j start from zero, $j = 0, 1, \ldots, N-1$. The matrix elements of the position operator are well-known:

$$\langle \varphi_j \,|\, \hat{x} \,|\, \varphi_k \rangle = \sqrt{\frac{j+1}{2m\omega}}\, \delta_{j,k-1} + x_{\text{eq}}\, \delta_{jk} + \sqrt{\frac{j}{2m\omega}}\, \delta_{j,k+1} \,. \tag{B.32}$$

The diagonalisation of this matrix yields the transformation $\boldsymbol{U}$ and the grid points x_α. The weights are given by

$$w_\alpha^{1/2} = (m\omega/\pi)^{-1/4} \exp\left(\tfrac{1}{2}\, m\omega\,(x_\alpha - x_{\text{eq}})^2\right) U_{0\alpha} \,, \tag{B.33}$$

according to Eq. (B.13).

The phases of the eigenvectors of the position operator, i.e. the column vectors of $\boldsymbol{U}$, are arbitrary. They are chosen such that $w_\alpha^{1/2}$ is positive, i.e. the sign of a column vector is changed if $w_\alpha^{1/2}$ would otherwise be negative. This is done for all DVRs, but will not be mentioned later.

The matrix of first derivatives is also well-known,

$$D_{jk}^{(1)} = \langle \varphi_j \,|\, \tfrac{d}{dx} \,|\, \varphi_k \rangle = -\sqrt{\frac{m\omega}{2}} \left(\sqrt{j+1}\, \delta_{j,k-1} - \sqrt{j}\, \delta_{j,k+1}\right) \,, \tag{B.34}$$

and its DVR form reads

$$\begin{aligned} D_{\alpha\beta}^{(1),\text{DVR}} &= \left(\boldsymbol{U}^\dagger \boldsymbol{D}^{(1)} \boldsymbol{U}\right)_{\alpha\beta} \\ &= \sqrt{\frac{m\omega}{2}} \sum_{k=0}^{N-2} \sqrt{k+1} \left(U_{k\alpha}^*\, U_{k+1,\beta} - U_{k+1,\alpha}^*\, U_{k\beta}\right) \,. \end{aligned} \tag{B.35}$$

One could act similarly for $\boldsymbol{D}^{(2)}$, but it is easier to make use of the fact that the Hamiltonian matrix is diagonal with eigenvalues $\omega\,(k + 1/2)$:

$$\begin{aligned} D_{\alpha\beta}^{(2),\text{DVR}} &= -2m \left(\boldsymbol{U}^\dagger\,(\boldsymbol{H} - \boldsymbol{V})\,\boldsymbol{U}\right)_{\alpha\beta} \\ &= -2m\omega \sum_{k=0}^{N-1} U_{k\alpha}^* \left(k + \tfrac{1}{2}\right) U_{k\beta} + m^2\omega^2 (x_\alpha - x_{\text{eq}})^2 \delta_{\alpha\beta} \,. \end{aligned} \tag{B.36}$$

B.4.2 Radial harmonic oscillator DVR

The *radial harmonic oscillator DVR* is an appropriate DVR when the wavefunction is defined on a half-axis $[x_0, \infty[$ only, and satisfies the boundary condition $\psi(x_0) = 0$. The odd harmonic oscillator functions are chosen as basis:

$$\varphi_j(x) = \sqrt{2}\,\varphi^{\mathrm{HO}}_{2j-1}(x)\,, \tag{B.37}$$

where $j = 1, \ldots, N$, and where φ^{HO} denotes a harmonic oscillator function as defined by Eq. (B.31), but with x_{eq} replaced by x_0 for convenience. The normalisation factor $\sqrt{2}$ appears because one now considers only a half-axis. The position operator does not have a tridiagonal representation in this basis, but the transformed variable $z = (x - x_0)^2$ does:

$$\begin{aligned} Q_{jk} &= \langle \varphi_j \,|\, \hat{z} \,|\, \varphi_k \rangle\,, \qquad\qquad (\mathrm{B.38}) \\ &= \frac{\sqrt{2j\,(2j+1)}}{2m\omega}\,\delta_{j,k-1} + \frac{4j-1}{2m\omega}\,\delta_{j,k} + \frac{\sqrt{(2j-1)(2j-2)}}{2m\omega}\,\delta_{j,k+1}\,. \end{aligned}$$

The DVR grid points and weights are obtained after diagonalisation of this matrix:

$$x_\alpha = \sqrt{z_\alpha} + x_0 \tag{B.39}$$

$$w_\alpha^{1/2} = \pi^{1/4}\,(m\omega)^{-3/4}\,(x - x_0)^{-1} \exp\left(\tfrac{1}{2}\,m\omega\,(x_\alpha - x_{\mathrm{eq}})^2\right) U_{1\alpha}\,, \tag{B.40}$$

where z_α denotes an eigenvalue of the (transformed) position operator matrix (B.38).

The matrix elements of d/dx are not analytically given in the radial harmonic oscillator basis, one uses the operator $\frac{1}{2}\left((x - x_0)\,d/dx + d/dx\,(x - x_0)\right)$ instead. This first derivative operator has the matrix elements

$$\begin{aligned} D^{(1)}_{jk} &= \frac{1}{2}\,\langle \varphi_j \,|\, (x - x_0)\,\frac{d}{dx} + \frac{d}{dx}\,(x - x_0) \,|\, \varphi_k \rangle \\ &= -\sqrt{2j\,(2j+1)}\,\delta_{j,k-1} + \sqrt{(2j-1)(2j-2)}\,\delta_{j,k+1}\,. \qquad (\mathrm{B.41}) \end{aligned}$$

The matrix of second derivatives, $\boldsymbol{D}^{(2)}$, has matrix elements similar to Eq. (B.38), but with negative off-diagonal elements and with $1/(m\omega)$ replaced by $m\omega$. The transformation of the derivative matrices to DVR form is similar to Eqs. (B.35) and (B.36) but with $\sqrt{m\omega/2}\,\sqrt{k+1}$ replaced by $\sqrt{2k\,(2k+1)}$, and with $(k + 1/2)$ replaced by $(2k - 1/2)$, respectively. The sums run now from 1 to N.

B.4.3 Legendre DVR

A *Legendre DVR* is employed for angular degrees of freedom because the associated Legendre functions $P_l^m(\cos\theta)$ are eigenfunctions of the angular momentum operator

$$\hat{l}^2 = -\frac{1}{\sin\theta}\frac{d}{d\theta}\sin\theta\frac{d}{d\theta} + \frac{m^2}{\sin^2\theta}\,, \tag{B.42}$$

where the magnetic quantum number m is treated as a fixed parameter. The basis functions are thus the $\mathcal{L}^2$-normalised associated Legendre functions,

$$\varphi_{l-m+1}(\theta) = \tilde{P}_l^m(\theta) = (-1)^m \sqrt{\frac{2\,l+1}{2}\frac{(l-m)!}{(l+m)!}}\, P_l^m(\cos\theta)\,, \tag{B.43}$$

with $m \geq 0$ and l restricted to $m \leq l \leq m+N-1$. These functions are closely related to the spherical harmonics: $Y_{lm}(\theta,\phi) = (2\pi)^{-1/2}\tilde{P}_l^m(\cos\theta)\,e^{im\phi}$ for $m \geq 0$.

From the recurrence relation of the Legendre polynomials [173] follows the recursion

$$c_{l+1}\tilde{P}_{l+1}^m(x) - x\tilde{P}_l^m(x) + c_l\tilde{P}_{l-1}^m(x) = 0\,, \tag{B.44}$$

with

$$c_l = \sqrt{\frac{l^2-m^2}{4\,l^2-1}} \tag{B.45}$$

and

$$x = \cos\theta\,. \tag{B.46}$$

It is now obvious that in the present case one should not diagonalise the matrix representation of the coordinate θ — this would not lead to a tridiagonal matrix — but diagonalise the representation of the transformed coordinate $x = \cos\theta$. The matrix representation of $\hat{x}$ follows directly from Eq. (B.44) since the polynomials $\tilde{P}_l^m$ are orthonormal.

In the case of a Legendre DVR it is convenient to replace the derivative operator $d/d\theta$ by $d/d\theta\,\sin\theta$. (Multiplying the latter operator with the imaginary unit i turns it into a Hermitian operator, whereas $i\, d/d\theta$ is not Hermitian because of the volume element $\sin\theta\, d\theta$.) In the transformed variable x this first derivative operator reads

$$\frac{d}{d\theta}\sin\theta = \left(x^2 - 1\right)\frac{d}{dx} + x\,, \tag{B.47}$$

and a recursion involving $d/d\theta\, P_l^m(x)$ [173] can be transformed to

$$\left(\left(x^2 - 1\right)\frac{d}{dx} + x\right)\tilde{P}_l^m(x) = (l+1)\, c_{l+1}\, \tilde{P}_{l+1}^m(x) - l\, c_l \tilde{P}_{l-1}^m(x)\,. \tag{B.48}$$

The matrix representation of the first derivative follows immediately from this equation. Similarly to the first derivative, the second derivative $d^2/d\theta^2$ is not useful but is replaced by the operator $\hat{l}^2$ (see Eq. (B.42)), the matrix representation of which is diagonal with eigenvalues $l\,(l+1)$.

Finally, the matrix representation of $\cos\theta$ is diagonalised. The eigenvalues x_α of this matrix determine the DVR grid points, $\theta_\alpha = \arccos x_\alpha$, and the DVR weights are given by

$$w_\alpha^{1/2} = \sqrt{\frac{2^{m+1}\, m!}{(2\,m+1)!!}}\, \sin^{-m}(\theta_\alpha)\, U_{1\alpha}\,, \tag{B.49}$$

where the first row of $\boldsymbol{U}$ refers to the lowest value of l, i.e. $l = m$. As in the previous section, $\boldsymbol{U}$ is then used to transform the matrices of first and second derivatives (i.e. $d/d\theta\, \sin\theta$ and $\hat{l}^2$) to DVR form (compare with Eqs. (B.35) and (B.36)).

There are cases, e.g. the scattering of an atom off a homonuclear diatom, where the potential is symmetric in θ with respect to $\theta = \pi/2$. The potential can then be considered as a function of $\cos^2\theta$, and the Hamiltonian couples only even with even and odd with odd l-states. The number of basis functions can thus be halved by choosing

$$\varphi_k(\theta) = \tilde{P}_{l_{\min}+2k-2}^m(\cos\theta) \tag{B.50}$$

as basis functions, with $l_{\min} = m$ for even and $l_{\min} = m+1$ for odd symmetry. In order to arrive at a tridiagonal representation we now have to consider $\widehat{x^2}$. Iterating Eq. (B.44) yields

$$c_{l+2}\, c_{l+1}\, \tilde{P}_{l+2}^m(x) + \left(c_l^2 + c_{l+1}^2 - x^2\right)\tilde{P}_l^m(x) + c_l\, c_{l-1}\, \tilde{P}_{l-2}^m(x) = 0\,, \tag{B.51}$$

which shows that the matrix representation of $\widehat{x^2}$ is tridiagonal. The resulting eigenvalues are called x_α^2, and the grid points $\theta_\alpha = \arccos(x_\alpha)$ lie in the interval $]0, \pi/2[$, whereas they are distributed over $]-\pi/2, \pi/2[$ when no symmetry is used.

The expression (B.49) for the weights remains unchanged for even symmetry ($l_{\min} = m$), but is to be replaced by

$$w_\alpha^{1/2} = \sqrt{\frac{2^{m+1}\, m!}{(2\,m+3)!!}}\; (\cos\theta_\alpha\, \sin^m \theta_\alpha)^{-1}\, U_{1\alpha} \tag{B.52}$$

for odd symmetry ($l_{\min} = m+1$). As the first derivative we now define

$$\frac{1}{2}\left(\frac{d}{d\theta}\, \sin\theta\, \cos\theta + \cos\theta\, \frac{d}{d\theta}\, \sin\theta\right) = \frac{3\,x^2-1}{2} + x\left(x^2-1\right)\frac{d}{dx}\,, \tag{B.53}$$

the matrix elements of which can be deduced from the recursion

$$\begin{aligned}&\left(\frac{3\,x^2-1}{2} + x\left(x^2-1\right)\frac{d}{dx}\right)\tilde{P}_l^m(x) = \\ &\qquad \left(l+\frac{3}{2}\right) c_{l+1}\, c_{l+2}\, \tilde{P}_{l+2}^m(x) - \left(l-\frac{1}{2}\right) c_l\, c_{l-1}\, \tilde{P}_{l-2}^m(x)\,.\end{aligned} \tag{B.54}$$

Otherwise the procedure remains unchanged.

B.4.4 Sine DVR

The *sine DVR* uses the particle-in-a-box eigenfunctions as a basis. The box boundaries are x_0 and x_{N+1}, and $L = x_{N+1} - x_0$ denotes the length of the box. The basis functions are thus

$$\varphi_j(x) = \begin{cases} \sqrt{\frac{2}{L}}\sin\left(j\pi(x-x_0)/L\right) & \text{for } x_0 \le x \le x_{N+1} \\ 0 & \text{else} \end{cases}\,. \tag{B.55}$$

The derivative matrices are very simple:

$$D_{jk}^{(1)} = \langle\varphi_j\,|\,\frac{d}{dx}\,|\,\varphi_k\rangle = \mathrm{mod}(j-k,2)\,\frac{4}{L}\,\frac{jk}{j^2-k^2}\,, \qquad j \neq k\,, \tag{B.56}$$

$$D_{jk}^{(2)} = \langle\varphi_j\,|\,\frac{d^2}{dx^2}\,|\,\varphi_k\rangle = -\delta_{jk}\,\left(j\pi/L\right)^2\,, \tag{B.57}$$

where mod$(j-k,2)$ is zero if $j-k$ is even, and one otherwise. $D^{(1)}_{jk}$ vanishes for $j=k$.

The matrix representation of the position operator $\hat{x}$, however, is not tridiagonal. To arrive at a tridiagonal form the transformed variable

$$z = \cos\left(\pi(x-x_0)/L\right) \tag{B.58}$$

is introduced. The position operator matrix then reads

$$Q_{jk} = \langle \varphi_j \,|\, \hat{z} \,|\, \varphi_k \rangle = \frac{1}{2}\left(\delta_{j,k+1} + \delta_{j,k-1}\right) \,. \tag{B.59}$$

This matrix is particularly simple and — in fact — can be diagonalised analytically! The eigenvectors and eigenvalues of $\boldsymbol{Q}$ are

$$U_{j\alpha} = \sqrt{\frac{2}{N+1}}\,\sin\left(\frac{j\alpha\pi}{N+1}\right) \tag{B.60}$$

and

$$z_\alpha = \cos\left(\frac{\alpha\pi}{N+1}\right) \,. \tag{B.61}$$

This leads to the DVR grid points

$$x_\alpha = x_0 + \frac{L}{\pi}\,\arccos(z_\alpha) = x_0 + \alpha\,\frac{L}{N+1} = x_0 + \alpha\,\Delta x \,. \tag{B.62}$$

The grid is thus equidistantly spaced with the spacing $\Delta x = L/(N+1)$. It now becomes clear why the box boundaries have been called x_0 and x_{N+1}. Note that these points do not belong to the grid; the wavefunction vanishes there by construction.

An evenly spaced grid should lead to constant weights, and indeed one finds

$$w_\alpha^{1/2} = U_{j\alpha}/\varphi_j(x_\alpha) = \sqrt{\Delta x} \,. \tag{B.63}$$

The transformation of the first derivative matrix to DVR form is done numerically,

$$D^{(1),\mathrm{DVR}}_{\alpha\beta} = \sum_{j,k=1}^{N} U^*_{j\alpha} D^{(1)}_{jk}\, U_{k\beta} \,, \tag{B.64}$$

but the transformation of the second derivative matrix can be done analytically:

$$D^{(2),\mathrm{DVR}}_{\alpha\beta} = -\left(\tfrac{\pi}{\Delta x}\right)^2 \begin{cases} \frac{1}{3} + \frac{1}{6\,(N+1)^2} - \frac{1}{2\,(N+1)^2 \sin^2\left(\frac{\alpha\pi}{N+1}\right)}\,, & \alpha = \beta \\ \frac{2\,(-1)^{\alpha-\beta}}{(N+1)^2} \frac{\sin\left(\frac{\alpha\pi}{N+1}\right)\sin\left(\frac{\beta\pi}{N+1}\right)}{\left(\cos\left(\frac{\alpha\pi}{N+1}\right) - \cos\left(\frac{\beta\pi}{N+1}\right)\right)^2}\,, & \alpha \neq \beta \end{cases} . \tag{B.65}$$

Some final remarks are appropriate. The basis functions (B.55) may be written as $(2/L)^{1/2} \sin(j\ \arccos(z))$. This shows that they are related to the Chebyshev polynomials of the second kind [173]. The sine DVR is therefore also known as Chebyshev DVR. The sine DVR has recently been discussed by Colbert and Miller [174] who generalised it (by introducing an additional approximation) to arrive at a "universal" DVR.

B.4.5 Exponential DVR

The *exponential DVR* is equivalent to FFT. It is our experience that the exponential DVR performs faster than FFT for small grids ($N \lesssim 16$), but FFT is considerably faster for large grids ($N \gtrsim 100$). Since the exponential DVR is, on the one hand, rather well-documented in the literature [174–176] and, on the other hand, similar to the sine DVR, we will discuss it here only briefly.

When deriving the exponential DVR it is convenient to concentrate on an odd number of basis functions. We hence set $N = 2n+1$ and let the index j run between $-n$ and n rather than 1 and N. The basis functions are written as

$$\varphi_j(x) = L^{-1/2} \exp\left(2i\pi j(x - x_0)/L\right)\,, \qquad -n \le j \le n\,. \tag{B.66}$$

They are obviously periodic,

$$\varphi_j(x) = \varphi_j(x + L)\,, \tag{B.67}$$

but we consider φ_j as being defined only on the interval $[x_0, x_N]$ with $L = x_N - x_0$. The wavefunctions to be represented satisfy periodic boundary conditions, $\psi(x_0) = \psi(x_N)$.

As in the sine DVR one has to use the transformed variable $z = \cos(\pi(x - x_0)/L)$ in order to arrive at a tridiagonal representation of the (transformed) position operator. This matrix is again given by Eq. (B.59). All subsequent manipulations can be done analytically, yielding

$$\Delta x = L/N\,, \tag{B.68}$$
$$x_\alpha = x_0 + \alpha\Delta x\,, \tag{B.69}$$
$$w_\alpha = \Delta x\,. \tag{B.70}$$

The derivative matrices read

$$D^{(1),\mathrm{DVR}}_{\alpha\beta} = \begin{cases} 0\,, & \text{if } \alpha = \beta \\ \dfrac{\pi}{L}\,(-1)^{\alpha-\beta}\,\dfrac{1}{\sin\left(\pi(\alpha-\beta)/N\right)}\,, & \text{if } \alpha \neq \beta \end{cases}\,, \tag{B.71}$$

$$D^{(2),\mathrm{DVR}}_{\alpha\beta} = \begin{cases} -\dfrac{\pi^2}{3L^2}\left(N^2-1\right)\,, & \text{if } \alpha = \beta \\ -\dfrac{2\pi^2}{L^2}\,(-1)^{\alpha-\beta}\,\dfrac{\cos\left(\pi(\alpha-\beta)/N\right)}{\sin^2\left(\pi(\alpha-\beta)/N\right)}\,, & \text{if } \alpha \neq \beta \end{cases}\,. \tag{B.72}$$

B.4.6 Spherical harmonics FBR

The *spherical harmonics FBR* is the appropriate choice when there is rotational motion which must be described by two angles, θ and ϕ. The spherical harmonics $Y_{jm}(\theta,\phi)$ serve as basis functions. The matrix elements of the angular momentum operators $\hat{j}^2$, $\hat{j}_+$, $\hat{j}_-$, and $\hat{j}_z$ are then given by simple formulas. These are well-discussed in textbooks [177,178] and need not to be reported here. The potential matrix elements

$$V_{jmj'm'} = \langle Y_{jm}\,|\,V(\theta,\phi)\,|\,Y_{j'm'}\rangle \tag{B.73}$$

can be evaluated by Gauss quadrature. The θ-nodes and -weights are taken to be those of the Legendre DVR for $m = 0$, and the ϕ-nodes and -weights are taken to be those of the exponential DVR. In the actual calculations we usually take more nodes than there are basis functions, which makes the representation more VBR like.

B.4.7 Fast Fourier transform (FFT)

The *Fast Fourier transform* (FFT) method may be considered as an exponential DVR where, however, the derivative matrices are not built but the action of them on the wavefunction is evaluated by two FFTs. The FFT method is well-documented in the literature [7,82,179], and there is no need to discuss it here any further. We only remark that we use a Temperton FFT [180–182] which allows us to use grids the length of which can be factorised into powers of 2, 3, and 5, i.e.

$$N = 2^j 3^k 5^l\,, \tag{B.74}$$

where j, k, l are non-negative integers. This gives us sufficient flexibility when choosing the grid length.

C The Lanczos and the Lanczos-Arnoldi integrator

In this appendix we briefly review the short iterative Lanczos (SIL) integration scheme [63], and discuss two different error estimates for the SIL method. A reliable error estimate and step size control for the SIL integrator is important for the efficiency of the CMF scheme detailed in Sec. 5.2. We consider here the complex Lanczos, or Lanczos-Arnoldi, algorithm [103–105], since it includes the Hermitian Lanczos as a special case.

In the Lanczos scheme the exact Hamiltonian H is approximated by the reduced Hamiltonian $H_L = P_L H P_L$, where P_L denotes the projector on the Krylov space spanned by the set of vectors $H^k\psi(t)$, $k = 0, \ldots, L$. The Lanczos-Arnoldi recursion,

$$
\begin{aligned}
& & \chi_{j+1}^{(0)} &= H\psi_j & & \qquad (\text{C.1}) \\
\text{for}\quad i = 0,\ldots,j: & & \chi_{j+1}^{(i+1)} &= \chi_{j+1}^{(i)} - \beta_{ij}\psi_i \quad \text{with} \quad \beta_{ij} = \langle \psi_i \,|\, \chi_{j+1}^{(i)} \rangle & & \\
& & \psi_{j+1} &= \chi_{j+1}^{(j+1)} / \beta_{j+1,j} \quad \text{with} \quad \beta_{j+1,j} = \| \, \chi_{j+1}^{(j+1)} \, \| \,, & &
\end{aligned}
$$

constructs an orthonormal basis $\psi_0, \ldots, \psi_L$, starting from a normalised state ψ_0, in which the reduced Hamiltonian H_L is a complex upper Hessenberg matrix:

$$
\langle \psi_j \,|\, H_L \,|\, \psi_k \rangle = \begin{cases} \beta_{jk} \text{ for } j \le k+1 \\ 0 \quad \text{else} \end{cases} \,, \quad j, k = 0, \ldots, L \,. \qquad (\text{C.2})
$$

(If H is Hermitian, then matrix (C.2) becomes symmetric, i.e. tridiagonal.) The Lanczos-Arnoldi algorithm requires $L+1$ evaluations of $H \,|\, \psi\rangle$.

The SIL integrator approximates the propagated wavefunction $\psi(t+\tau)$ by

$$
|\, \psi(t+\tau) \rangle = e^{-iH_L\tau} \; |\, \psi(t) \rangle = \sum_{k=0}^{L} a_k^{(L)} \; |\, \psi_k \rangle \qquad (\text{C.3})
$$

with

$$
a_k^{(L)} = \sum_{j=0}^{L} T_{kj} \, e^{-i\lambda_j\tau} \left(T^{-1} \right)_{j0} \qquad (\text{C.4})
$$

and $\psi_0 = \psi(t) / \| \, \psi(t) \, \|$. The λ_j specify the eigenvalues and $\boldsymbol{T}$ the eigenvector matrix of the small, and hence easy to diagonalise, upper Hessenberg matrix (C.2).

The Lanczos recurrence in its standard form is in so far inefficient as the vector ψ_{L+1} as well as the matrix element $\beta_{L+1,L}$ are determined but never used. A slight modification of the SIL algorithm can circumvent this. As has been suggested by Manthe *et al.* [183] one may increase the SIL order to $L' = L + 1$ by adding a further, approximate, column to the Lanczos matrix. To this end we set $\beta_{L'L'} = \beta_{LL}$, $\beta_{L,L'} = \beta_{L',L}$, and $\beta_{j,L'} = 0$ for $j < L$. The upper Hessenberg matrix is then an $L' \times L'$ matrix, and the summation in Eqs. (C.3) and (C.4) extends to L' rather than L. The wavefunction propagated with this modified algorithm is correct up to an order $\tau^{L'}$, while it is only accurate up to an order τ^{L} in the conventional Lanczos scheme.

For the conventional SIL integrator there exists a very convenient estimate for the difference $\Delta\psi$ of the propagated and the exact wavefunction [63], namely

$$\|\,\Delta\psi\,\| \approx \frac{\beta_{10}\cdots\beta_{L+1,L}}{(L+1)!}\,\tau^{L+1}\,, \tag{C.5}$$

which may be used to adjust either the step size τ or the order L. For the modified SIL integrator one could use the same formula but replace L by L'. However, $\beta_{L'+1,L'}$ is unknown, and instead of estimating it we prefer to use Eq. (C.5) as it is. Since for any one-step method, such as Lanczos, the order of the global discretisation error is a power one lower than that of the local error [101], the error estimate therefore controls the global rather than the local error.

Turning again to the conventional Lanczos integrator we note that the error estimate (C.5) is correct to an order of $L + 1$, yet the true error also contains contributions from higher orders of τ. These contributions depend not only on the sub-diagonal but on all elements of matrix (C.2). Despite these higher contributions, the error formula (C.5) is remarkably accurate for small step sizes. However, it may grossly overestimate the error when the integrator is running at high order and thus taking large step sizes [54].

A more reliable error estimate for the (modified) Lanczos integrator is given by [54]

$$\|\,\Delta\psi\,\| = \|\,\boldsymbol{a}^{(L')} - \boldsymbol{a}^{(L'-1)}\,\|\,, \tag{C.6}$$

where a zero is appended to the shorter of the two vectors, $\boldsymbol{a}^{(L'-1)}$. This criterion thus takes as an error estimate the norm of the difference between the wavefunctions propagated by the SIL method of order L' and $L' - 1$. The accuracy of the propagation can be controlled by increasing the SIL order L' until the predicted error (C.6) becomes smaller than the prescribed error tolerance.

The improved error estimate is predominantly determined by the error of the solution obtained with an order of $L' - 1$. Hence the propagated wavefunction is one order in τ more accurate than the error estimate indicates. This is very much in the spirit of what has been discussed above, namely using Eq. (C.5) for the modified Lanczos integrator as well. Equation (C.6) seems to be rather costly because it requires the diagonalisation of matrix (C.2) after each SIL iteration. However, for large systems the evaluation of $H \mid \psi\rangle$ needs so much numerical effort that the effort for the error estimation remains negligible. For large step sizes the improved error measure (C.6) estimates the SIL integration error more accurately than the standard estimate (C.5), while for small step sizes both estimates are equally accurate [54].

D $\mathcal{L}^2$-error of the product representation

In the following the $\mathcal{L}^2$-error of the potential representation (see Eq. (95))

$$V_I^{\mathrm{app}} = \sum_J^m C_J \, v_{IJ} \tag{D.1}$$

is determined, and an estimation of the error is given. Here $I = (i_1, \ldots, i_f)$ is a multi-index. The upper summation index m denotes the set of potential expansion orders $\{m_\kappa\}$, $v_{IJ} = \prod_{\kappa=1}^f v_{i_\kappa j_\kappa}$ denotes a configuration of natural potentials, and the multi-index I represents all product grid points. If for each degree of freedom the potential expansion orders, $\{m_\kappa\}$, and the number of product grid points, $\{N_\kappa\}$, are equal, then the potential representation is exact:

$$V_I = \sum_J^N C_J \, v_{IJ} \, . \tag{D.2}$$

Having introduced this nomenclature, the $\mathcal{L}^2$-error (see Eq. (99)) can be determined:

$$\begin{aligned}
\Delta^2 \equiv & \sum_{i_1=1}^{N_1} \cdots \sum_{i_f=1}^{N_f} \left(V_{i_1 \ldots i_f} - V_{i_1 \ldots i_f}^{\mathrm{app}} \right)^2 \\
= & \sum_I^N \Bigg[\underbrace{\left(\sum_L^N C_L v_{IL} \sum_M^N C_M v_{IM} \right)}_{V_I^2} + \underbrace{\left(\sum_L^m C_L v_{IL} \sum_M^m C_M v_{IM} \right)}_{(V_I^{\mathrm{app}})^2} \\
& - \left(\sum_L^N C_L v_{IL} \sum_M^m C_M v_{IM} \right) - \left(\sum_L^m C_L v_{IL} \sum_M^N C_M v_{IM} \right) \Bigg] \\
= & \sum_I^N \left[V_I^2 + (V_I^{\mathrm{app}})^2 \right] - 2 \underbrace{\sum_L^N \sum_M^m C_L C_M \underbrace{\sum_I^N v_{IL} v_{IM}}_{\delta_{LM}}}_{\sum_I (V_I^{\mathrm{app}})^2} \\
= & \sum_{i_1=1}^{N_1} \cdots \sum_{i_f=1}^{N_f} \left[\left(V_{i_1 \ldots i_f} \right)^2 - \left(V_{i_1 \ldots i_f}^{\mathrm{app}} \right)^2 \right] \\
= & \sum_{i_1=1}^{N_1} \cdots \sum_{i_f=1}^{N_f} \left| C_{i_1 \ldots i_f} \right|^2 - \sum_{j_1=1}^{m_1} \cdots \sum_{j_f=1}^{m_f} \left| C_{j_1 \ldots j_f} \right|^2 \qquad \text{(D.3)} \\
= & \sum_{j_1=m_1+1}^{N_1} \sum_{j_2=1}^{N_2} \cdots \sum_{j_f=1}^{N_f} \left| C_{j_1 \ldots j_f} \right|^2 + \sum_{j_1=1}^{m_1} \sum_{j_2=m_2+1}^{N_2} \sum_{j_3=1}^{N_3} \cdots \sum_{j_f=1}^{N_f} \left| C_{j_1 \ldots j_f} \right|^2 +
\end{aligned}$$

$$\ldots + \sum_{j_1=1}^{m_1} \ldots \sum_{j_{f-1}=1}^{m_{f-1}} \sum_{j_f=m_f+1}^{N_f} \left| C_{j_1 \ldots j_f} \right|^2 . \tag{D.4}$$

The last transformation can be proven by induction. Introducing the notation

$$a_\kappa = \sum_{i_\kappa=1}^{m_\kappa} \text{ and } b_\kappa = \sum_{i_\kappa=m_\kappa+1}^{N_\kappa} , \quad \text{i.e. } a_\kappa + b_\kappa = \sum_{i_\kappa=1}^{N_\kappa} , \tag{D.5}$$

the summation over all indices may be alternatively written as

$$\sum_{i_1=1}^{N_1} \ldots \sum_{i_f=1}^{N_f} = \prod_{\kappa=1}^{f} (a_\kappa + b_\kappa) . \tag{D.6}$$

Adding the second term of Eq. (D.3) to the equations (D.3) and (D.4), the induction hypothesis in the new nomenclature reads

$$\prod_{\kappa=1}^{f} (a_\kappa + b_\kappa) = \tag{D.7}$$

$$\left.\begin{array}{cccccccc}
 & b_1 & (a_2+b_2) & (a_3+b_3) & \cdots & (a_{f-1}+b_{f-1}) & (a_f+b_f) \\
+ & a_1 & b_2 & (a_3+b_3) & \cdots & (a_{f-1}+b_{f-1}) & (a_f+b_f) \\
+ & a_1 & a_2 & b_3 & \cdots & (a_{f-1}+b_{f-1}) & (a_f+b_f) \\
\vdots & & & & & & \\
+ & a_1 & a_2 & a_3 & \cdots & a_{f-1} & b_f \\
+ & a_1 & a_2 & a_3 & \cdots & a_{f-1} & a_f
\end{array}\right\} \begin{array}{c} f+1 \\ \text{summation} \\ \text{terms} . \end{array}$$

For $f = 1$ the induction hypothesis is obviously satisfied

$$\prod_{\kappa=1}^{1} (a_\kappa + b_\kappa) = b_1 + a_1 .$$

Performing one induction step one obtains the induction hypothesis for $f+1$

$$\prod_{\kappa=1}^{f+1} (a_\kappa + b_\kappa) = \left[\prod_{\kappa=1}^{f} (a_\kappa + b_\kappa) \right] (a_{f+1} + b_{f+1}) \tag{D.8}$$

$$
= \left.\begin{array}{llllll}
\, b_1 & (a_2+b_2) & (a_3+b_3) & \cdots & (a_f+b_f) & (a_{f+1}+b_{f+1}) \\
+\, a_1 & b_2 & (a_3+b_3) & \cdots & (a_f+b_f) & (a_{f+1}+b_{f+1}) \\
+\, a_1 & a_2 & b_3 & \cdots & (a_f+b_f) & (a_{f+1}+b_{f+1}) \\
\vdots & & & & & \\
+\, a_1 & a_2 & a_3 & \cdots & a_f & b_{f+1} \\
+\, a_1 & a_2 & a_3 & \cdots & a_f & a_{f+1}
\end{array}\right\}
\begin{array}{c} f+2 \\ \text{summation} \\ \text{terms}\,, \end{array}
$$

proving the validity of the induction hypothesis.

Having determined the $\mathcal{L}^2$-error of the product expansion (D.4) as a function of the expansion coefficients $C_{j_1 \ldots j_f}$, an error estimation as a function of the natural populations $\lambda^{(\kappa)}_{j_\kappa}$ is derived as follows.

The potential density matrices $\boldsymbol{\varrho}^{(\kappa)}$, defined according to Eq. (94), are diagonal in the basis of their eigenvectors, the natural potentials $\boldsymbol{v}^{(\kappa)}_{j_\kappa}$, and can be expressed in terms of the potential expansion coefficients $C_{j_1 \ldots j_f}$ as follows:

$$
\varrho^{\mathrm{diag},(\kappa)}_{\alpha\beta} = \sum_{j_1=1}^{N_1} \cdots \sum_{j_{\kappa-1}=1}^{N_{\kappa-1}} \sum_{j_{\kappa+1}=1}^{N_{\kappa+1}} \cdots \sum_{j_f=1}^{N_f} C_{j_1 \ldots \alpha \ldots j_f} C_{j_1 \ldots \beta \ldots j_f} = \delta_{\alpha\beta} \lambda^{(\kappa)}_{\alpha} \,. \tag{D.9}
$$

Thus, the natural populations $\lambda^{(\kappa)}_{j_\kappa}$ define an upper limit for the square of the modulus of the potential expansion coefficients,

$$
|\, C_{j_1 \ldots j_f} \,|^2 \leq \min \left\{ \lambda^{(1)}_{j_1}, \ldots, \lambda^{(f)}_{j_f} \right\} \,. \tag{D.10}
$$

Comparing this inequality with the $\mathcal{L}^2$-error of the product expansion (D.4) shows that the potential expansion can be safely truncated if the corresponding natural populations are sufficiently small.

E Overview of software packages

In this appendix the MCTDH program package will be briefly described. The programs are written mainly in standard FORTRAN 77. Particular care has been taken to make the program user friendly, both with respect to usage and development. The structure is modular, with information being passed between the modules using read-write files and common blocks contained in include files. Documentation is in HTML format.

The package has been implemented on a number of different platforms, and App. E.6 gives some information on the installation of the code. This set of programs will be made available on request to the authors.

E.1 The MCTDH program

The MCTDH program creates an initial wavepacket and propagates it in time, i.e. it solves the MCTDH equations of motion (see Sec. 3.1). The program contains four sequential sections which reflect the stages of the calculation: primitive basis (DVR) generation; representation of the operator in the primitive basis; generation of the initial wavefunction; propagation of the wavefunction.

Desired options and input parameters can be comfortably specified in an input file with the aid of keywords and arguments. If a parameter is not specified a reasonable default is taken. Conversion factors are built in, so that data can be input in a variety of units.

For the primitive basis functions, the FFT and DVR schemes of App. B are available.

The Hamiltonian is specified in a text file which is translated by the program. The program is capable of parsing a variety of mathematical expressions, which often allows the Hamiltonian to be implemented in terms of an analytic formula, avoiding the need to write a routine for that purpose. More complicated functions can be added to the library of functions. If a potential does not have an analytic product form (64), one can use the natural potential fit (Sec. 6.1), determined by the POTFIT program (see below). Alternatively, the multidimensional potential can be used with the CDVR method (Sec. 4.3). Complex absorbing potentials (Sec. 4.7) may also be included in the Hamiltonian.

The initial wavepacket can be set up by employing the methods described in Sec. 7. Multi-mode single-particle functions, recommended for large systems or for strongly coupled degrees of freedom (Sec. 4.5), can be simply defined. Non-adiabatic systems can be treated within both the single- and the multi-set formulation (Sec. 3.5).

The wavepacket may be propagated using the VMF or the CMF integration scheme (Sec. 5). In addition to the standard single-particle functions, the program allows the use of natural (Sec. 3.3) and interaction picture (Sec. 3.4) orbitals. The program can also be used to propagate wavepackets employing the standard or the TDH method (Sec. 2.2 and 2.3).

E.2 The POTFIT *program*

The POTFIT program comprises all the features presented in Sec. 6. Having given the potential energy values of an arbitrarily chosen surface on a product grid, the potential energy surface is expanded in a set of natural potentials. The input parameters (e.g. the set of expansion orders $\{m_\kappa\}$, the contraction mode, the energy cut-off, the number of iteration steps) are specified in the same manner as the MCTDH input parameters, i.e. using keywords in an input file. The product grid points can be generated employing the same FFT and DVR schemes used for the representation of the single-particle functions of the subsequent MCTDH calculation. The potential data generated can then be used directly by the MCTDH program.

E.3 The ANALYSE *programs*

The ANALYSE suite of programs serves to extract observable quantities from the data produced during the propagation, e.g. the wavefunction or auto-correlation function. In principle there is a library of routines to read and extract data from the files produced by the MCTDH program. The various ANALYSE programs then manipulate this data to extract the quantity of interest. The library of routines thus provides an interface to the MCTDH program, easing the development of new ANALYSE programs.

The programs enable one, for example, to determine and display photo-absorption and photo-dissociation spectra (see Sec. 8.3), reaction probabilities (Sec. 8.6), state populations (Sec. 8.5), and adiabatically corrected energy distributions (Sec. 7.2).

Programs also exist to check the accuracy of a calculation. The convergence of a calculation with respect to the number of single-particle functions can be examined by computing the natural populations (Sec. 3.3), estimating the error of the auto-correlation function (Sec. 8.7), or comparing two wavefunctions with different numbers of single-particle functions (Sec. 8.2). One may also detect numerical inaccuracies by checking the orthonormality of the single-particle functions, or the conservation of the norm of the wavefunction. Finally, the step-sizes of the VMF and CMF integration scheme (Sec. 5) can be analysed.

Standard plot programs, such as GnuPlot or Xmgr, can then be used to visualise these results. The Mathematica program, driven by script files, can also be used to automatically produce graphical output from the programs. This is particularly useful for animation graphics, such as the evolution of the density along a coordinate with time.

E.4 The Filter *program*

With the aid of the Filter program one may determine ro-vibrational spectra of molecules or clusters using the filter-diagonalisation method (see Sec. 8.4). A Mathematica routine for plotting the obtained line spectrum also exists. Different damping functions, variational principles, and error estimates are available (see Ref. [126] for details). As in the MCTDH program, the input is based on keywords.

E.5 The MCTDH library

In the above-mentioned programs a variety of standard mathematical problems have to be solved. We have stored the corresponding routines in a library which can also be used independently of the MCTDH package. The library contains efficient routines for many operations involving vectors, matrices and tensors (multiplication, inversion, etc.), solvers for several kinds of linear equations and eigenvalue problems, fast Fourier transformation, spline interpolation, and string manipulation. Furthermore, the library includes a number of integrators for ordinary differential equations, such as an Adams-Bashforth-Moulton predictor-corrector, a Bulirsch-Stoer extrapolation scheme, a short iterative Lanczos and Lanczos-Arnoldi method, and a second-order differencing integrator.

E.6 System requirements

Our MCTDH software package has been installed on a variety of platforms, ranging from personal computers through various workstations to large vector machines. Tab. E.1 offers an overview of the platforms on which our code has run so far. The compilation of the program is very easy: a shell-script recognises the architecture being used and automatically chooses the appropriate compiler options and settings. The system requirements are quite small. For the automatic compilation a C-shell is needed, as well as a Posix-make. A few routines are written in C and require an Ansi-C compiler. An Html browser (e.g. Netscape) is needed for reading the program documentation. In order to visualise the results computed with the Analyse programs (see App. E.3),

Table E.1
The platforms on which our MCTDH software package has been installed so far. The first two columns specify the machine type. In the third column the operating system is given. The fourth column denotes the compiler that has been used.

Machine	Architecture	Operating system	Compiler
CRAY	J90	Unicos	f90
	T90		
DEC	alpha	Ultrix	f77
HP	9000/755	HP UX	fort77
IBM	powerPC	AIX	xlf
	power		
	power2		
PC	pentium	Linux	g77
SGI	mips2	Irix	f77
Sun	sparc20	SunOS	f77

MATHEMATICA is recommended. Note that no commercial libraries, such as IMSL, ESSL or NAG, are necessary. On all machines listed in Tab. E.1, with the exception of CRAY, shared libraries are supported.

References

[1] *Time-dependent methods for quantum dynamics*, edited by K. C. Kulander (Elsevier, Amsterdam, 1991).

[2] R. Schinke, *Photodissociation Dynamics* (Cambridge University Press, Cambridge, 1993).

[3] *Dynamics of Molecules and Chemical Reactions*, edited by R. E. Wyatt and J. Z. H. Zhang (Marcel Dekker, New York, 1996).

[4] M. Manz and L. Wöste, *Femtosecond Chemistry* (Wiley-VCH, Weinheim, 1994).

[5] *Femtochemistry*, edited by M. Chergui (World Scientific, Singapore, 1996).

[6] R. B. Gerber, R. Kosloff, and M. Berman, Computer Phys. Rep. **5**, 59 (1986).

[7] R. Kosloff, J. Phys. Chem. **92**, 2087 (1988).

[8] *Numerical Grid Methods and their Application to Schrödinger's Equation*, edited by C. Cerjan (Kluwer Academic Publishers, Dordrecht, 1993).

[9] C. Leforestier, R. H. Bisseling, C. Cerjan, M. D. Feit, R. Friesner, A. Guldenberg, A. Hammerich, G. Jolicard, W. Karrlein, H.-D. Meyer, N. Lipkin, O. Roncero, and R. Kosloff, J. Comp. Phys. **94**, 59 (1991).

[10] R. Kosloff, Ann. Rev. Phys. Chem. **45**, 145 (1994).

[11] Z. Bačić and J. C. Light, J. Chem. Phys. **85**, 4594 (1986).

[12] Z. Bačić and J. C. Light, J. Chem. Phys. **86**, 3065 (1987).

[13] S. Liu, Z. Bačić, J. W. Moskowitz, and K. E. Schmidt, J. Chem. Phys. **103**, 1829 (1995).

[14] M. Warken and V. Bonačić-Koutecký, Chem. Phys. Lett. **272**, 284 (1997).

[15] R. E. Wyatt, C. Iung, and C. Leforestier, J. Chem. Phys. **97**, 3458 (1992).

[16] M. L. Brewer, J. S. Hulme, and D. E. Manolopoulos, J. Chem. Phys. **106**, 4832 (1997).

[17] M. F. Hermann, Ann. Rev. Phys. Chem. **45**, 83 (1994).

[18] M. A. Sepulveda and F. Grossmann, Adv. Chem. Phys. **96**, 191 (1996).

[19] P. A. M. Dirac, Proc. Cambridge Philos. Soc. **26**, 376 (1930).

[20] A. D. McLachlan, Mol. Phys. **8**, 39 (1964).

[21] J. Kucar, H.-D. Meyer, and L. Cederbaum, Chem. Phys. Lett. **140**, 525 (1987).

[22] H.-D. Meyer, J. Kucar, and L. Cederbaum, J. Math. Phys. **29**, 1417 (1988).

[23] J. Kucar and H.-D. Meyer, Z. Phys. D **18**, 325 (1991).

[24] N. Makri and W. H. Miller, J. Chem. Phys. **87**, 5781 (1987).

[25] R. Kosloff, A. D. Hammerich, and M. A. Ratner, in *Large finite systems: Proceedings of the twentieth Jerusalem Symposium of Quantum Chemistry and Biochemistry*, edited by J. Jortner and B. Pullman (Reidel, Dordrecht, 1987).

[26] A. D. Hammerich, R. Kosloff, and M. A. Ratner, Chem. Phys. Lett. **171**, 97 (1990).

[27] H.-D. Meyer, U. Manthe, and L. S. Cederbaum, Chem. Phys. Lett. **165**, 73 (1990).

[28] U. Manthe, H.-D. Meyer, and L. S. Cederbaum, J. Chem. Phys. **97**, 3199 (1992).

[29] H.-D. Meyer, U. Manthe, and L. S. Cederbaum, in *Numerical Grid Methods and their Application to Schrödinger's Equation*, edited by C. Cerjan (Kluwer Academic Publishers, Dordrecht, 1993), pp. 141–152.

[30] H.-D. Meyer, in *The Encyclopedia of Computational Chemistry*, edited by P. v. R. Schleyer, N. L. Allinger, T. Clark, J. Gasteiger, P. A. Kollman, H. F. Schaefer III, and P. R. Schreiner (John Wiley and Sons, Chichester, 1998), pp. 3011–3018.

[31] U. Manthe, H.-D. Meyer, and L. S. Cederbaum, J. Chem. Phys. **97**, 9062 (1992).

[32] U. Manthe and A. D. Hammerich, Chem. Phys. Lett. **211**, 7 (1993).

[33] A. D. Hammerich, U. Manthe, R. Kosloff, H.-D. Meyer, and L. S. Cederbaum, J. Chem. Phys. **101**, 5623 (1994).

[34] L. Liu, J.-Y. Fang, and H. Guo, J. Chem. Phys. **102**, 2404 (1995).

[35] G. Worth, H.-D. Meyer, and L. S. Cederbaum, J. Chem. Phys. **105**, 4412 (1996).

[36] G. Worth, H.-D. Meyer, and L. S. Cederbaum, J. Chem. Phys. **109**, 3518 (1998).

[37] A. Raab, G. Worth, H.-D. Meyer, and L. S. Cederbaum, J. Chem. Phys. **110**, 936 (1999).

[38] G. Worth, H.-D. Meyer, and L. S. Cederbaum, Chem. Phys. Lett. **299**, 451 (1999).

[39] J.-Y. Fang and H. Guo, J. Chem. Phys. **102**, 1944 (1995).

[40] A. Jäckle and H.-D. Meyer, J. Chem. Phys. **102**, 5605 (1995).

[41] U. Manthe and F. Matzkies, Chem. Phys. Lett. **252**, 71 (1996).

[42] F. Matzkies and U. Manthe, J. Chem. Phys. **106**, 2646 (1997).

[43] F. Matzkies and U. Manthe, J. Chem. Phys. **108**, 4828 (1998).

[44] F. Matzkies and U. Manthe, J. Chem. Phys. **110**, 88 (1999).

[45] A. Jäckle and H.-D. Meyer, J. Chem. Phys. **109**, 2614 (1998).

[46] A. Jäckle, M.-C. Heitz, and H.-D. Meyer, J. Chem. Phys. **110**, 241 (1999).

[47] A. P. J. Jansen, J. Chem. Phys. **99**, 4055 (1993).

[48] J.-Y. Fang and H. Guo, J. Chem. Phys. **101**, 5831 (1994).

[49] J.-Y. Fang and H. Guo, Chem. Phys. Lett. **235**, 341 (1995).

[50] A. P. J. Jansen and H. Burghgraef, Surf. Sci. **344**, 149 (1995).

[51] A. Capellini and A. P. J. Jansen, J. Chem. Phys. **104**, 3366 (1996).

[52] M. Ehara, H.-D. Meyer, and L. S. Cederbaum, J. Chem. Phys. **105**, 8865 (1996).

[53] R. Milot and A. P. J. Jansen, J. Chem. Phys. **109**, 1966 (1998).

[54] M. H. Beck and H.-D. Meyer, Z. Phys. D **42**, 113 (1997).

[55] U. Manthe, J. Chem. Phys. **105**, 6989 (1996).

[56] A. Jäckle and H.-D. Meyer, J. Chem. Phys. **104**, 7974 (1996).

[57] A. Jäckle and H.-D. Meyer, J. Chem. Phys. **109**, 3772 (1998).

[58] E. J. Heller, J. Chem. Phys. **62**, 1544 (1975).

[59] M. D. Feit, J. A. Fleck Jr., and A. Steiger, J. Comp. Phys. **47**, 412 (1982).

[60] M. D. Feit and J. A. Fleck Jr., J. Chem. Phys. **78**, 301 (1983).

[61] M. D. Feit and J. A. Fleck Jr., J. Chem. Phys. **80**, 2578 (1984).

[62] H. Tal-Ezer and R. Kosloff, J. Chem. Phys. **81**, 3967 (1984).

[63] T. J. Park and J. C. Light, J. Chem. Phys. **85**, 5870 (1986).

[64] P. McGuire and D. J. Kouri, J. Chem. Phys. **60**, 2488 (1974).

[65] R. T. Pack, J. Chem. Phys. **60**, 633 (1974).

[66] J. Frenkel, *Wave Mechanics* (Clarendon Press, Oxford, 1934).

[67] P. Jungwirth and R. B. Gerber, J. Chem. Phys. **102**, 6046 (1995).

[68] P. Jungwirth and R. B. Gerber, J. Chem. Phys. **102**, 8855 (1995).

[69] P. Jungwirth, E. Fredj, and R. B. Gerber, J. Chem. Phys. **104**, 9332 (1996).

[70] *Modern Methods for Multidimensional Dynamics Computations in Chemistry*, edited by R. B. Gerber, P. Jungwirth, E. Fredj, A. Rom, and D. L. Thompson (World Scientific, Singapore, 1998).

[71] R. D. Coalson, Chem. Phys. Lett. **165**, 443 (1990).

[72] J. Campos-Martinez and R. D. Coalson, J. Chem. Phys. **93**, 4740 (1990).

[73] J. Campos-Martinez and R. D. Coalson, J. Chem. Phys. **99**, 9629 (1993).

[74] J. R. Waldeck, J. Campos-Martinez, and R. D. Coalson, J. Chem. Phys. **94**, 2773 (1991).

[75] E. Camona-Novillo, D. Calloto, and J. Campos-Martinez, J. Chem. Phys. **104**, 8016 (1996).

[76] P. Jungwirth and B. Schmidt, Chem. Phys. Lett. **275**, 127 (1997).

[77] P. Jungwirth, E. Fredj, and R. B. Gerber, J. Chem. Phys. **107**, 8963 (1997).

[78] R. McWeeny, *Methods of Molecular Quantum Mechanics* (Academic Press, London, 1989).

[79] K. Blum, *Density matrix theory and applications* (Plenum Press, New York, 1981).

[80] U. Manthe, J. Chem. Phys. **101**, 2652 (1994).

[81] A. Jäckle, Ph.D. thesis, Universität Heidelberg, 1997.

[82] D. Kosloff and R. Kosloff, J. Comp. Phys. **52**, 35 (1983).

[83] D. O. Harris, G. G. Engerholm, and G. W. Gwinn, J. Chem. Phys. **43**, 1515 (1965).

[84] A. S. Dickinson and P. R. Certain, J. Chem. Phys. **49**, 4209 (1968).

[85] J. C. Light, I. P. Hamilton, and J. V. Lill, J. Chem. Phys. **82**, 1400 (1985).

[86] J. C. Light, in *Time-Dependent Quantum Molecular Dynamics*, edited by J. Broeckhove and L. Lathouwers (Plenum, New York, 1992), pp. 185–199.

[87] E. Sim and N. Makri, J. Chem. Phys. **102**, 5616 (1995).

[88] C. Leforestier and R. E. Wyatt, J. Chem. Phys. **78**, 2334 (1983).

[89] R. Kosloff and D. Kosloff, J. Comp. Phys. **63**, 363 (1986).

[90] G. Jolicard and E. Austin, Chem. Phys. Lett. **121**, 106 (1985).

[91] G. Jolicard, C. Leforestier, and E. Austin, J. Chem. Phys. **88**, 1026 (1988).

[92] U. V. Riss and H.-D. Meyer, J. Phys. B **26**, 4503 (1993).

[93] D. Neuhauser and M. Baer, J. Chem. Phys. **90**, 4351 (1989).

[94] D. Neuhauser and M. Baer, J. Chem. Phys. **91**, 4651 (1989).

[95] I. Last, A. Baram, H. Szichman, and M. Baer, J. Phys. Chem. **97**, 7040 (1993).

[96] T. Seideman and W. H. Miller, J. Chem. Phys. **96**, 4412 (1992).

[97] T. Seideman and W. H. Miller, J. Chem. Phys. **97**, 2499 (1992).

[98] U. V. Riss and H.-D. Meyer, J. Phys. B **28**, 1475 (1995).

[99] U. V. Riss and H.-D. Meyer, J. Chem. Phys. **105**, 1409 (1996).

[100] A. Vibok and G. G. Balint-Kurti, J. Chem. Phys. **96**, 7615 (1992).

[101] C. W. Gear, *Numerical Initial Value Problems in Ordinary Differential Equations* (Prentice-Hall, Englewood Cliffs, New Jersey, 1971).

[102] W. H. Press, S. A. Teukolsky, W. T. Vetterling, and B. P. Flannery, *Numerical Recipes* (Cambridge University Press, Cambridge, 1992).

[103] W. E. Arnoldi, Q. Appl. Math. **9**, 17 (1951).

[104] Y. Saad, Lin. Alg. Appl. **34**, 269 (1980).

[105] R. A. Friesner, L. S. Tuckerman, B. C. Dornblaser, and T. V. Russo, J. Sci. Comp. **4**, 327 (1989).

[106] M. H. Beck and H.-D. Meyer, unpublished results.

[107] M.-C. Heitz and H.-D. Meyer, unpublished results.

[108] E. Schmidt, Math. Ann. **63**, 433 (1906).

[109] A. Jäckle and H.-D. Meyer, J. Chem. Phys. **105**, 6778 (1996).

[110] R. Schinke, M. Nonella, H. U. Suter, and J. R. Huber, J. Chem. Phys. **93**, 1098 (1990).

[111] P. Siegbahn and B. Liu, J. Chem. Phys. **68**, 2457 (1978).

[112] D. G. Truhlar and C. J. Horowitz, J. Chem. Phys. **68**, 2466 (1978).

[113] D. G. Truhlar and C. J. Horowitz, J. Chem. Phys. **71**, 1514 (1979).

[114] J. Z. H. Zhang, D. J. Kouri, K. Haug, D. W. Schwenke, Y. Shima, and D. G. Truhlar, J. Chem. Phys. **88**, 2492 (1988).

[115] R. Kosloff and H. Tal-Ezer, Chem. Phys. Lett. **127**, 223 (1986).

[116] D. J. Tannor and D. E. Weeks, J. Chem. Phys. **98**, 3884 (1993).

[117] D. E. Weeks and D. J. Tannor, Chem. Phys. Lett. **207**, 301 (1993).

[118] U. Manthe, Ph.D. thesis, Universität Heidelberg, 1991.

[119] V. Engel, Chem. Phys. Lett. **189**, 76 (1992).

[120] D. Neuhauser, J. Chem. Phys. **93**, 2611 (1990).

[121] M. R. Wall and D. Neuhauser, J. Chem. Phys. **102**, 8011 (1995).

[122] V. A. Mandelshtam and H. S. Taylor, J. Chem. Phys. **107**, 6756 (1997).

[123] T. P. Grozdanov, V. A. Mandelshtam, and H. S. Taylor, J. Chem. Phys. **103**, 7990 (1995).

[124] V. A. Mandelshtam, T. P. Grozdanov, and H. S. Taylor, J. Chem. Phys. **103**, 10074 (1995).

[125] G.-J. Kroes, M. R. Wall, J. W. Pang, and D. Neuhauser, J. Chem. Phys. **106**, 1800 (1997).

[126] M. H. Beck and H.-D. Meyer, J. Chem. Phys. **109**, 3730 (1998).

[127] E. Narevicius, D. Neuhauser, H. J. Korsch, and N. Moiseyev, Chem. Phys. Lett. **276**, 250 (1997).

[128] V. A. Mandelshtam, J. Chem. Phys. **108**, 9999 (1998).

[129] K. C. Kulander and E. J. Heller, J. Chem. Phys. **69**, 2439 (1978).

[130] R. C. Mowrey and D. J. Kouri, J. Chem. Phys. **84**, 6466 (1986).

[131] Y. Sun, R. C. Mowrey, and D. J. Kouri, J. Chem. Phys. **87**, 339 (1987).

[132] D. Neuhauser, J. Chem. Phys. **93**, 7836 (1990).

[133] G. G. Balint-Kurti, R. N. Dixon, and C. C. Marston, J. Chem. Soc., Faraday Trans. **86**, 1741 (1990).

[134] G. G. Balint-Kurti, R. N. Dixon, C. C. Marston, and A. J. Mulholland, Computer Phys. Comm. **63**, 126 (1991).

[135] D. E. Weeks and D. J. Tannor, Chem. Phys. Lett. **224**, 451 (1994).

[136] W. H. Miller, S. D. Schwartz, and J. W. Tromp, J. Chem. Phys. **79**, 4889 (1983).

[137] W. H. Thompson and W. H. Miller, Chem. Phys. Lett. **206**, 123 (1993).

[138] D. Neuhauser and M. Baer, J. Phys. Chem. **94**, 185 (1990).

[139] D. Neuhauser, M. Baer, R. S. Judson, and D. J. Kouri, J. Chem. Phys. **93**, 312 (1990).

[140] D. E. Manolopoulos and M. H. Alexander, J. Chem. Phys. **97**, 2527 (1992).

[141] D. H. Zhang, Q. Wu, and J. Z. H. Zhang, J. Chem. Phys. **102**, 124 (1995).

[142] N. Balakrishnan and N. Sathyamurthy, Chem. Phys. Lett. **240**, 119 (1995).

[143] T. Peng, D. H. Zhang, J. Z. H. Zhang, and R. Schinke, Chem. Phys. Lett. **248**, 37 (1996).

[144] D. Neuhauser, M. Baer, R. S. Judson, and D. J. Kouri, Computer Phys. Comm. **63**, 460 (1991).

[145] J.-Y. Fang and H. Guo, J. Mol. Struct. (Theochem) **341**, 201 (1995).

[146] T. Gerdts and U. Manthe, J. Chem. Phys. **107**, 6584 (1997).

[147] J. K. McDonald, J. A. Merrit, V. F. Kalasinksky, H. L. Heusel, and J. R. During, J. Mol. Spec. **117**, 69 (1986).

[148] H. Buchenau, J. P. Toennies, J. Arnold, and J. Wolfrum, Ber. Bunsenges. Phys. Chem. **94**, 1231 (1990).

[149] G. C. Schatz, J. Phys. Chem. **100**, 12839 (1996).

[150] S. M. Auerbach and W. H. Miller, J. Chem. Phys. **100**, 1103 (1994).

[151] S. L. Mielke, G. C. Lynch, D. G. Truhlar, and D. W. Schwenke, J. Phys. Chem. **98**, 8000 (1994).

[152] F. J. Aoiz, L. Bañares, T. Díez-Rojo, V. J. Herrero, and V. Sáez Rábanos, J. Phys. Chem. **100**, 4071 (1996).

[153] G. W. Johnston, B. Katz, K. Tsukiyama, and R. Bersohn, J. Phys. Chem. **91**, 5445 (1987).

[154] H. B. Levene, D. L. Phillips, J.-C. Nieh, D. P. Gerrity, and J. J. Valentini, Chem. Phys. Lett. **143**, 317 (1988).

[155] R. A. Brownsword, M. Hillenkamp, T. Laurent, H.-R. Volpp, J. Wolfrum, R. K. Vatsa, and H.-S. Yoo, J. Phys. Chem. A **101**, 6448 (1998).

[156] A. Baram, I. Last, and M. Baer, Chem. Phys. Lett. **212**, 649 (1993).

[157] D. M. Charutz, I. Last, and M. Baer, J. Chem. Phys. **106**, 7654 (1997).

[158] R. B. Gerber, L. H. Beard, and D. J. Kouri, J. Chem. Phys. **74**, 4709 (1981).

[159] H. F. Bowen, D. J. Kouri, R. C. Mowrey, A. T. Yinnon, and R. B. Gerber, J. Chem. Phys. **99**, 704 (1993).

[160] D. Lemoine, J. Chem. Phys. **101**, 10526 (1994).

[161] I. Yamazaki, T. Murao, T. Yamanaka, and K. Yoshihara, Faraday Discuss. Chem. Soc. **75**, 395 (1983).

[162] K. K. Innes, I. G. Ross, and W. R. Moonaw, J. Mol. Spec. **132**, 492 (1988).

[163] H. Köppel, W. Domcke, and L. S. Cederbaum, Adv. Chem. Phys. **57**, 59 (1984).

[164] L. Seidner, G. Stock, A. L. Sobolewski, and W. Domcke, J. Chem. Phys. **96**, 5298 (1992).

[165] C. Woywood, W. Domcke, A. L. Sobolewski, and H.-J. Werner, J. Chem. Phys. **100**, 1400 (1994).

[166] S. Krempl, M. Winterstetter, H. Plöhn, and W. Domcke, J. Chem. Phys. **100**, 926 (1994).

[167] A. G. Redfield, Adv. Magn. Reson. **1**, 1 (1965).

[168] G. Lindblad, Commun. Math. Phys. **48**, 119 (1976).

[169] T. Gerdts and U. Manthe, J. Chem. Phys. **106**, 3017 (1997).

[170] P. Kramer and M. Saraceno, *Geometry of the time-dependent variational principle* (Springer, Berlin, 1981).

[171] J. V. Lill, G. A. Parker, and J. C. Light, J. Chem. Phys. **85**, 900 (1986).

[172] J. V. Lill, G. A. Parker, and J. C. Light, Chem. Phys. Lett. **89**, 493 (1982).

[173] M. Abramowitz and I. A. Stegun, *Handbook of mathematical functions.* (Dover Publications, New York, 1972).

[174] D. T. Colbert and W. H. Miller, J. Chem. Phys. **96**, 1982 (1992).

[175] R. Meyer, J. Chem. Phys. **52**, 2053 (1970).

[176] C. C. Marston and G. G. Balint-Kurti, J. Chem. Phys. **91**, 357 (1989).

[177] A. R. Edmonds, *Angular momentum in quantum mechanics.* (Princeton University Press, Princeton, New Jersey, 1957).

[178] R. N. Zare, *Angular Momentum, Understanding spatial effects in Chemistry and Physics.* (John Wiley and Sons, New York, 1988).

[179] R. Kosloff, in *Dynamics of Molecules and Chemical Reactions*, edited by R. E. Wyatt and J. Z. H. Zhang (Marcel Dekker, New York, 1996), pp. 185–230.

[180] C. J. Temperton, J. Comp. Phys. **52**, 1 (1983).

[181] C. J. Temperton, J. Comp. Phys. **52**, 198 (1983).

[182] C. J. Temperton, J. Comp. Phys. **52**, 340 (1983).

[183] U. Manthe, H. Köppel, and L. S. Cederbaum, J. Chem. Phys. **95**, 1708 (1991).